STRUCTURAL ANALYSIS AND DESIGN OF VARIABLE DISPLACEMENT LINKAGE PUMPS

A Thesis
SUBMITTED TO THE FACULTY OF
UNIVERSITY OF MINNESOTA
BY

Anirudh Reddy Ravula

IN PARTIAL FULFILLMENT OF THE REQUIREMENTS
FOR THE DEGREE OF
MASTER OF SCIENCE

James D. Van De Ven, PhD

May 2017

Acknowledgements

My deep gratitude goes first to my advisor, Dr. James D. Van De Ven for his invaluable guidance, support and belief in me. He expertly guided through my graduate education and his personal generosity helped make my time at University of Minnesota enjoyable. I would like to thank Dr. Shawn Wilhelm, my project partner and a good friend, for putting up with my never ending technical questions. His support and encouragement brought me where I am today and I am lucky to have had a chance to work with him. To my lab colleagues and friends, who provided insightful comments on improving my work, I thank you. I extend my heartfelt gratitude to Erika Langford, my close friend and confident, who helped me through stressful times. I thank you for being there for me when I needed you the most.

Dedication

I dedicate this work to my parents Madhavi.R and Pradeep.R, and my brother Achyuth.R, for all their love and support.

Abstract

Fluid power systems are ubiquitous, providing high power within a small package. They are also capable of producing extremely high forces and rapid precise response. However, the average efficiency of fluid power systems is just around 21%, while consuming 2% of the total energy in the United States. A large percentage of these energy losses is due to ineffective flow control methods. While variable displacement pumps offer a more efficient method of controlling the speed of an actuator over metering valves, most of them are inefficient at low displacements. The variable displacement linkage pump architecture, developed recently at the University of Minnesota, shows great promise to achieve high efficiency across the full displacement range. Pin joints, which have a linear relationship between energy loss and displacement, are used instead of hydrodynamic planar joints used in conventional pumps.

In this thesis, a new generation variable linkage pump prototype, with a displacement of 10cc/rev and maximum pressure of 3500 psi, is presented. The pump was designed to address the issues of previous generation linkage pump prototypes by improving the volumetric efficiency and reducing the size, thereby advancing the pump towards commercialization. A primary focus of this work was supporting design decisions using structural analysis. A specific focus was on minimizing the linkage deflection by designing the links to be in double shear. The finite element analysis results were validated by comparing the rotational deflection of the adjustment mechanism assembly obtained through simulations with that of those from experimental results.

Unlike conventional variable displacement pump architectures, linkage pumps have the potential to pump a slurry, as the pumping fluid can be separated from the lubricating fluid. However, conventional reciprocating seals like elastomeric and clearance seals wear quickly and leak when operating with abrasive fluids, whereas packed glands and mechanical seals, which are the popular choice in industrial slurry pumps, result in high leakage and high initial cost respectively. Rolling diaphragm seals offer negligible friction

and zero effective leakage, possibly offering a better option compared to other seals. However, commercial diaphragm seals are currently being used for pressures under 60bar and not much research has been done since 1970's to improve their pressure capability. In this thesis, a preliminary study is presented on analyzing the behavior of rolling diaphragms under various conditions using finite element analysis. The convolution portion of the seal was analyzed by modelling fiber and elastomer individually. Increasing the fiber diameter and number of fibers reduced the deformation of elastomer and stress induced in the fiber. Fiber diameter is found to be a more important parameter than the number of fibers. Analysis showed that a Kevlar reinforced neoprene diaphragm seal would be able to withstand 80 bar before the elastomer fails. The possibility of modifying the design to withstand higher pressures is also discussed in this thesis.

In addition to work on the inline triplex variable linkage pump prototype, this thesis also describes structural analysis that supports the design of a cam driven radial configuration of the variable linkage pump. Challenges of this multi-body finite element analysis were identifying proper contact interfaces, generating high quality mesh, and simplifying the geometry to reduce the computational time. Further, it was not practical to model the full detail of commonly found component like bearing due to large number of contacts between rollers and raceway. The contributions of this work include constructing a systematic approach of using FEA to drive the design process, identifying proper contact interfaces, and developing a simplified bearing model. The cam driven linkage pump is used as a case study to demonstrate the application of these analysis tools.

Table of Contents

List of Tables

List of Figures

1. Background and Literature Review

1.1 Introduction

Fluid power systems have high power density compared to other forms of power transmission, making it a technology of choice for many industries and various applications [1]. However, when it comes to energy efficiency, fluid power systems suffer compared to electromechanical power systems. A study by Oak Ridge National Laboratories in 2012 determined that fluid power systems in the U.S. consume between 2.2 and 2.9 quadrillion BTUs of energy (quads), representing nearly 3% of the total energy consumed in the country. The efficiency of these systems varies from 6% to 60% with an average efficiency of 21% [2]. Inefficient flow control through metering valves is one of the prime reasons for the low system efficiency.

While variable orifice valves are inexpensive and provide precise control, they are inefficient because of throttling losses across the valves. Alternatively, stationary applications can use variable frequency drives to control the shaft speed of an electric motor coupled to a fixed displacement pump to control flow rate. While being an efficient solution, variable frequency drives are limited by high cost and the reduced motor life [3]. On the other hand, variable displacement pumps are quite attractive over variable orifice valves to regulate speed, because of reduced energy loss and less heat generation [4].

Axial piston pumps, bent axis pumps and vane pumps are the most commonly used variable displacement pumps. Axial-piston pumps consist of a set of pistons that are fitted within a rotating cylinder block and driven by an angled swash plate as shown in Figure 1.1(a). The angle of the swashplate determines the piston displacement and is varied to adjust the output of pump. These pumps require a leakage path from the pumping cylinder to the swashplate in order to create a hydrostatic bearing in the piston-slipper and slipper-swashplate interfaces, leading to a large leakage energy loss. Because this energy loss does not scale with displacement, the efficiency of these pumps is significantly reduced at low displacements [5, 6].

Bent-axis piston pumps operate similar to axial piston pumps, but rather than the swash plate being at an angle, the pistons and the cylinder block are at an angle as shown in Figure 1.1(b). They tend to have higher efficiency than axial piston pumps, but they also tend to be slightly larger for a given displacement [7]. They are not widely used compared to axial piston pumps because of their high costs, reliability issues, and their inability to support a through-shaft design [3]. Vane pumps generate flow using a set of vanes, which are free to move radially within a slotted rotor that rotates in an elliptical chamber as shown in Figure 1.1(c). While vane pumps are quiet, they cannot achieve the high pressures as piston pumps.

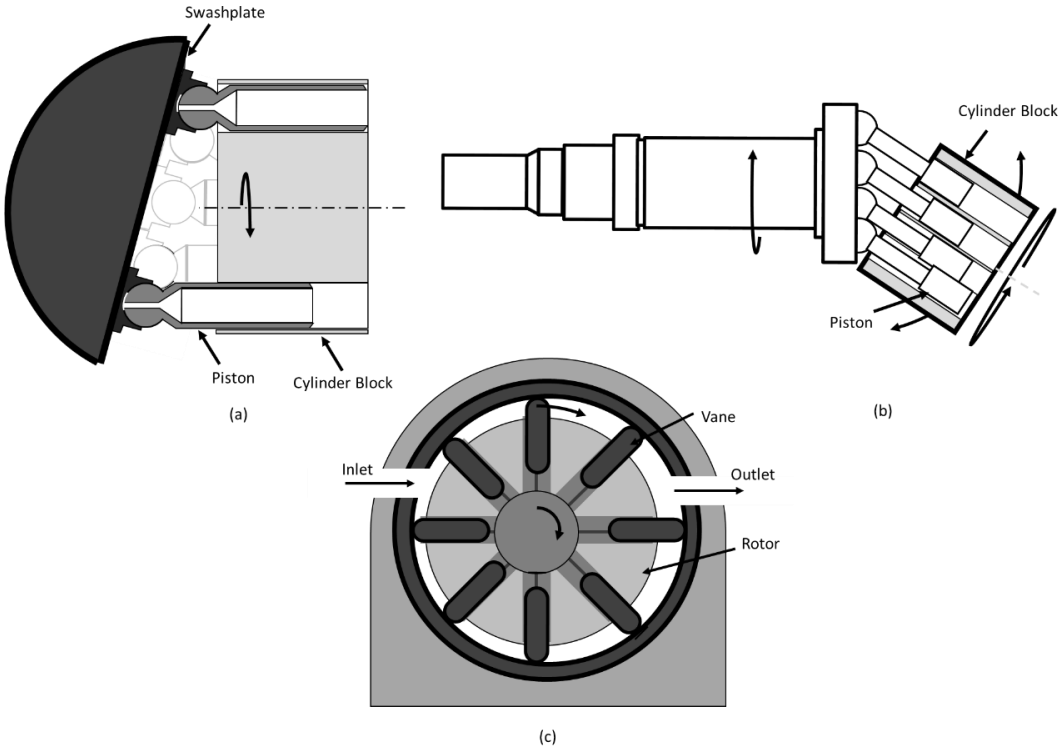

Figure 1.1 Variable displacement pump architectures (a) Axial piston pump (b) Bent axis piston pump (c) Vane pump [3]

A lot of research has been done to improve the efficiency of above mentioned variable displacement pumps [8-11]. However, their efforts led to improvement in efficiency at high displacements. Little work has focused on improving the efficiency at low displacements until recently when Wilhelm and Van de Ven synthesized a novel adjustable six bar linkage to act as a driving mechanism for the variable displacement linkage pump (VDLP) [12-18].

1.1.1 Crankshaft driven variable displacement linkage pumps

Revolute joints with rolling element bearings are more efficient than the hydrodynamic planar joints of a swash plate pump due to linear relationship between energy loss and relative velocity of components. Therefore, a pump that purely uses rolling element

bearings in a crank-slider linkage has the potential for high efficiency. If a crosshead bearing design is used, the working fluid of the pump can be separated from the mechanism, resulting in a more versatile design. Recognizing the inherent advantages of crank-slider linkage pumps, Wilhelm and Van de Ven synthesized a six bar adjustable linkage, depicted in figure 1.1, for use as a variable displacement pump [13]. As the input crank rotates, the coupler link causes the rocker link to oscillate, and the connecting rod transfers this oscillating motion to the slider link. The displacement of the slider can be changed by adjusting the position of ground pivot of rocker along an arc shown in Figure 1.2(a). The center of this arc corresponds to a point on coupler curve when crank and coupler are collinear as shown in Figure 1.2(b). The mechanism is designed such that the piston maintains a constant top dead center position independent of stroke. Because of this and in contrast to other pump designs, the unswept volume of the proposed pumping chamber remains constant independent of displacement. Furthermore, the stroke is adjustable to zero travel of the slider, which corresponds to zero pump displacement.

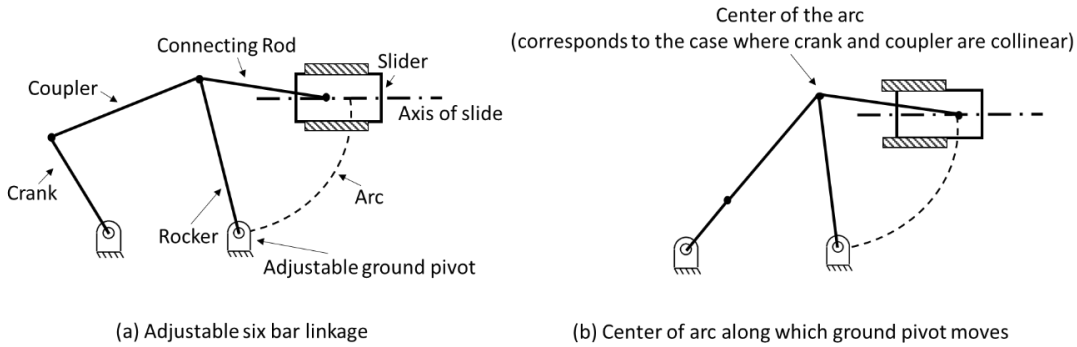

Figure 1.2 Adjustable six bar linkage for use as a variable displacement pump

Wilhelm and Van de Ven demonstrated the VDLP concept with an 8.7 cm^3/rev single cylinder prototype [14]. The prototype, depicted in Figure 1.3, was designed to handle 5 MPa pressure. They developed and experimentally validated a kinematic model and a mechanical energy loss model. The dominant energy loss in the prototype was the Coulomb friction in the bronze bushings. However, by extrapolating the model to low-friction rolling element bearings, which have an equivalent dynamic coefficient of friction of 0.005, they predicted that the VDLP would have efficiencies greater than 90% for displacements greater than 10% for the majority of operating conditions.

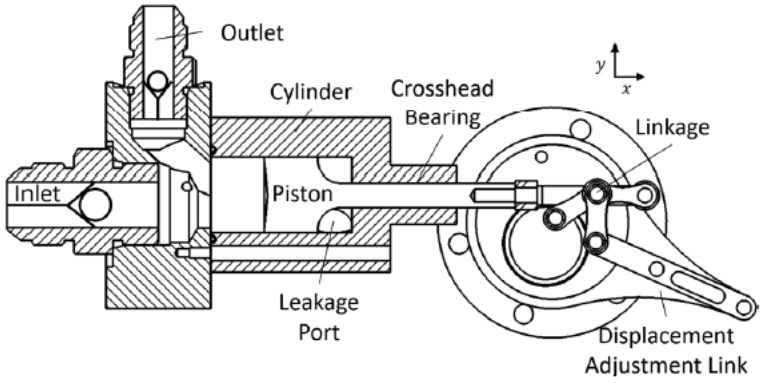

Figure 1.3 Single Cylinder variable displacement linkage pump used by Wilhelm and Van de Ven for experiments [14]

Based on the model prediction, Wilhelm and Van de Ven designed an 8.5kW, 21 MPa, 6.75 cc/rev triplex check-valve VDLP with links that incorporate roller bearings to improve efficiency [15], as depicted in Figure 1.4. This second generation pump was optimized for its kinematics and fluid dynamics together to improve both the pump performance and to control the size of the linkage mechanism. In order to reduce the number of bearings and the axial length of the pump, duplicate links were avoided when possible. As a result, most of the pin joints were loaded in single shear.

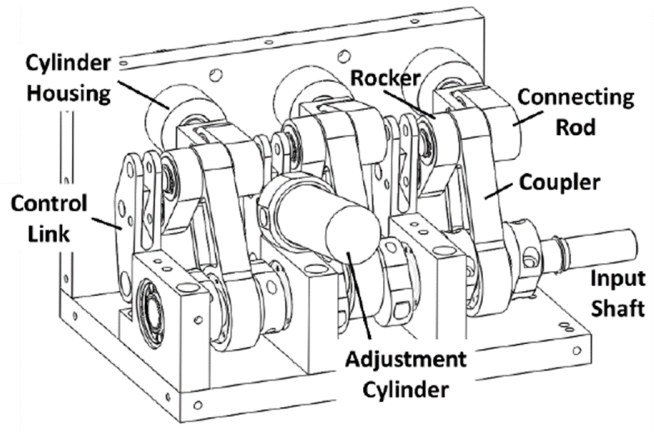

Figure 1.4 Second generation single shear triplex linkage pump designed by Wilhelm and Van de Ven [15]

Experiments conducted by Wilhelm and Van de Van showed that the mechanical efficiency of the second generation pump was greater than 90% at all measured displacements at pressures above 5 MPa and shaft speeds above 600 RPM, with the highest mechanical efficiency measured being 98% at 7 MPa and 40% displacement [16]. The mechanical efficiency trended upwards with increased pressure while the volumetric efficiency trended down with increased pressure, as depicted in Figure 1.5. The volumetric efficiency of the second generation prototype was limited by poorly performing check valves and out-of-plane deflection of the linkage due to the single shear joints that reduced the piston displacement.

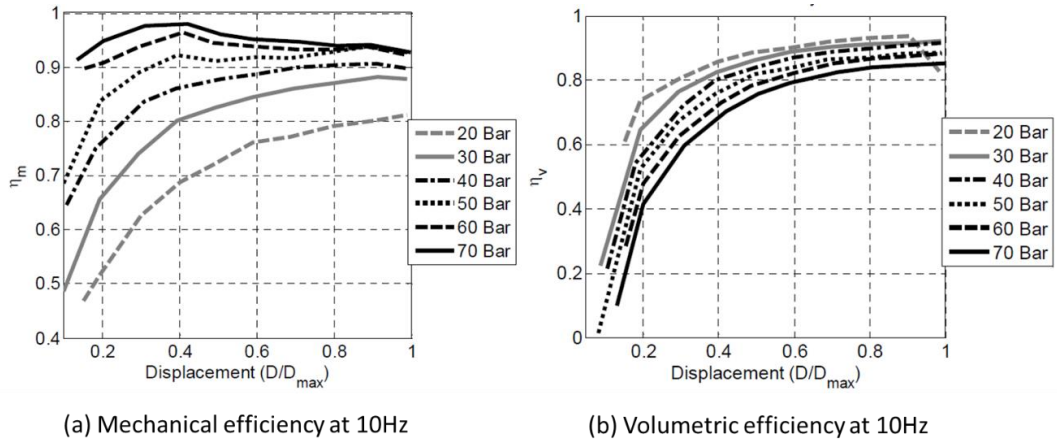

(a) Mechanical efficiency at 10Hz

(b) Volumetric efficiency at 10Hz

Figure 1.5 Mechanical and Volumetric efficiency of second generation triplex linkage pump prototype at 10Hz [15]

Continuing the work of Wilhelm and Van de Ven, a third generation VDLP was designed to address the limitations of the first two generation prototypes. Design and structural analysis of the third generation three cylinder pump are presented in this thesis.

1.1.2 Cam driven variable displacement linkage pump

Building on the concept of crankshaft driven variable displacement linkage architecture, Wilhelm and Van de Ven proposed a more compact, cam driven version of the linkage pump [17, 18]. In the cam driven pump, depicted in Figure 1.6, the crank and the coupler of variable displacement linkage mechanism presented in figure 1-1 are replaced by a cam and roller-follower. Since the fundamental kinematics of the cam driven VDLP are the same as the crankshaft driven VDLP, it retains all the benefits, including achieving true zero displacement, high efficiency joints, insignificant leakage and maintaining constant top dead center position of piston regardless of the displacements. The resulting cam driven VDLP is more compact and lightweight. Further, if a multi-lobe cam is used, there will be multiple piston strokes per revolution of the input shaft, effectively acting as gear ratio.

This increases the pump displacement per revolution and increases the volumetric efficiency at low shaft speeds. The profile of the cam can also be designed to control pumping characteristics such as torque or flow ripple.

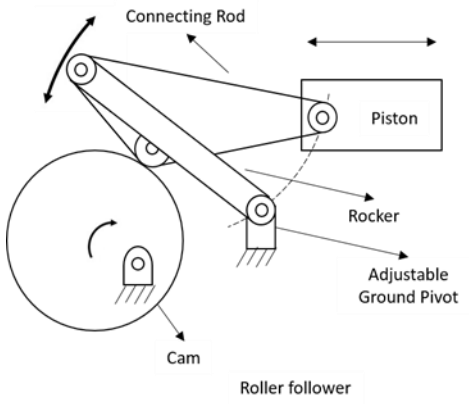

Figure 1.6 Schematic of cam driven adjustable mechanism for variable displacement [18]

In the cam driven pump, duplicate links were avoided to reduce the size and manufacturing costs of the pump, resulting in a single shear arrangement of links, similar to the second generation crankshaft driven pump. Finite Element Analysis (FEA) was carried out on the multibody cam pump assembly during the design stage to enhance the stiffness of pump assembly, thereby improving the volumetric efficiency. Various ways to approach multi-body linkage assembly FEA simulations, identifying proper contact interfaces to avoid convergence issues, and the method of using the analysis results to drive the design process are all contributions of this thesis.

From the view of computational cost, it was not feasible to model the full detail of the multiple rolling element bearings in the linkage assembly due to the large number of contacts between the individual rollers and races. Thus, it was necessary to use a simplified bearing model that provides the correct overall stiffness with lower computational expense.

Emil Claesson developed a simplified rolling element bearing model that captured the stiffness of the bearing partly or entirely with non-linear spring elements [19]. Claesson developed three different models of varying complexity to predict correct stiffness for radial and axial displacements, misalignment, and deformation of the rings. However, the models made use of many coupling constraints[1] and spring elements at specific nodes, which can be defined only by using scripting languages, thereby increasing the time for setting up the bearing model. Further, a fine mesh is needed on the inner and outer rings for the problem to be stable and to avoid convergence issues. Claesson made use of force-displacement relations developed by Houpert [20] for non-linear spring elements. However, those relations are valid only for two remote stress free points in the rings and the rollers. Hence, the spring-stiffness values had to be readjusted and calibrated against reference results from complete FE-models, increasing the overall amount of time to setup the bearing model.

There is a need for sufficiently accurate bearing models with minimal complexity and are numerically stable to decrease FEA computational time. To address this need, a simpler and computationally inexpensive bearing model that uses a bushing with fictitious properties similar to that of a needle roller bearing is presented in this thesis.

[1] kinematic coupling constrains the motion of the coupling nodes to the rigid body motion of the reference node

1.1.3 Dynamic reciprocating seals for pumping slurry

Slurries, two-phase solid-liquid mixtures, are encountered in many industries where they are referred to by various names: sludges (sewage and waste), pulps (paper industry), muds (oil drilling industry), dispersions (chemical industries), and broths (biotechnological industries) [21]. As conventional variable displacement pumps, like axial and bent axis pumps, lubricate the pumping mechanism with the pumping fluid, they cannot be used to pump slurries unless exotic materials and coatings are used [22]. Linkage pumps have an advantage over these pumps as the pumping fluid can be separated from the lubricating fluid by using a crosshead bearing.

Industrial slurry pumps are sub-divided into rotodynamic (centrifugal) and positive displacement pumps (piston, plunger and diaphragm pumps). Most rotary slurry pumps use packed glands (also called as compression packings) seals with either clean water flushing or grease lubrication [21]. Plunger pumps are fitted with a flushing system for more abrasive duties. Some high-pressure piston and plunger pumps use composite rubber and fiber packings, while others have synthetic rubber (e.g. “Viton”) rings [23].

However, packed glands and mechanical seals have many disadvantages. Packed glands result in increased friction and leakage [21]. The average leakage rate of packed glands when used for pumping water is 20 to 60 drops per minute [25]. Even though mechanical seals have lower leakage rates compared to packing glands, they result in higher initial cost

due to the tighter tolerance and smoother surface finish required (0.08 to 0.4 micrometer). In addition, they require more attention to detail during assembly to avoid damage.

Diaphragm seals have many potential advantages compared to the above mentioned seals for reciprocating applications. While flat and dished diaphragms have a relatively limited stroke, rolling diaphragms permit a large range of motion [24]. Their advantages include:

i. No friction and low wear because of rolling movement
ii. No lubrication required
iii. Negligible leakage
iv. No breakout force on startup
v. No stick-slip effect for low speed operations

However, if diaphragm failure occurs, it can be sudden and catastrophic, compared with the gradual decay of seal performance as wear occurs in other reciprocating seals. Further, the pressure withstanding capability of rolling diaphragm seals is less than other seals, limiting the applications to which these seals are applied. No significant research has been done to improve the design of rolling diaphragm seals since Bellofram Corporation and Phillips National Laboratory designed these seals in early 1960's [26, 27]. Considering the advantages that Rolling Diaphragm Seals (RDS) offer, a structural analysis of their behavior under various loading conditions is presented in this thesis. The objective of this study is to explore the viability of modifying the design of RDS to improve their pressure withstanding capability.

1.2 Overview of Thesis

This chapter presented background information as well as a review of relevant research on both conventional and linkage type variable displacement pumps, simplified bearing models for FEA, and dynamic reciprocating seals used in slurry pumping applications. Chapter two presents the detailed design and analysis of third generation crankshaft driven variable displacement linkage pump developed to address issues of previous generation linkage pumps. In chapter three, results of a study on structural analysis of rolling diaphragm seals and the viability of modifying their design to improve their pressure withstanding capability is presented. Chapter four develops guidelines for performing finite element analysis on multi-body assemblies, including select appropriate contact interfaces and a computationally efficient rolling element bearing model. As a case study, these methods are applied to the FEA analysis of the cam driven VDLP. Chapter five presents an overview of the contributions of this thesis and suggests future relevant work.

2. Design and Analysis of Third Generation Variable Displacement Linkage Pump

2.1 Introduction

Wilhelm and Van de Ven invented a crankshaft driven variable displacement linkage pump that has the potential for achieving high efficiency across a wide range of operating conditions. Two generations of prototypes were designed and tested to validate this concept. Experiments with the second generation pump showed that the mechanical efficiency was above 90% across the full displacement range at pressures above 5MPa and shaft speeds above 600 RPM. However, volumetric efficiency was limited due to two reasons:

i. Poorly performing check valves in the pumping cylinder resulted in reverse flow as the valve transitions from open to closed, thereby reducing the actual fluid flow out of the pump

ii. The single shear design of the three-cylinder prototype created out-of-plane forces that caused deflection of the mechanism, reducing the piston stroke and introduced additional joint friction due to thrust loads between the links

This chapter describes the design of the third generation linkage pump that addresses the issues of the previous generation pumps, while also reducing the size of pump to aid in moving this pump design towards commercialization. The author's role in the project was to perform a detailed design, coordinate manufacturing, and validate the FEA used during

the product development stage by comparing simulation results with the physical test results.

Detailed design and analysis of the pump is described in section two, followed by validation of FEA results in section three. The final section contains concluding remarks.

2.2 Detailed Design & Analysis

A set of design specifications define the operating conditions of the pump prototype. In addition to providing a test bed for experimental validation, this prototype acts as a proof of concept demonstration of the technology at real world operating pressures and displacements. The peak operating pressure of the pump was set to 24.1 MPa (3500 psi), a common industry standard. The testing facility had a variable frequency drive capable of 5.5kW, and typical electric drive motors have an operating speed of 60Hz. From the power and pressure requirements, a peak flowrate of 15.39 $\frac{l}{min}$ was calculated, assuming no losses. The 60Hz requirement dictates that the maximum volumetric displacement of the pump is 27.3$\frac{cc}{rev}$. Further, the working fluid is water and hydraulic oil is the lubricant.

2.2.1 Optimized link lengths and transmission angle

The earlier second generation prototype was optimized for its kinematics and fluid dynamics together to improve the pump performance and to control its size. However, an overly simple fluid mechanics model was used that assumed ideal behavior of the inlet and outlet check valves and the working fluid. The experiments revealed that the volumetric efficiency was affected by the fluid compressibility and valve dynamics. In response, Wilhelm and Van de Ven developed a model that captured the dynamics of the fluid in the

piston chambers, the check valves, and the discharge line of the pump [3]. The new fluid dynamics model was used in the objective function for optimizing the third generation pump for its kinematics and fluid dynamics.

The third generation pump was designed around commercially available components, especially for the pumping head components like pistons and valves. The pump was optimized for its size, flow ripple and efficiency with link lengths, piston length, piston clearance and maximum transmission angles as the parameters. Appropriate solutions to the design problem were then chosen from the Pareto front obtained from the optimization by making sure that the efficiency of the chosen solution would be greater than 85% at 20% displacement. Bearings were selected within the optimization sub-routine using data from bearing specification guides. Selection was then refined to the bearings which were readily available. The pump optimization and selection of right bearings was carried out by Dr. Shawn Wilhelm, one of the inventors of the VDLP.

The set of link lengths and angles obtained after optimization that define the kinematics of the mechanism are presented in Table 2.1. Figure 2.1 shows various links and their corresponding parameters.

Table 2.1 Optimized link lengths and angles

Parameter	**Description**	**Value**
r_3	Coupler Length	70.3 mm
r_4	Rocker Length	58.4 mm

r_5	Connecting Rod Length	58.4 mm
θ_{min}	Minimum transmission angle of base four bar	46^o
θ_s	Angle of slide	137^0

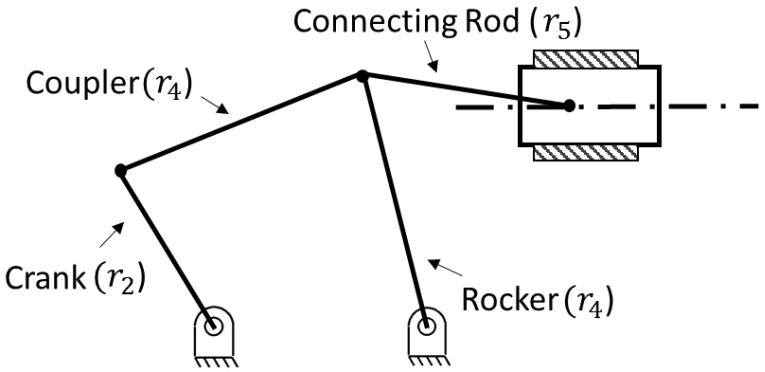

Figure 2.1 Optimized link lengths and angles

For context, a CAD rendering of the third generation VDLP is shown in Figure 2.2. The major subassemblies include:

I. *Linkage mechanism assembly* comprised of the coupler, rocker, connecting rod, slider and piston

II. *Crankshaft assembly* drives the linkage assembly by the help of electric motor

III. *Adjustment mechanism assembly* changes the location of ground pivot and thereby changes the piston displacement with the help of the control assembly comprised of the hydraulic linear actuator

IV. *Pump body (skeleton assembly)* holds all the sub-assemblies together and is built to handle the reaction forces and moments

V. *Pumping Head Assembly* comprised of the crosshead mounting block designed to handle reaction forces from the piston movement and the manifold that has all the seals, inlet and outlet valves

The intent of designing each of these sub-assemblies, engineering analysis to support the design decisions, and a brief description of how parts are connected to each other will be discussed in the next few sections.

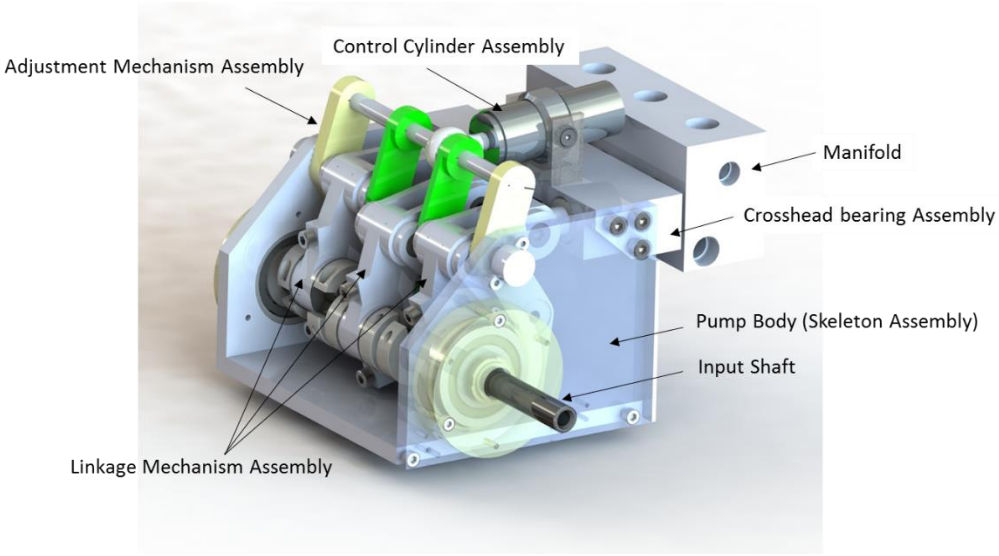

Figure 2.2 Rendered image of third generation variable displacement linkage pump

The conceptual design of the sub-assemblies was a collaborative effort between the author and Dr. Shawn Wilhelm, while the author's contribution was to analyze stresses and deflection of the sub-assemblies and its components, generate the final design, and select hardware components and co-ordinate manufacturing.

2.2.2 Linkage Mechanism Assembly

The second generation pump used a single shear arrangement of links that resulted in out-of-plane deflection of the linkage, reducing the piston displacement. In order to prevent this, links were duplicated in the third generation design to place the joints in double-shear, as shown in the Figure 2.3, where the links are numbered 1-6 and the assignments given in Table 2.2.

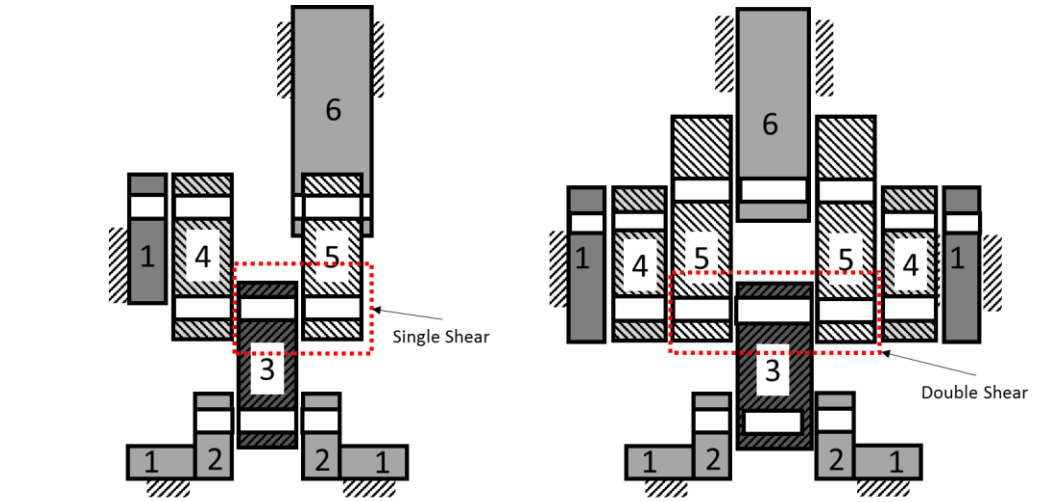

Figure 2.3 Comparison of linkage arrangement in second and third generation pump design

Table 2.2 Link Assignments

Link Name	**Assignment**
Ground Link	1
Input Crank	2
Coupler	3
Rocker	4
Connecting Rod	5
Slider	6
Note 1: Ground link includes the adjustable ground pivot, slider axis, and input shaft	

The double shear arrangement cancels all the out-of-plane moments acting on the coupler. To improve the alignment and rigidity of the assembly, the two connecting rods on either

side of coupler, shown in Figure 2.3(b), were replaced with a single H shaped connecting rod, shown in Figure 2.4.

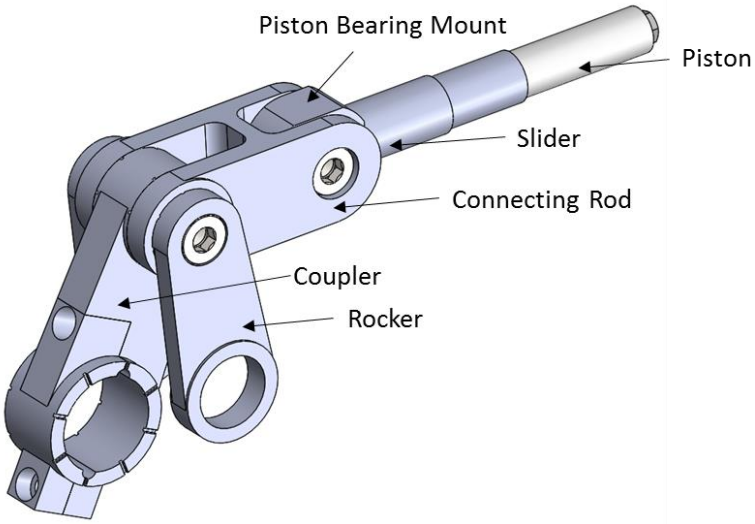

Figure 2.4 Linkage mechanism assembly

The radial loads in all of the joints are transmitted through rolling element bearings, while locational thrust forces create link to link contact. To handle this thrust load, all the links were made from 52100 bearing steel, hardened to Rockwell C60, in order to provide excellent wear resistance and fatigue strength. To reduce the friction, grooves are designed in coupler and rocker to aid in lubrication when components slide past each other and a surface finish of 0.4 microns is maintained on the faces of links sliding against each other. These grooves are chamfered to make sure that they don't act as cutting edges during the relative motion. To ease the assembly of the coupler link and crankshaft, Dr. Shawn Wilhelm developed the idea of a split coupler design, as shown in Figure 2.5. Note that the key features in the coupler are machined after appropriate matching parts are assembled. In order to prevent binding and deviation from the link lengths obtained from optimization,

tight tolerance of $\pm$0.025mm ($\pm$1 thousands of inch) is maintained on the length of rocker, coupler and connecting rod.

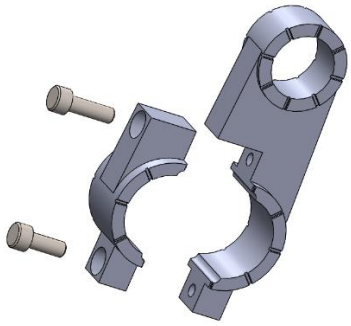

Figure 2.5 Split coupler design for ease of assembly

A design specification was set that the overall deformation of the links should be less than 0.1mm to maintain the rigidity of the linkage assembly. In order to obtain forces acting on various links, a force analysis has been performed on the linkage assembly using the method presented by Wilhelm [3]. While the coupler and connecting rod experience compressive force, the rocker experiences tensile force that varies with the angle of rotation of the crank. Using these forces, FEA was carried out to make sure that the links are rigid and stress induced is much less than the yield strength of bearing steel.

A mesh was generated on the imported CAD models in ANSYS using SOLID186 elements[2]. Dr. Shawn Wilhelm contributed to the analysis by providing the maximum compressive/tensile force that the links experience during the pump operation. The forces were applied on either end of the links and a static structural simulation was run to obtain the deformation/stress results. A mesh resolution study was conducted to make sure that

[2] SOLID186 is a higher order 3-D 20-node solid element that exhibits quadratic displacement behavior.

the results from the simulations have an acceptable level of accuracy. Table 2.3 shows a mesh resolution study as an example, illustrating the convergence trend of maximum stress in the coupler link. The mesh was refined until one of the critical results, maximum stress in the coupler in this case, converged and the analysis results were then used to determine if the deformation/stress was within the desired results. A similar approach was followed while analyzing the other links. The deformation and stress contour plots of various links under load are shown in Figure 2.6.

Table 2.3 Mesh resolution study on coupler

	Elements/nodes	Maximum stress	Solver time
Case I	4611/21966	29.812 MPa	1.27 min
Case II	32122/140410	32.095 MPa	4.33 min
Case III	57879/252388	35.709 MPa	8.55 min
Case IV	102154/437138	35.717 MPa	32.57 min

It can be observed that the maximum deformation in all the links is less than 0.01mm which indicates that the links will be rigid while the pump is in operation. Further, maximum stress induced in the links is less than 35 MPa, which is far less than their yield strength of bearing steel (2033 MPa), indicating a very high factor of safety. While these links could have been redesigned with webbing and other features to minimize the weight, the dynamic loads created by the moving links was low relative to the pressure induced forces.

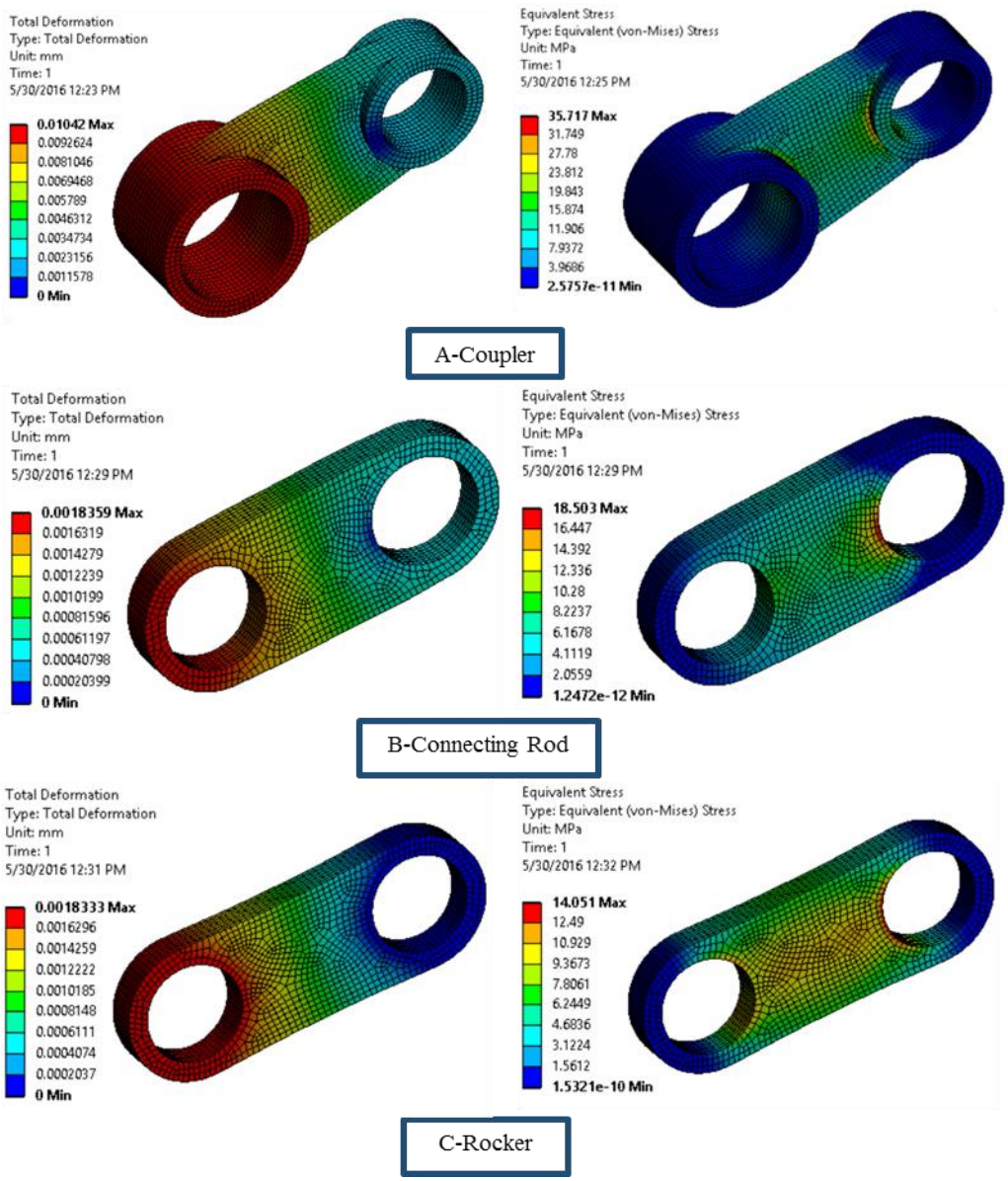

Figure 2.6 FEA of coupler, connecting rod and rocker of linkage mechanism assembly

Needle roller bearings are radially compact, high load capacity, and lightweight type of rolling element bearings. Hence, they were used everywhere in the linkage mechanism assembly. Each of the three piston linkages contains seven needle roller bearings as shown in Figure 2.7. Drawn cup caged needle roller bearings were used between coupler and

crankpin, whereas drawn cup full complement needle roller bearings were everywhere else in the linkage assembly. These two bearing types were chosen because of their ability to handle radial loads and work reliably at high rotational speeds.

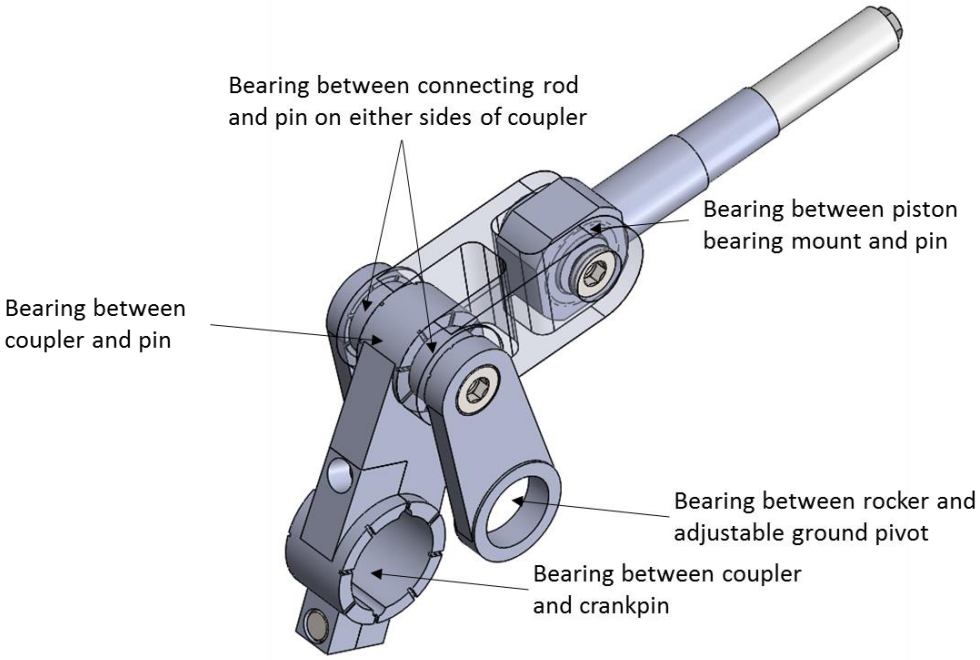

Figure 2.7 Location of bearings in the linkage mechanism assembly

Figure 2.8(a) shows how the rocker links, connecting rod and coupler link are connected. An internally threaded pin sits in shoulders of the rocker link. This pin serves as the inner race for the bearings in connecting rod and coupler. A locational clearance fit is maintained between the pin and rocker. Low head cap screws are used to preload the rocker links against the pin and set the clearances between the five links. A close running fit is maintained between rocker and connecting rods, which is essential for smooth running of the assembly. The detailed tolerance stack up analysis performed on the linkage assembly is presented in Appendix B of this thesis.

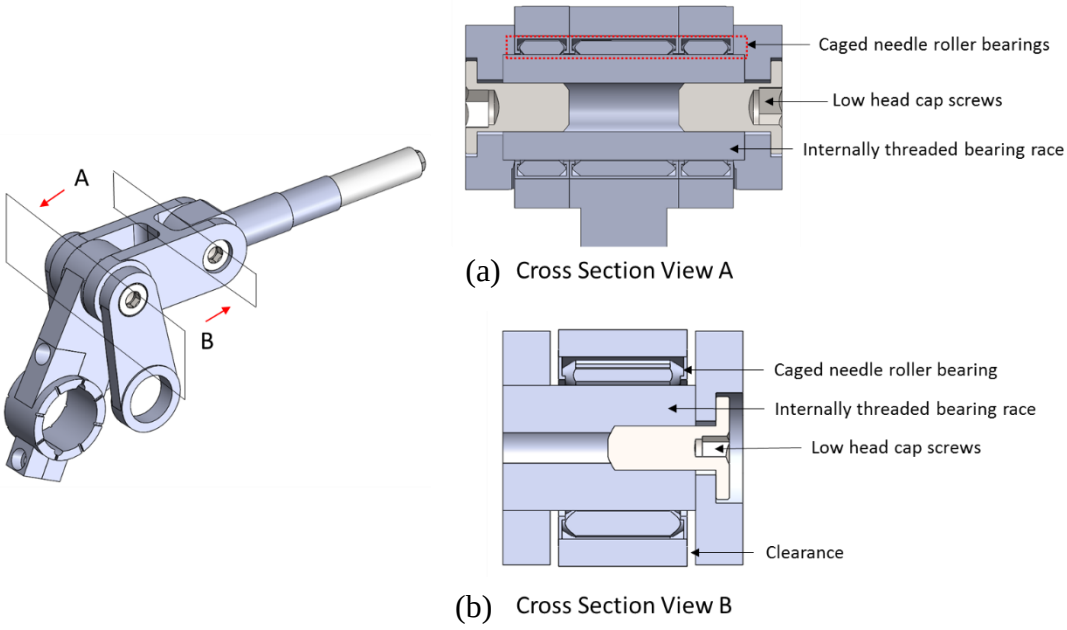

Figure 2.8 Cross section view of linkage assembly near double shear zone and piston bearing mount

Figure 2.8(b) shows how the connecting rod is connected to piston bearing mount. An internally threaded pin is inserted through the connecting rod and is kept in place by a low head cap screw from the other side. This pin acts as a bearing race for the needle roller bearing and a locational clearance fit is maintained between the outer diameter of pin and the connecting rod. In order to realize the full load carrying capacity of the bearings and to increase its life, the outer surface of both the pins is hardened to Rockwell C60 with a surface finish of $R_a<0.2\mu m$. The pin length was designed for 2.525 mm of axial clearance between the connecting rod and the piston to ensure the piston did not bind in the crosshead bearing, as determined by the tolerance stack up analysis.

Figure 2.9 shows how the piston bearing mount, slider and the ceramic piston are assembled. The slider, which slides back and forth in the crosshead mounting block, sits

on the shoulder of the piston bearing mount. The ceramic piston, is located on the shoulder of slider. The slider and ceramic piston are held in place by using a long M6 screw threaded into the piston bearing mount.

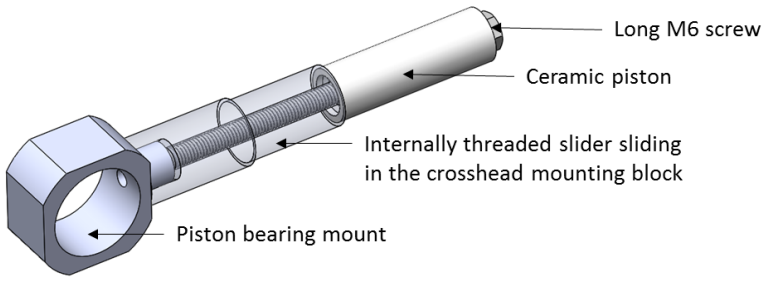

Figure 2.9 Piston bearing mount, slider and piston of linkage mechanism assembly

While the piston bearing mount and slider were made of 52000 bearing steel, the piston was made from ceramic. Benefits of the ceramic piston include (i) increased life by reducing friction and heat, (ii) protection against galling and other damage from metal to metal contact and (iii) being chemically inert, which allows the pump to work with a greater variety of fluids.

2.2.3 Crankshaft Assembly

Based on a provisional patent by Wilhelm and Van de Ven [47], a split crank-shaft was designed to accommodate rolling element bearings between the crank pin and the coupler as shown in Figure 2.10(a). The crankshaft is formed by machining flats on the individual crank pins and input shaft to create eccentric centers when mated, as shown in Figure 2.10(b). Tight tolerances of $\pm$0.0125mm and $\pm$0.025mm were maintained on the distance of the flats from the center of the crankpin and the length of the machined flats to ensure

proper alignment of crankshaft when it is assembled. To assemble the crankshaft, the roller bearings are installed over each throw and the components are placed in a fixture and then clamped together with c-clamps to create a rigid structure as shown in Figure 2.10(c).

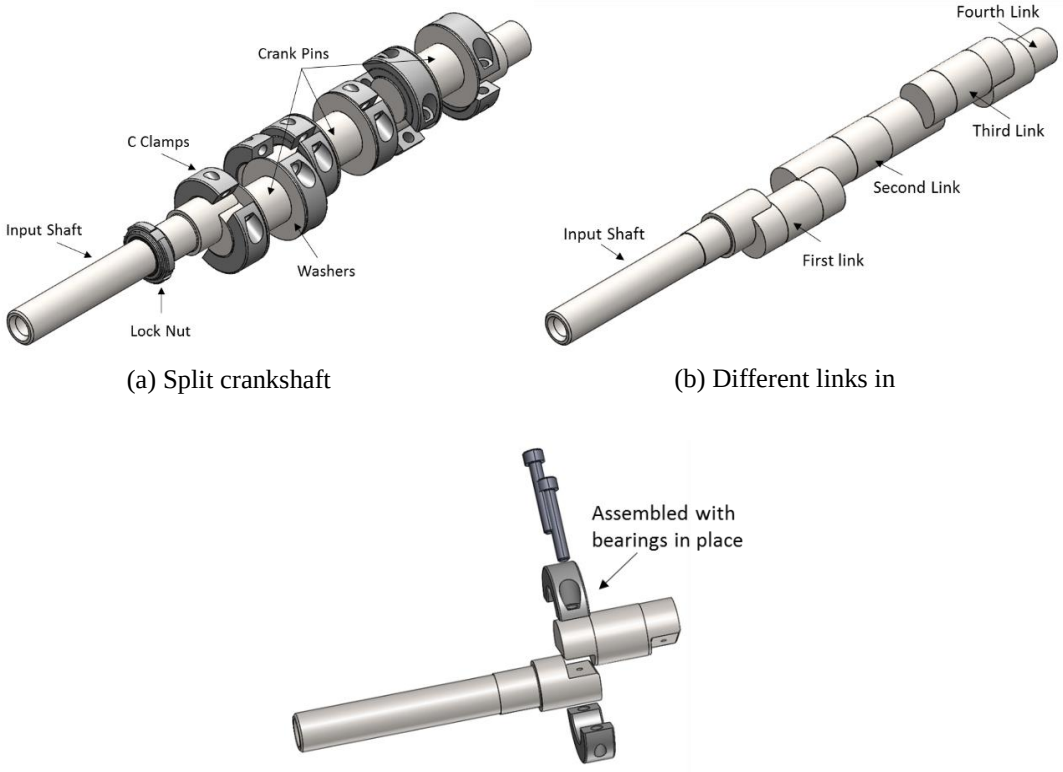

(a) Split crankshaft (b) Different links in

(c) Exploded view of split crankshaft design

Figure 2.10 Split input crankshaft design

The overall length of the crankshaft determines the total axial length of the VDLP. Thrust washers on either side of crankpin prevent axial movement of the coupler bearing and the c-clamps locate the washers. A bearing lock nut was used to load the input shaft to the inner race of the front size crankshaft bearing to axially locate the crankshaft and keep it square, as shown in Figure 2.11.

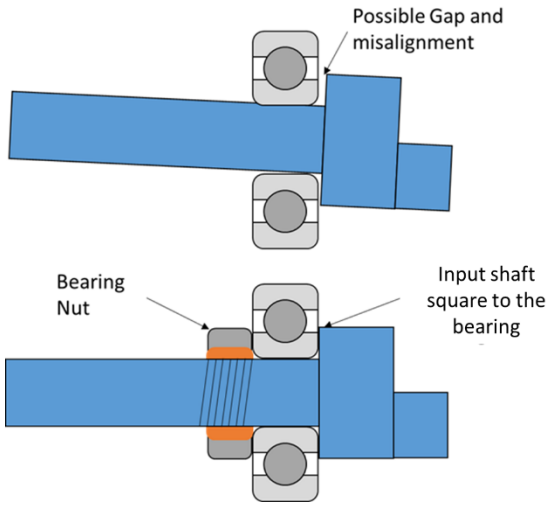

Figure 2.11 Bearing nut used to locate the crankshaft axially

2.2.4 Adjustment Mechanism Assembly

The pump displacement can be controlled by changing the position of the ground pivot of the rocker links. The adjustment mechanism assembly was designed to serve this purpose as shown in Figure 2.12. The figure depicts how the linkage is connected to the adjustable ground pivots at the rocker links. The top of the four control arms are clamped to a circular cross beam, as shown in Figure 2.13. A close running clearance fit is maintained between the circular beam and the control arms. The two control arms at the far ends of the assembly pivot on the pump body using a shoulder screw and bushing when actuated at the center of the circular rod by the hydraulic cylinder. More about the pump body and the hydraulic control cylinder will be discussed in next sections.

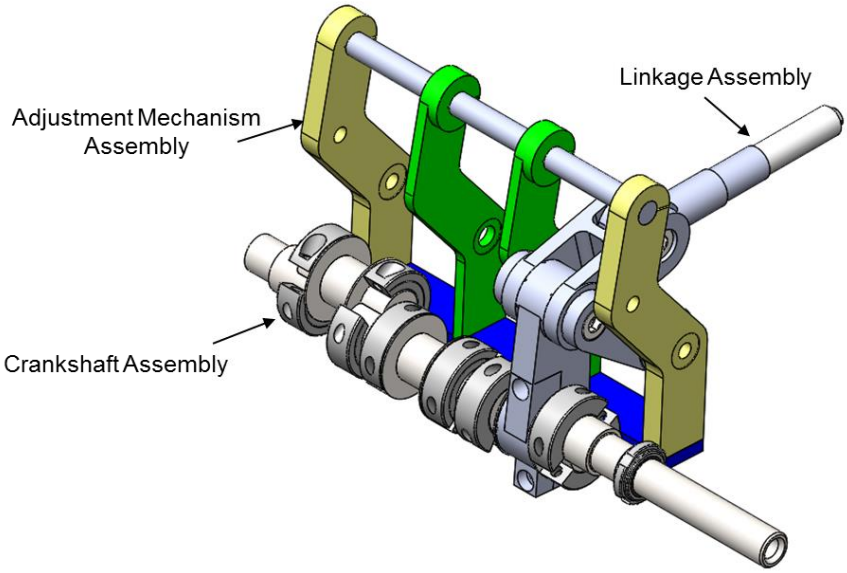

Figure 2.12 Adjustment Mechanism Assembly

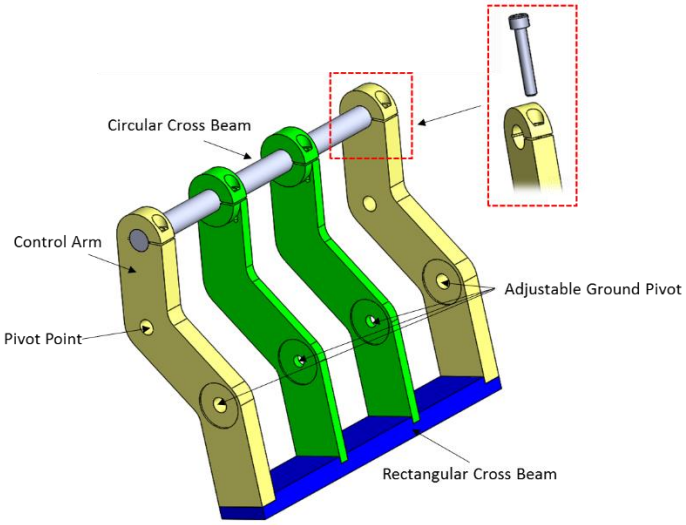

Figure 2.13 Components of adjustment mechanism assembly

Low head cap screws are threaded into the control arms at either ends of the adjustment mechanism assembly to hold rocker links 1 and 6 in place, as shown in Figure 2.14. Cap screws on one side of control arm are threaded into internally threaded pins from the

opposite side to hold rockers 2, 3, 4 and 5 in place. The figure also shows the needle roller bearings pressed into each of the rocker links.

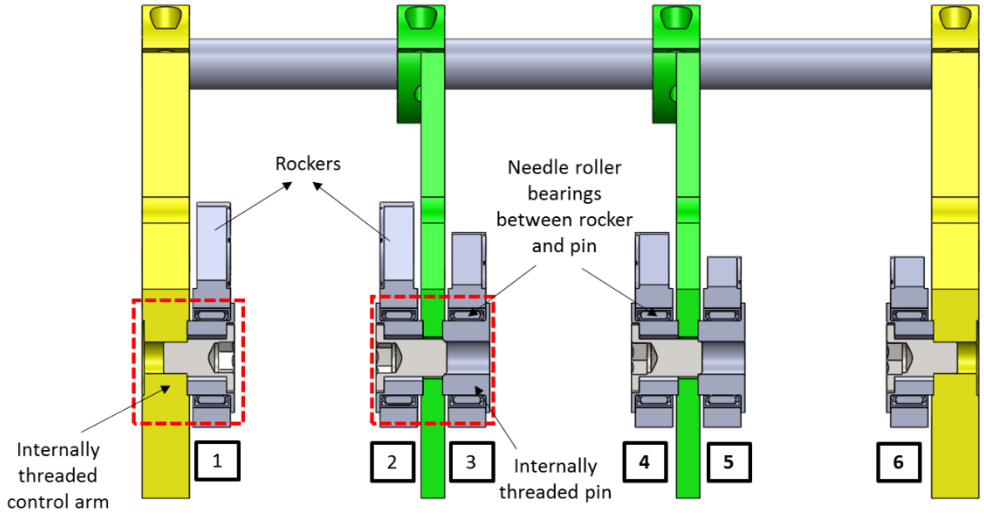

Figure 2.14 Method of connecting linkage and adjustment mechanism assemblies

Figure 2.15 shows the forces and moments acting on the adjustable ground pivot (control arms) due to the rocker links. It is vital to minimize the deformation of the adjustable ground pivot as its position along the arc as discussed in section 1.1.1 dictates the piston displacement. Any change in its position because of the deformation of adjustment mechanism assembly results in a change in the pump displacement. While the control arms are designed to handle the forces, the rectangular cross beam bolted to the bottom of the control arms is designed to withstand most of the moments. A loose transition fit is maintained between the slots in the rectangular beam and control arms.

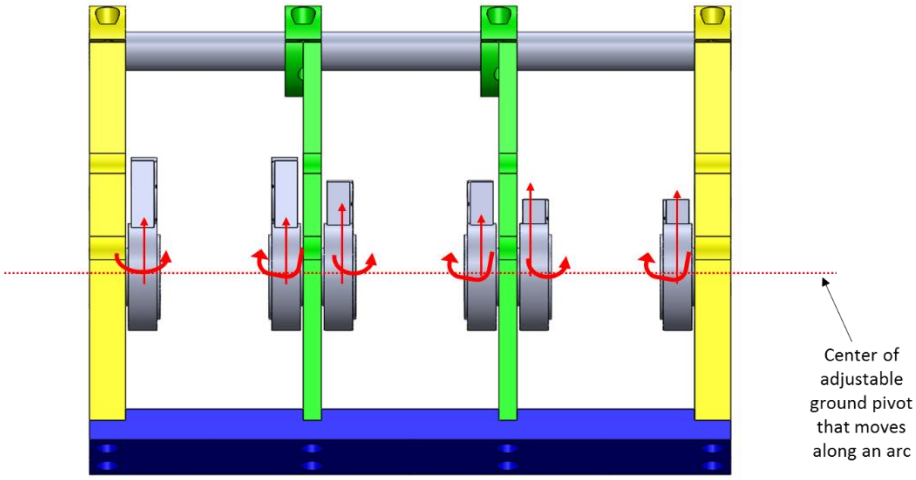

Figure 2.15 Forces and moments acting on the adjustable ground pivots (control arms) due to rockers

Design iterations were carried out using FEA to limit the maximum deformation observed near the adjustable ground pivot of the adjustment mechanism assembly. Figure 2.16 shows the boundary and loading conditions applied to the adjustment mechanism assembly geometry. While, revolute joints were defined between ground and the control arms on the either end of the assembly, the center of circular cross beam is completely fixed, indicating the location where the adjustment mechanism assembly is actuated to rotate about the pivots. The figure also shows the location and direction of action of forces acting on the assembly, as obtained from the analytical force calculations. Numerical values of the forces acting on the ground pivots that were used during the FEA simulations were provided by Dr. Shawn Wilhelm.

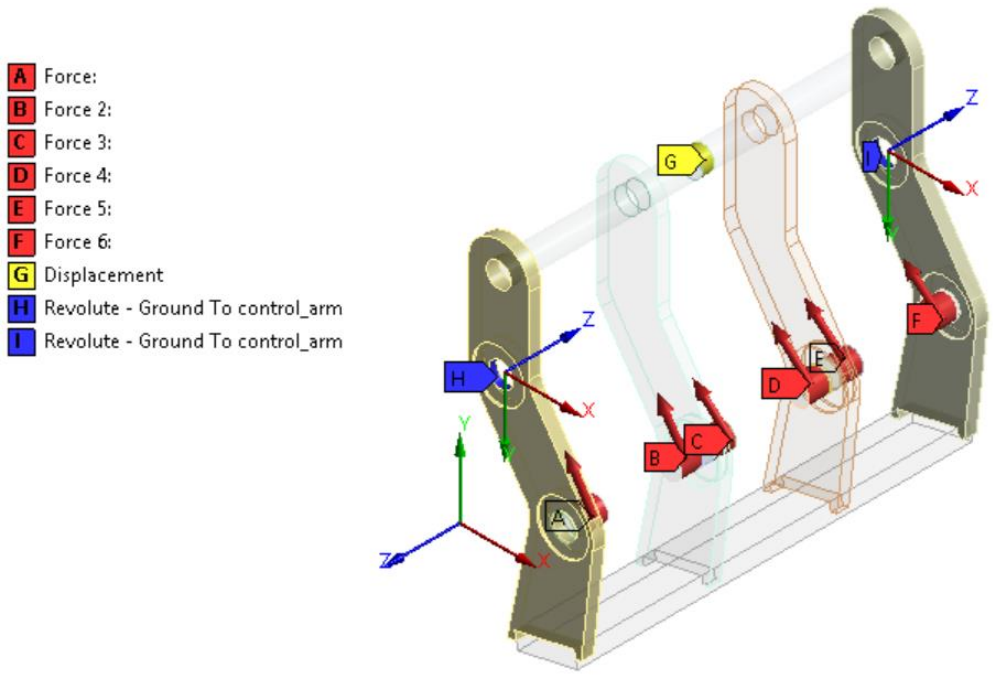

Figure 2.16 Load and boundary conditions on the adjustment mechanism assembly

A deformation contour plot of the final assembly design is presented in Figure 2.17. The design intent of bolting the rectangular beam to the control arms is to resist the moment and reduce the deformation of the adjustable ground pivots. It can be observed that the maximum deformation in the adjustment mechanism assembly is in the rectangular cross beam, while the deflection of the ground pivots is minimal.

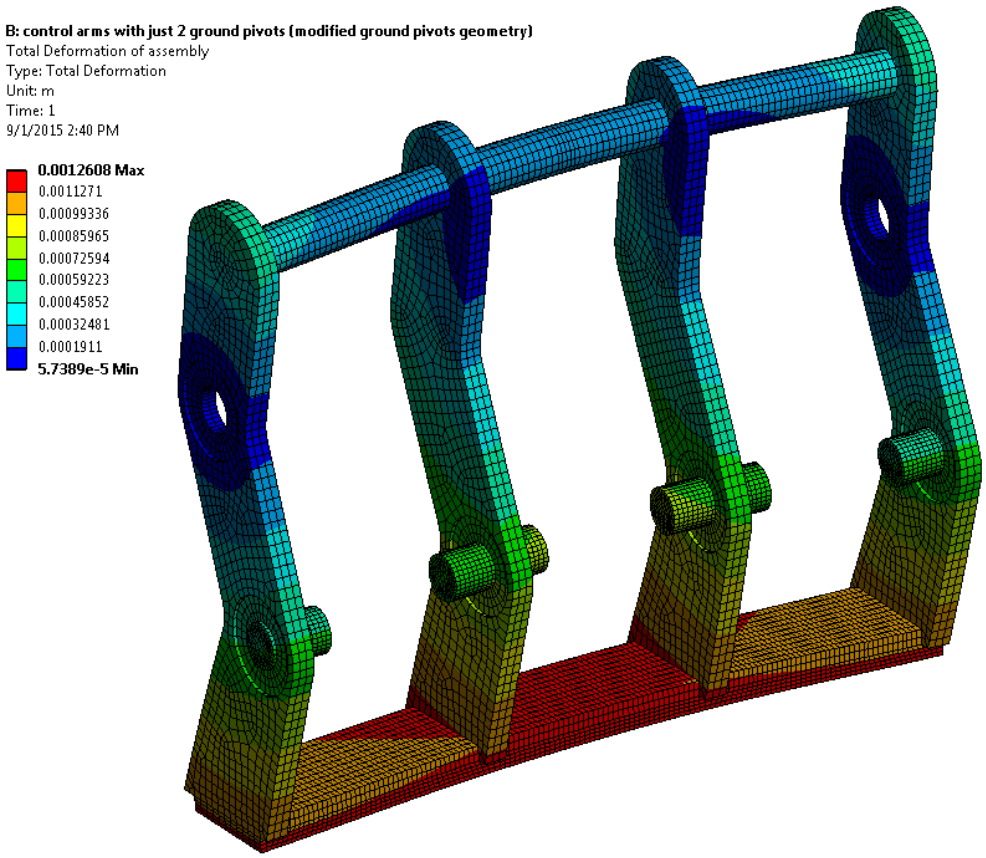

Figure 2.17 Total deformation and equivalent stress induced in the assembly

2.2.5 Pump Body

The pump body serves as an outer rigid case for the pump and also holds the adjustment mechanism assembly and the crankshaft bearings in place. It is built to handle the reaction forces and moments generated near the crankshaft bearing, adjustment mechanism assembly and crosshead mounting block.

Figure 2.18(a) shows the pump body along with linkage, adjustment and crankshaft assemblies. The adjustment mechanism is connected to the side plates of the pump body by two shoulder screws in the control arms on either ends of adjustment assembly. The pivot point of the adjustment mechanism is shown in Figure 2.18(b). The side plates, base

plate and bearing houses were all made from 6061-T6 aluminium for weight savings and stiffness.

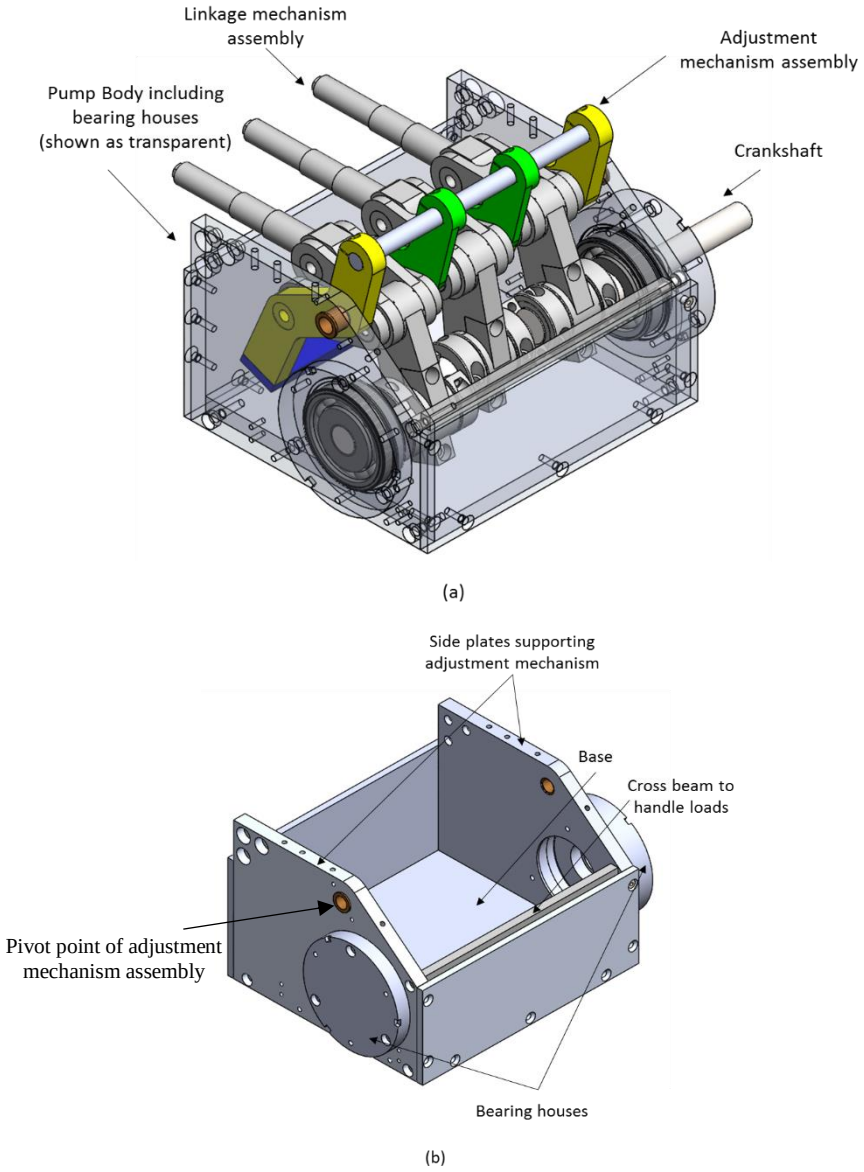

Figure 2.18 Pump body (skeleton) of third generation linkage pump

The crankshaft bearing housings are mounted on the side plates of the pump body to locate the crankshaft bearings, as shown in Figure 2.19. Grooves for the shaft seal and O-ring are also shown in the figure.

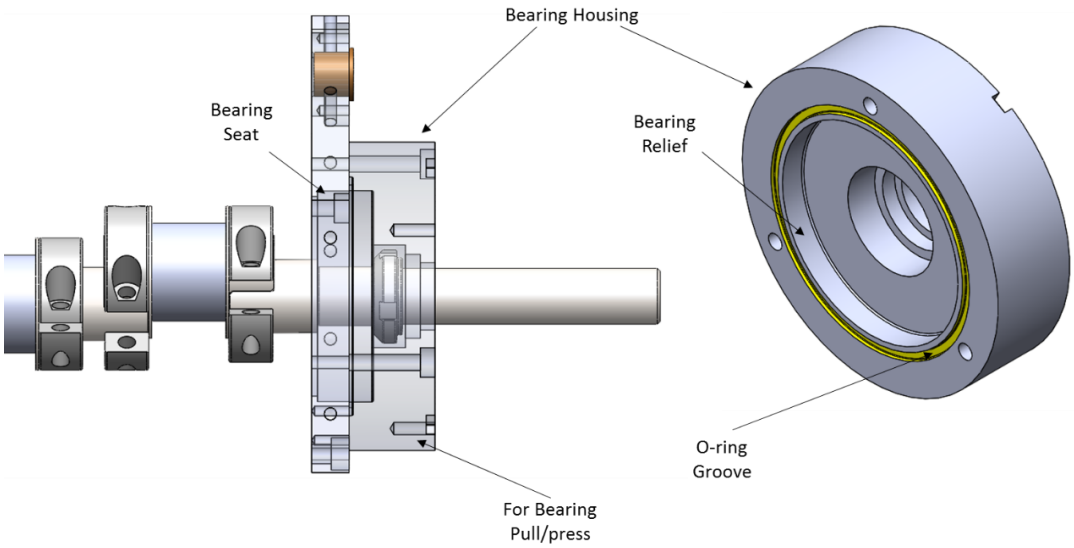

Figure 2.19 Bearing house bolted on to the side plates of pump body

The pump body was designed to minimize its weight, size, and to withstand the forces from the adjustment mechanism assembly, crankshaft bearings, and the manifold. FEA was carried out on the final design to make sure the pump body is sufficiently stiff. Figure 2.20 shows the boundary and loading conditions on the pump body FEA simulation. Forces acting on the pump body due to the adjustment mechanism assembly can be calculated by assuming that the assembly is in static equilibrium. Dr. Shawn Wilhelm provided the numerical values for the forces needed for carrying out the analysis. The results of the structural analysis presented in Figure 2.21 show that the deformation in the assembly is around 5 microns, which is sufficiently stiff to neglect deflection in the body. Further, the stress induced is much less than the yield strength of 6061-T6 aluminium (276MPa).

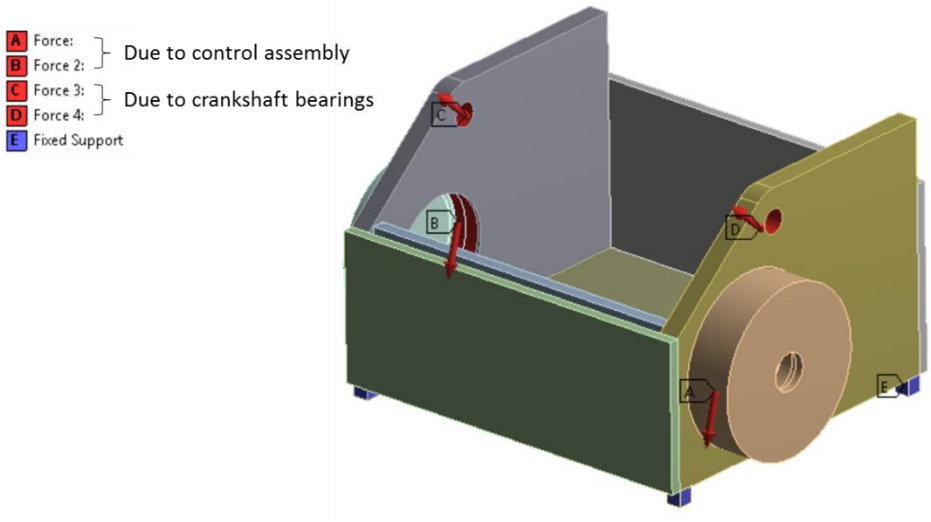

Figure 2.20 Boundary and loading conditions on the pump body

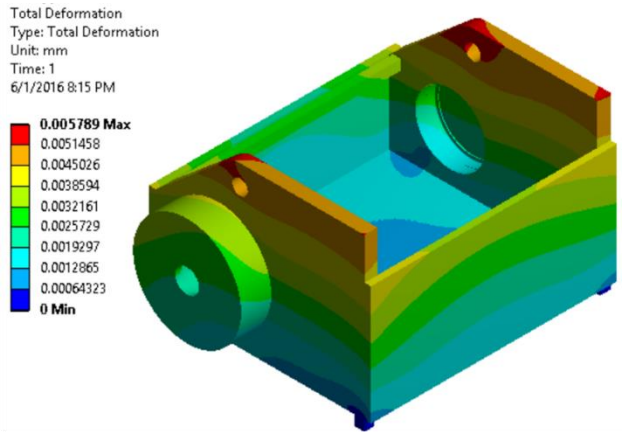

(a) Displacement

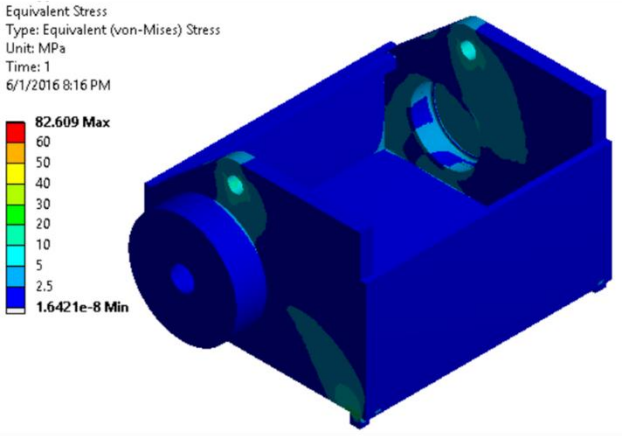

(b) Equivalent Stress

Figure 2.21 Finite element analysis of pump body

2.2.6 Control Assembly

The piston displacement is adjusted by rotating the adjustment mechanism assembly about the pivot point. The adjustment assembly is rotated using a hydraulic actuator acting either on the circular beam on the top or the rectangular cross beam on the bottom. However, the actuator required to create the required force is too large to fit inside the pump body if it were to drive the bottom rectangular beam. Hence, the control assembly has been designed such that it actuates the top circular beam, as shown in Figure 2.2.

2.2.7 Pumping Head Assembly

The pumping head assembly is comprised of the crosshead mounting block and the manifold, as shown in Figure 2.22. The crosshead mounting block separates the pumping fluid from the lubricating fluid and is designed to withstand reaction forces due to piston movement. It is bolted to the side plates of the pump body. Drill bushings are used as the linear crosshead bearings for the pistons.

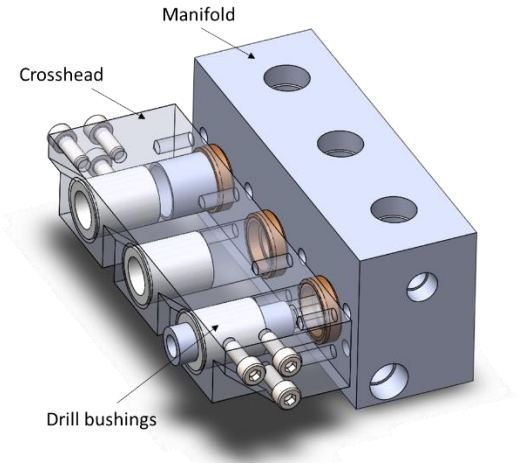

Figure 2.22 Pumping head assembly of the linkage pump

The manifold, which has all of the seals and check valves, is bolted to the crosshead block, as shown in Figure 2.23. The manifold is made of brass, which is compatible with water and resists erosion caused by particles in the fluid. Cat Pumps V packing seals and shaft seals are the primary seals for the water and oil respectively, while a graphite infused shaft seal is used as a secondary seal for preventing both water and oil leakage.

The design of pumping head assembly and selection of the seals in the manifold was led by Dr. Shawn Wilhelm.

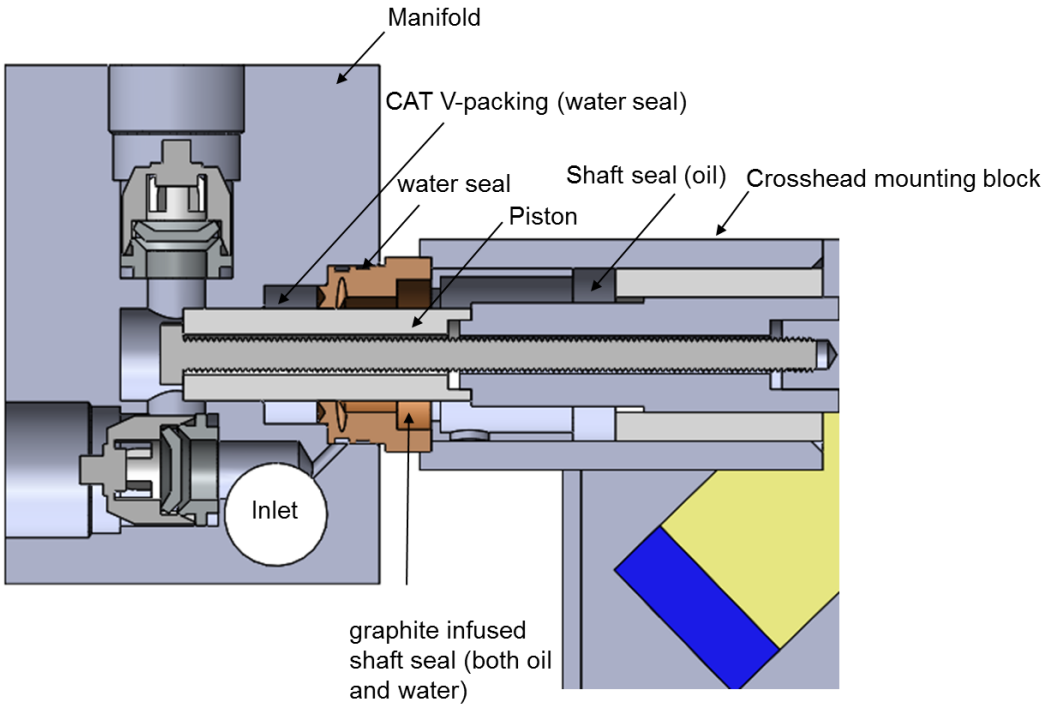

Figure 2.23 Cross section view of the pumping head assembly

2.3 Validation of FEA results

The third generation pump was manufactured, assembled and mounted to the test stand. Dr.Shawn Wilhelm and Nathan Fulbright carried out the experiments on the new prototype, while the author's role was to assemble/disassemble the pump and inspect the parts for signs of wear and loosening of fasteners.

For a given experiment, the displacement was set with the hydraulic cylinder acting on the control link. The displacement set point of the pump was measured using a CUI AMT10 capacitive incremental encoder with a resolution of 2048 steps/rev. The encoder typically uses a spline on the rotor to engage a shaft adapter. A shaft adapter was designed to engage the hex of shoulder bolt which attaches to the control assembly. An LVDT was used to measure the piston displacement vs encoder angle, thereby aiding in calibration of pump displacement.

The shaft speed was then set using the variable frequency drive and the pressure was set by adjusting the relief valve. The pump was run in this condition for 30 seconds, allowing it to reach cyclic steady state, and data from the sensors was then collected to capture multiple cycles of pumping action. Experiments were run to observe the variation of overall efficiency of the pump at different displacements, operating pressures and shaft speeds.

Experiments showed that the volumetric efficiency improved by an average of 10% from the second generation pump, demonstrating the effectiveness of the double shear linkage on reducing the axial piston deformation. It was observed that at 900 rpm and 2000 psi, the

overall efficiency of the pump was consistently around 80% above 20% displacement., thereby demonstrating a flat efficiency curve. This shows an overall improvement in the performance of new generation pump over the previous generation pump.

Experiments were conducted at 2000 psi and below with tap water as the working fluid. The only failure the pump had was when it was run at 1800 rpm. The screws of the split shaft collar between the second and third linkage mechanisms failed. A stronger split shaft collar was then used for further experimentation to avoid such failures. This component was not analyzed as part of the author's work.

In addition to demonstrating the pump efficiency and operating characteristics, an objective of the experimental testing was to validate the FEA models. While no parts were instrumented with strain gauges to measure strain or calculate stress, the rotary deflection of the ground pivot of adjustment mechanism was measured using a sensor. The rotational deflection during operation at a fixed displacement setting were directly compared to the FEA results.

FEA simulations were carried out for three different settings of the adjustment mechanism assembly, corresponding to 30%, 50% and 80% piston displacements, as shown in Figure 2.24. The results were then compared to the experimental data available on the rotary deflection of the assembly about the ground pivot.

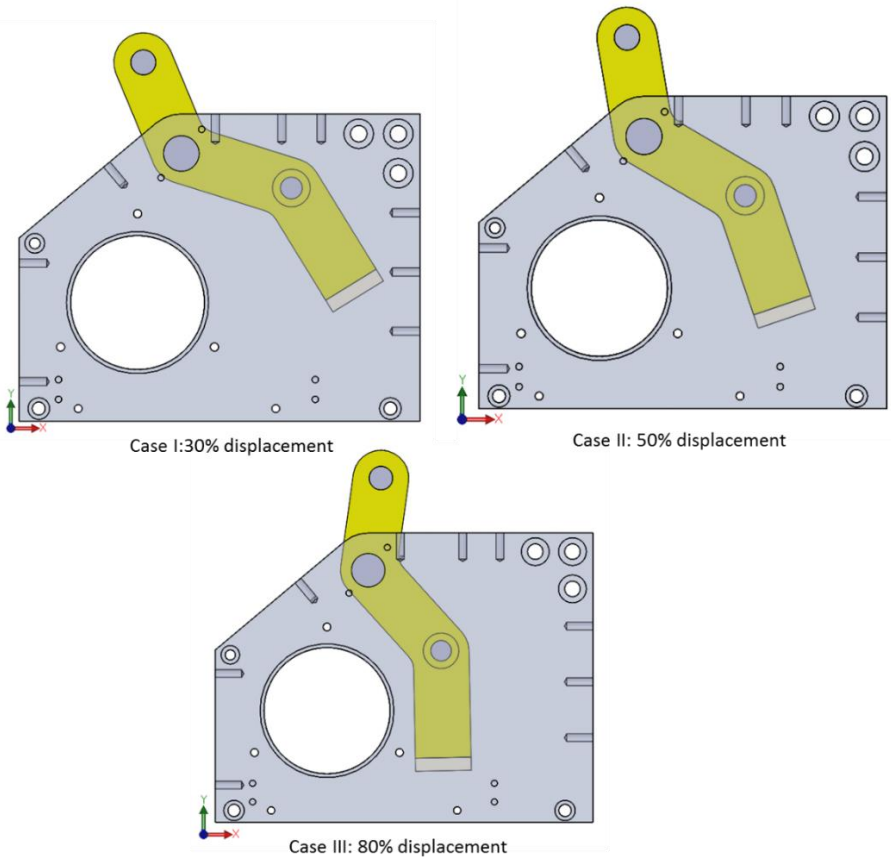

Figure 2.24 Configuration of the adjustment mechanism assembly corresponding to 30%, 50% and 80% displacements

The geometry considered for the simulations include the adjustment mechanism assembly and the side plates as shown in Figure 2.25.The entire adjustment mechanism assembly was considered to be a single body and rotates inside the bushing pressed in the side plates.

A frictionless contact was defined between the shoulder screw and the bushing as shown in the figure.

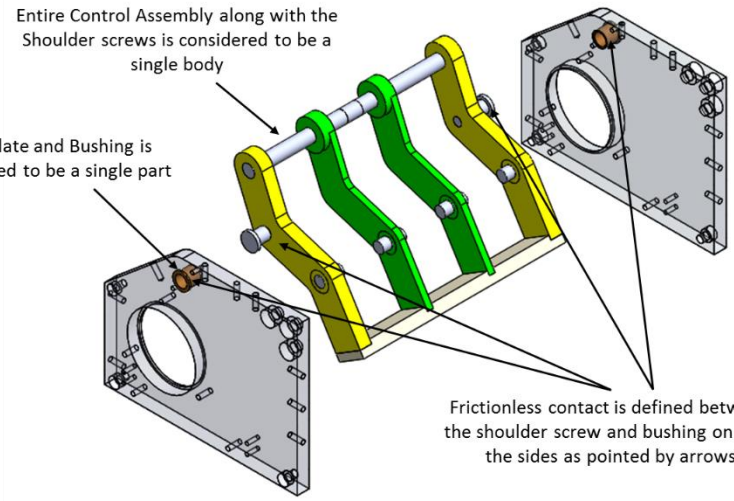

Figure 2.25 Geometry considered for FEA simulation and the contacts applied between different bodies

Mechanism force analysis [3] was used to calculate forces acting on the adjustable ground pivots (rocker ground pivots).The net moment of these forces on the entire adjustment mechanism assembly about its ground pivot, with respect to the crank angle, was calculated for the three different configurations as shown in Figure 2.26. It should be noted that these forces and moments correspond to the case where the pump is running at 2000 psi.

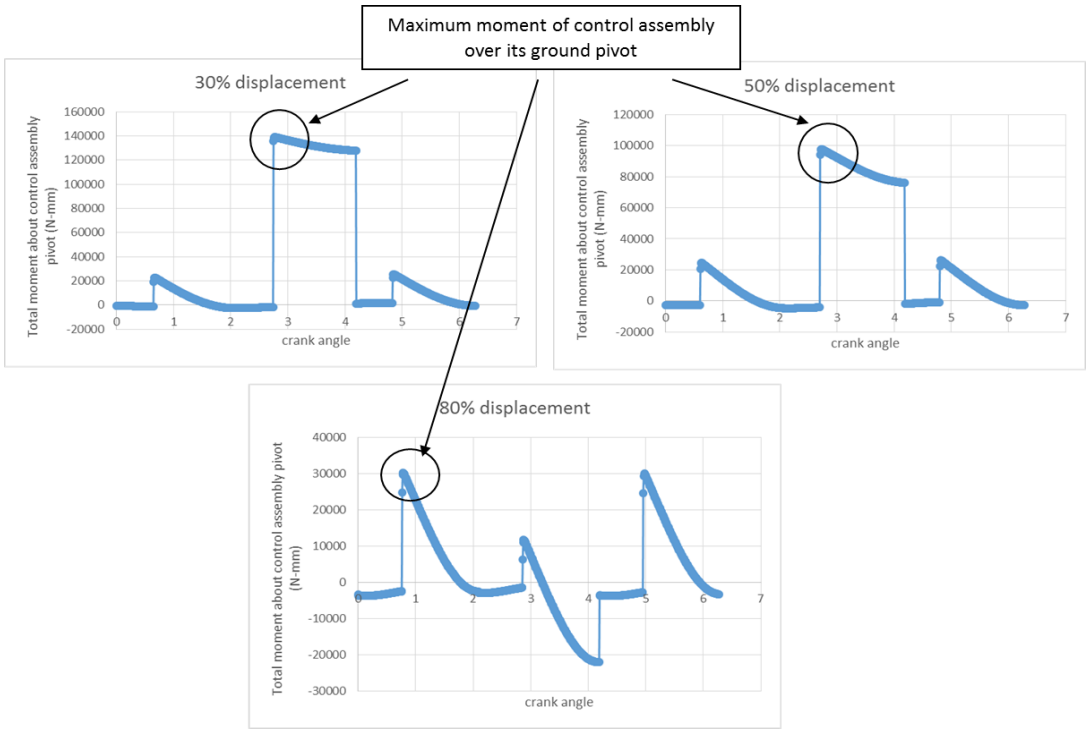

Figure 2.26 Variation of moment of the adjustable ground pivot forces on the control assembly about its pivot with the crank angle

Forces corresponding to the maximum moment on adjustment mechanism assembly about the ground pivot were applied on the adjustable rocker ground pivots during the simulations, while fully constraining the side plates. Table 2.4 shows the force values applied to each adjustable ground pivot corresponding to the maximum moment, used in the FEA simulations, which follows the naming convention shown in the Figure 2.27 for representing adjustable ground pivots of the three linkage assemblies.

Table 2.4 Forces acting on the adjustable rocker ground pivots corresponding to the maximum moment on the adjustment mechanism assembly about its ground pivot

	F1(x) [N]	F1(y) [N]	F2(x) [N]	F2(y) [N]	F3(x) [N]	F3(y) [N]
30% disp	48.9	2606.3	48.7	32.2	-450.8	-33.4
50% disp	15.0	2495	29.2	27.4	-987.1	-31.4
80% disp	8.1	1.4	2364.9	-9.1	27.8	-1885.8

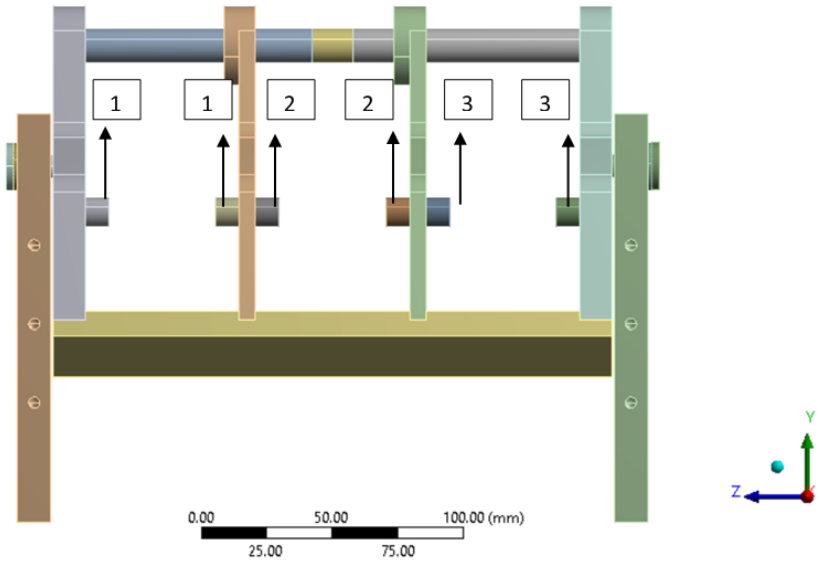

Figure 2.27 Convention used for representing the adjustable ground pivots

Figure 2.28 shows the FEA deformation results of the adjustment assembly about its ground pivot for the three different configurations. It can be observed that the deformation of the assembly in the first two configurations is more near the first linkage assembly. This is because the forces on ground pivots named “1” in Figure 2.27 are more than the other ground pivots for 30% and 50% displacements.

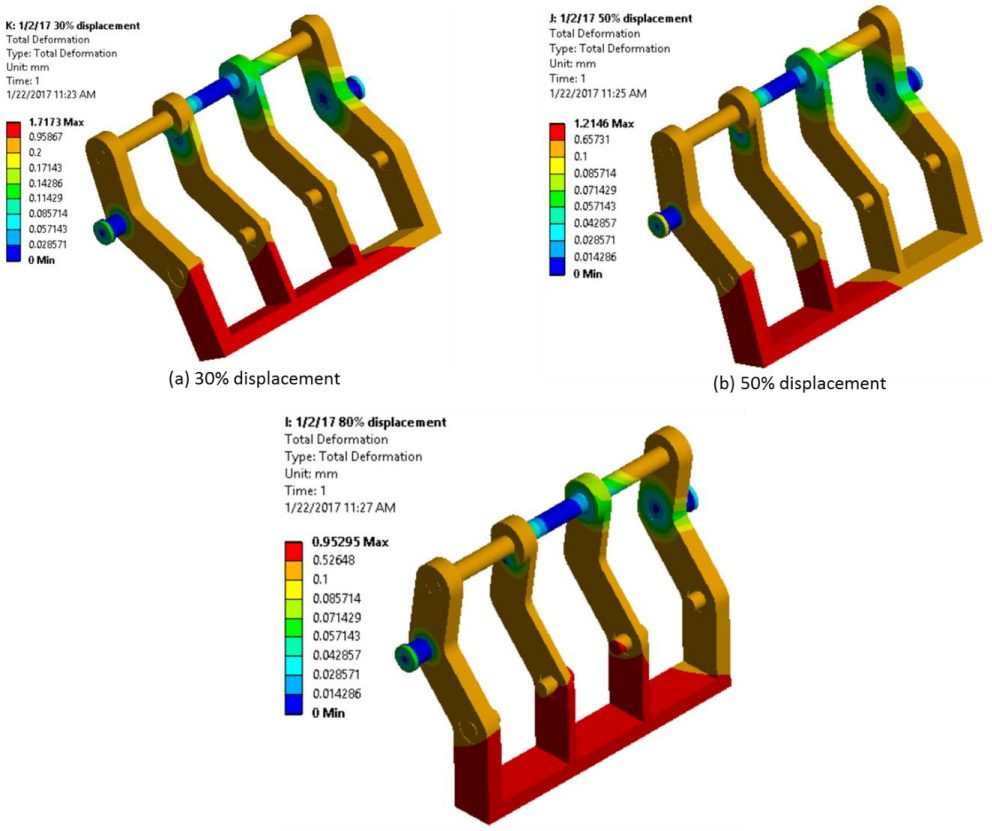

(a) 30% displacement

(b) 50% displacement

(c) 80% displacement

Figure 2.28 Deformation of the control linkage about its ground pivot for three different piston displacements

The rotational displacement of the adjustment mechanism assembly about its ground pivot is quantified by the deformation of the shoulder screws on either side of the adjustment mechanism assembly. Figure 2.29 shows the deformation of the shoulder screw in the bushings.

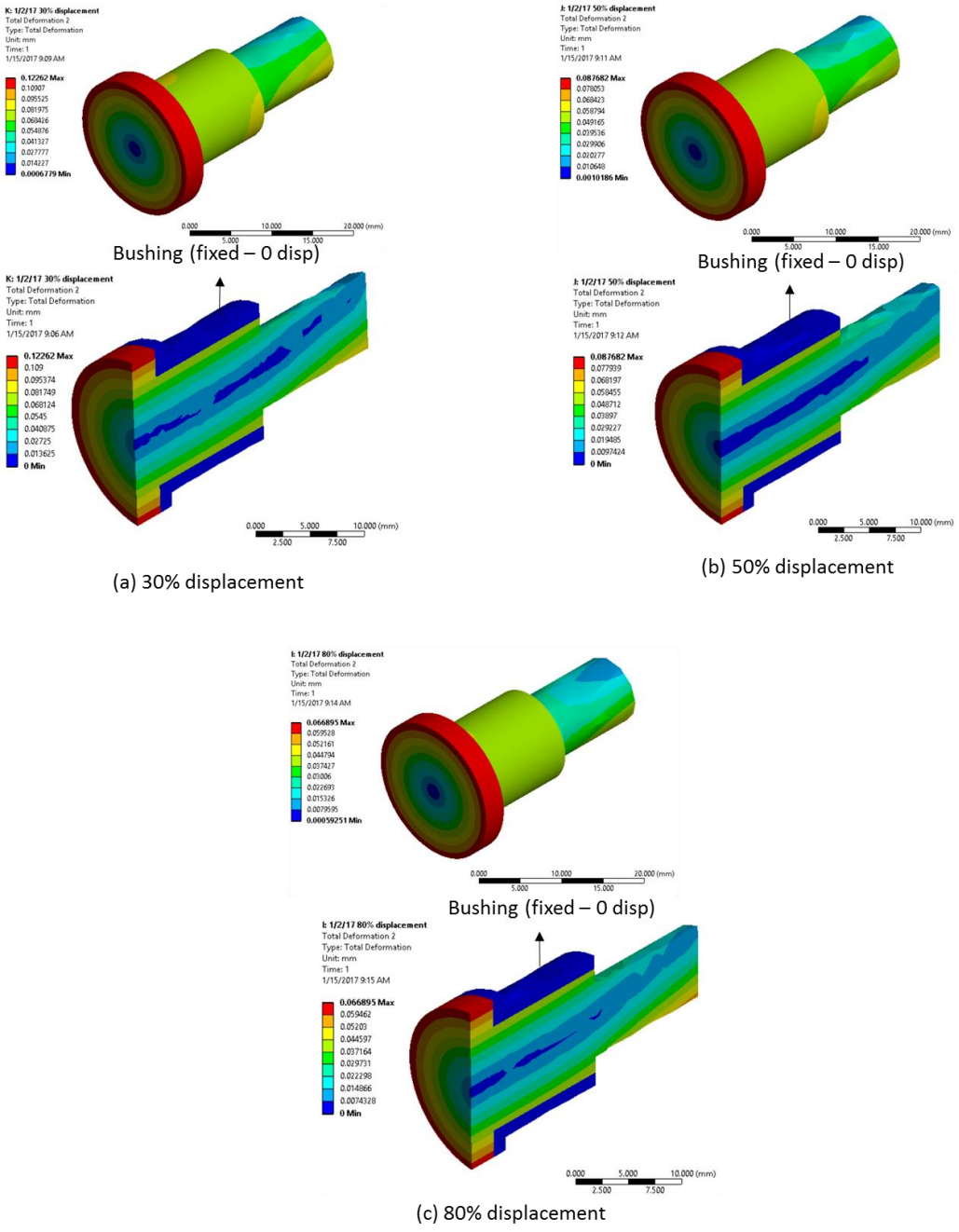

Figure 2.29 Deformation of the screw in the bushing corresponding to 30%, 50% and 80% piston displacements

One can observe from Figure 2.29 that the displacement of the pin is zero in the center and increases with the radial distance. This shows that the deformation of the screw in the

bushing is a true rotation, demonstrating that the frictionless boundary condition defined between the screw and the bushing in the FEA simulation is quite realistic. It can also be observed that the rotational displacement of the adjustment mechanism assembly about its ground pivot decreases with an increase in the piston displacement.

Figure 2.30 shows the experimentally found rotational deflection of the adjustment mechanism assembly about the ground pivot. The deflection of the ground pivot was measured by encoder at a set pressure and pump displacement. It can be observed that the rotational deflection of the assembly increases with an increase in the pump pressure. Further, it can also be observed that the rotational deflection increases with an increase in the piston displacement.

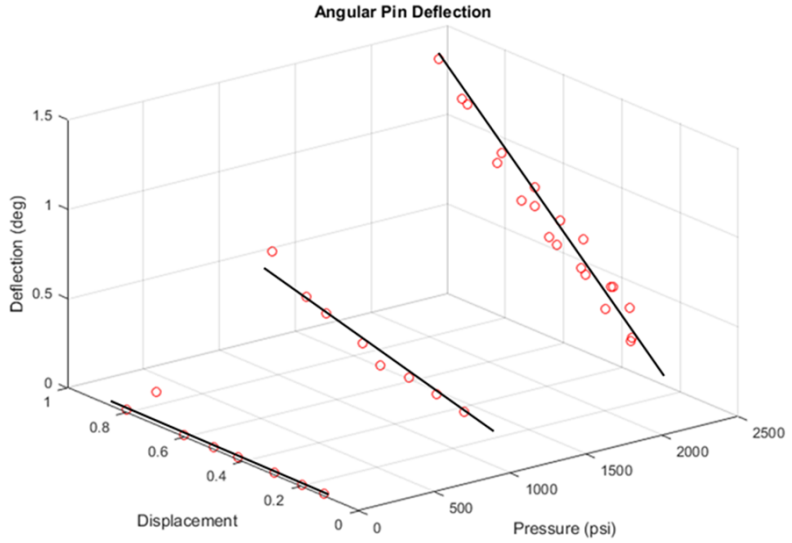

(a) Pin deflection vs. piston displacement vs. pressure

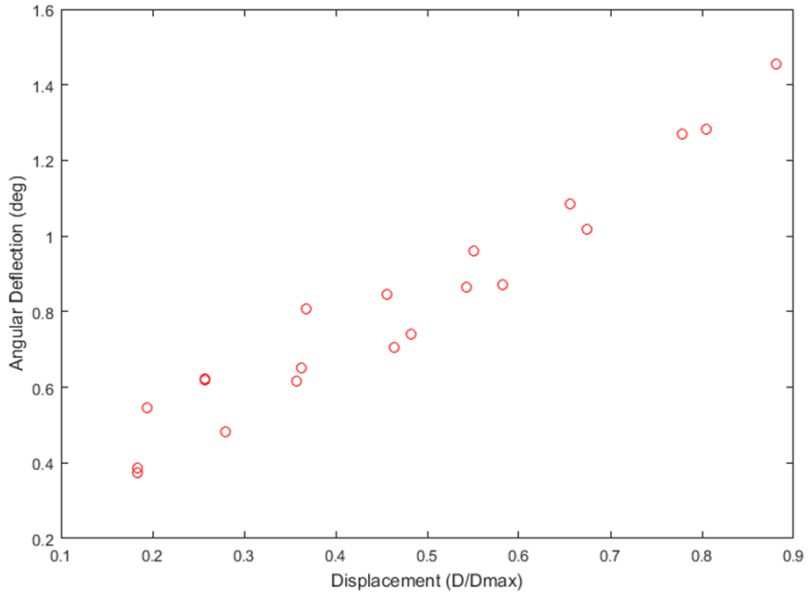

(b) Angular deflection at 2000 psi

Figure 2.30 Angular rotation of the adjustment mechanism assembly about its ground pivot

Table 2.5 compares the rotational deflection of the adjustment mechanism assembly about the ground pivot obtained through FEA and experimentally. It can be observed that the FEA results are quite similar in magnitude when compared to the experimental results. However, FEA predicts that the rotational deflection decreases with increase in piston displacement contrary to the trend shown by the experimental results, even though the results are of the same magnitude. One possible explanation for this discrepancy is that although the loads on the ground pivot increase as the displacement decreases, the direction of the force becomes closer aligned with the adjustment pivot. Slight deviations between the angle of the applied force between the FEA and the experimental pump will result in significant differences in observed rotational deflection.

Table 2.5 Comparison of experimental and FEA results at three different piston displacements

Rotation of screw in the bushing	30% disp	50% disp	80% disp
Experimental results (in degrees)	0.547	0.735	0.959
FEA (in degrees)	0.773	0.552	0.420

2.4 Conclusions

In this chapter, detailed design and analysis of the third generation 10cc/rev, 3500 psi VDLP prototype was presented. The intent of designing various sub-assemblies, engineering analysis to support the design decisions, and a brief description of how the parts were connected to each other was discussed in this chapter.

The links were arranged to place the joints in double shear to cancel out all out-of-plane moments. This helped to reduce the piston deflection and consequently showed an improvement of 10% in the volumetric efficiency compared to the second generation

prototype where the joints were in single shear. The linkage assembly and the adjustment mechanism assembly went through many design iterations using the simulation results. This made sure that the linkage mechanism and adjustment mechanism assemblies were rigid enough to prevent significant deflection and the stresses would not result in failure.

The FEA results were validated by comparing the rotational deflection of the adjustment mechanism assembly about its ground pivot predicted by the simulation with the results obtained experimentally. The experimental results validated that the FEA was predicting the correct magnitude of deflection, while slight differences in trends were seen with changes in displacement. In addition, the experiments showed that the overall efficiency of the pump was around 80% above 20% displacement, with volumetric efficiency above 90% at all conditions. This shows a significant improvement in the performance of the third generation pump over the previous generation pump. Overall size of the pump was also reduced compared to the previous generation designs, further advancing the VDLP towards commercialization.

3. Rolling Diaphragm Seals

As mentioned in section 1.1.3, linkage pumps have an advantage over other pump architectures in their ability to pump a slurry, as the pumping fluid can be separated from the lubricating fluid. However, conventional reciprocating dynamic seals like elastomeric and clearance seals have wear and leakage issues when pumping fluids with suspended particles of similar dimensions to the clearances. Further, mechanical seals[3] and packed glands, the most popular choice of primary sealing in industrial slurry pumps, result in high leakage and high initial cost respectively.

Rolling diaphragm seals (RDS) offer negligible friction, zero effective leakage and do not need any lubrication. However, modern RDS are used at low pressures and there is a lack of literature on the behavior of RDS under various loading conditions since their invention in the 1970's. In this chapter, a study is presented on the viability of rolling diaphragm seals (RDS) for pumping fluids at higher pressures.

The design of a conventional RDS and a literature review of the work done on elastomeric rolling diaphragm seals and fiber reinforced elastomers is presented in section one of this chapter. The approach to setting up the finite element analysis simulation and the post processing approach is discussed in section two. Section three describes how parameters

[3] Elastomer vs mechanical seals: Author refers to simple O-ring/V/U-Cup seal or pack of them used in succession when the term "elastomeric seals" is mentioned. However, mechanical seals refers to a device where elastomeric seal is just one part of device controlling leakage at one or two leakage paths

like fiber diameter, number of fibers, fiber packing, and various fiber-elastomer combinations affect the pressure withstanding capability of RDS. The final section presents concluding remarks on the viability of modifying the design of RDS to improve their pressure withstanding capability.

3.1 Introduction

Rolling diaphragms are flexible seals [26] that provide minimum hysteresis, long stroke and lasts millions of cycles under normal operating conditions [27]. Figure 3.1 shows how a rolling diaphragm seal is setup in a piston cylinder assembly. The outer flange of the RDS is fastened to the cylinder, whereas the center portion of the RDS is fastened to the piston. They offer negligible friction because the seal between the cylinder and piston is maintained by a rolling action rather than a sliding one. This smooth rolling motion between the piston and cylinder results in minimal wear and ensures that there is no stick-slip effect during low speed operations.

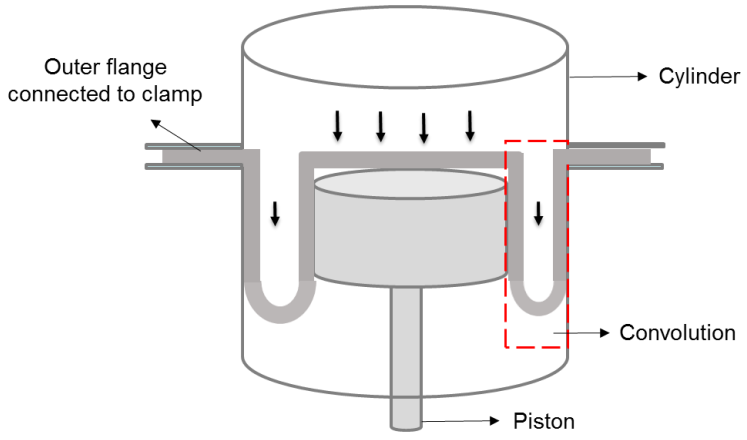

Figure 3.1 Rolling Diaphragm Seal

The diaphragm material is a layer of woven fabric, impregnated with a thin layer of elastomer. Total thickness is usually between 0.38 to 1.32 mm. The fabric, which lends

high tensile strength to the diaphragm, is designed to permit free circumferential elongation, allowing the RDS to conform to the larger diameter of the cylinder or the smaller diameter of the piston without wrinkling. The life of the rolling diaphragm depends on the operating pressures, amount of axial and circumferential stress applied during the stroke, and the materials that form it. In general, a properly installed RDS will provide a life of millions of cycles [27].

From Figure 3.1, it can be seen that most of the pressure load is supported by the piston head, while only a small amount of the fluid pressure is supported by the narrow convolution of the rolling diaphragm. From the cross-sectional view of the convolution in Figure 3.2, it can be observed that the lines of unit pressure along the piston and cylinder sidewalls act in the horizontal plan to force the diaphragm against the sidewalls. The lines of pressure acting on semi-circular segment of the convolution act in a direction normal to the semi-circular segment[4]; hence, all of the pressure lines can be replaced by their horizontal and vertical components. The direction of application of the force and the other boundary conditions while carrying out the finite element analysis on RDS will be discussed in more detail in section 3.2.

[4] The diameter of the semi-circular segment is called as convolution width.

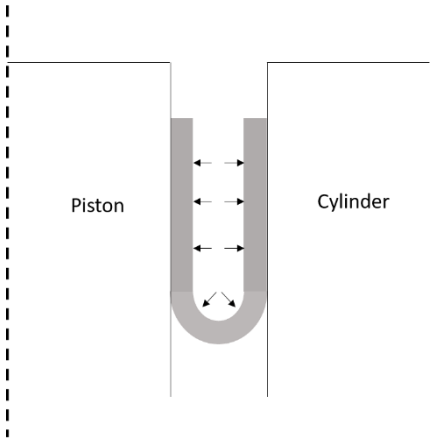

Figure 3.2 Fluid pressure acting in convolution region of RDS

While rolling diaphragm seals have many benefits, there are also some limitations:

(i) Currently, rolling diaphragm seals manufactured by the leading companies are able to withstand pressures ranging just from 4-60 bar [27, 28], while the commonly used industrial pumps usually operate around 200bar

(ii) They need longer installation time than other seal types

(iii) Burrs and sharp edges that may come in contact with the diaphragm can cut and tear both the fabric and elastomer, resulting in premature failure

(iv) Over clamping can rupture the elastomer

(v) Premature failure occurs when the sidewall of the diaphragm comes in contact with itself. One can overcome the limitations (iii) to (v) by following proper guidelines [27, 28].

3.1.1 Literature Review

Significant research on RDS was performed in the 1960's by Rietdijk, van Beukering, van der Aa, and Meijer of Philips Research Laboratories to improve the cycle life of rolling diaphragm seals [29] and to investigate the parameters that influence their pressure withstanding capability. Their research focused on purely elastomeric rolling diaphragm

seals rather than fiber reinforced seals, which is the main focus of the present study. The elastomer diaphragms could not withstand more than 500 kPa of pressure difference, limiting the applications of these diaphragms. They developed a new method, where the diaphragm was supported with a fluid cushion, such that there was only a small pressure differential across the diaphragm, as shown in Figure 3.3, where 'G' and 'O' refer to the pumping fluid and fluid cushion respectively. This increased the pressure capability of diaphragm seals, as the primary pressure difference, which ranged from 5 to 10 MPa, was supported by a conventional seal that separated the fluid cushion under the diaphragm from the space containing the driving mechanism.

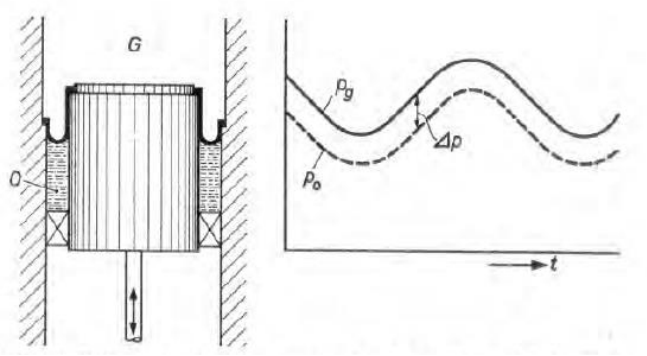

Figure 3.3 Diaphragm seal supported on a fluid cushion which takes up most of the pressure [4]

Through experiments, they found that the endurance of diaphragms depended on the temperature, pressure difference and a factor $\delta = \frac{2d_o}{s}$, where d_o is the thickness of RDS and s is the piston-cylinder clearance. They found that the cycle life of RDS can be improved by increasing the pressure differential and by reducing δ, as shown in Figure 3.4. They also proved this analytically by using the fundamental theory of elasticity to obtain a relationship between the pressure difference, constant δ, and strain induced in the diaphragm seals.

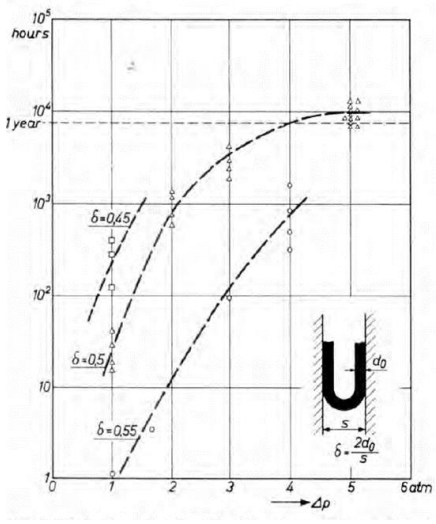

Figure 3.4 Life in hours as a function of pressure difference Δp, and ratio δ

One way to improve the pressure capability of RDS is by reinforcing the elastomer with fiber, thereby increasing its strength while keeping the flexibility and sealing properties of the elastomer. Fiber reinforced elastomer (FRE) composites are not a new concept and a lot of work has gone into exploring their mechanics and fabrication techniques [30]. Research has been done into exploring the fracture and impact resistant properties of FRE [31]. Work by DiaCom and Marsh Bellofram [27, 28] demonstrated that RDS can be manufactured to be able to withstand pressures up to 6 MPa by reinforcing them with suitable fibres. However, not much research has gone into looking at various possible designs of the reinforced diaphragm seals for higher pressure hydraulic applications.

3.1.2 Fibres reinforced in axial and circumferential direction

Commercially available diaphragm seals have uniform fabric weave impregnated with a thin layer of elastomer as shown in Figure 3.5. The fabric is designed to permit free circumferential elongation (allowing free rolling action) while preventing axial distortion.

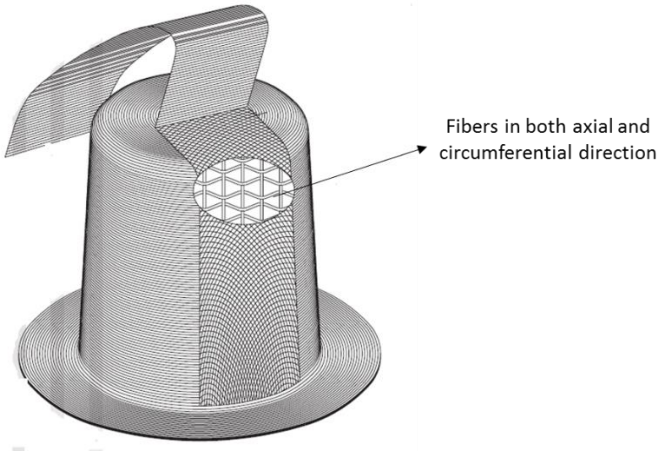

Figure 3.5 Fibers in radial and circumferential direction. Source: Marsh Bellofram [27]

Fluid pressure applied to the fiber reinforced rolling diaphragm is distributed from elastomer onto the axial fibers. As circumferential fibers do not have a significant role in withstanding the load, parameters that could improve the strength of RDS in axial direction are the focus of this investigation into higher pressure operation.

In this chapter, parametric Finite Element Analysis (FEA) studies are employed to explore various possible design options for improving the pressure capability of RDS. The method of setting up the simulation and the post processing approach are discussed in section 3.2. Section 3.3 describes the results of parametric FEA studies on various design variables, while section 3.4 provides concluding remarks and future work on RDS.

3.2 Finite Element Analysis

For the present case study, instead of modelling the entire RDS, only the convolution part of it was modelled and analyzed because of two reasons. First, the convolution is the highest stress section of RDS and represents the location of possible blowout failure. Blowout failure occurs when the elastomer between consecutive fibers ruptures because of the high fluid pressure, ultimately leading to the failure of RDS. Secondly, it reduces the computational time significantly, speeding up the parametric FE analysis.

This section describes the procedure for setting up the FEA problem. Specifically, individual models of the fiber and elastomer, setting up the contact between them, materials selection, and selection of loading and boundary conditions will be discussed. The deformation and stress patterns observed in both the fiber and elastomer will then be discussed. The FEA procedure presented in this section forms the basis for all the parametric analyses carried out on RDS, the results of which are shown in section 3.3.

3.2.1 Pre-processing

3.2.1.1 Geometry Setup

Figure 3.6(a) shows the convolution portion of the RDS with the full 3D model of the convolution presented in Figure 3.6(b). Applying cyclic symmetry conditions on a single sector of the convolution, as shown in Figure 3.6(c), is equivalent to analyzing the entire convolution. Hence, only the representative element shown in Figure 3.6(c) was modeled to reduce the computational time. It should be noted that both the faces chosen as the boundary fields must be of same shape and size, otherwise ANSYS will not be able to map

nodes from the low boundary to the high boundary. Thus, a smaller representative model with one of the symmetry planes down the center of the fiber is not used for the analysis.

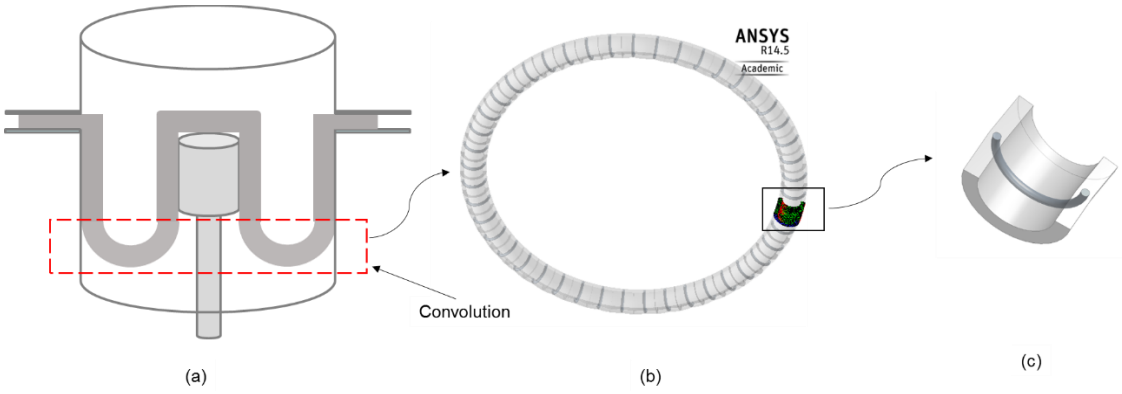

Figure 3.6 (a) Convolution portion of RDS (b) Full 3D model of convolution (c) Single sector 3D model used for analysis

3.2.1.2 Mesh, Contacts, Loading and Boundary Conditions

Figure 3.7 shows how the boundary and loading conditions are applied to each sector. Fluid pressure is applied on just the convolution part of the RDS, while the top flat surface is fully fixed. Technically, one should apply pre-strain in the material at the outer radius of the diaphragm due to expanding to conform to the cylinder wall. However, because of the lack of such convenient feature in the software to do that, all the simulations were run by assuming that the material is not in any kind of pre-strain. A local cylindrical coordinate system is defined at the center of the fiber in the convolution region as shown in Figure 3.8 with y-axis pointing along the length of the fiber and z axis pointing out of the plane. The global Cartesian coordinate system origin is at the center of the RDS.

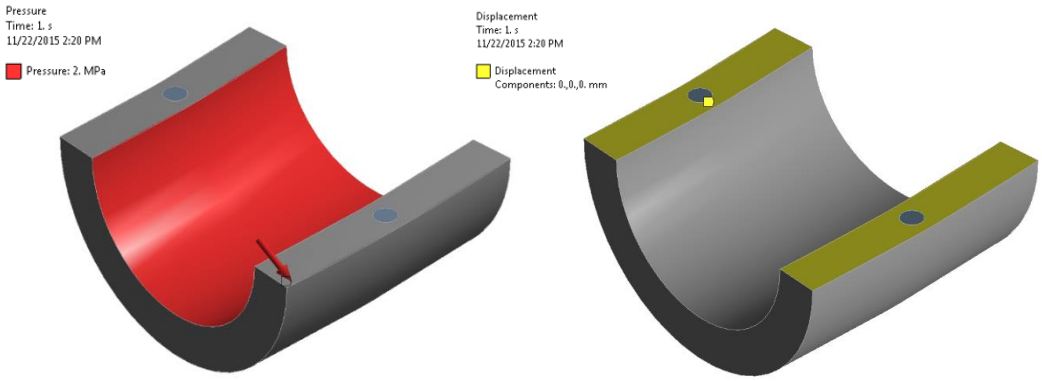

Figure 3.7 (a) Fluid pressure applied on the convolution (b) Boundary Conditions

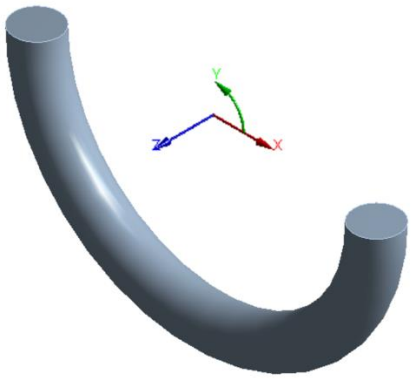

Figure 3.8 Local cylindrical co-ordinate system for fiber

Unlike the fibers, a global coordinate system is used for defining the elastomer properties, as it is considered to be an isotropic material. During proper operation, the RDS must have minimal compliance, and thus the elastomer was not treated as a hyper elastic material.

For the parametric case studies in this chapter, bonded contact is defined at the fiber-elastomer interface. The linear bonded contact not only reduces computational time, it also well represents the present case where the fibers remain bonded to the elastomer unless failure occurs.

To determine proper node spacing, a mesh resolution study was conducted. As the geometry is sweepable, mesh was generated using higher order 3-D 20-node Solid186 elements. Nodal and element count, maximum stress and deformation values, continuity of stress and deformation contours, and the simulation time were the factors that were taken into account to identify the mesh to use during analysis.

Table 3.1 shows the results of the study, with I to V representing different cases of mesh size for the fiber and elastomer. It can be observed that the stress and deformation values are converged by case III. Also, by comparing the averaged and non-averaged contour plots, it was observed that the stress and deformation contour plots started to become continuous from case III. Considering the simulation time and level of accuracy, mesh generated in case III with a node count of 85,195 was used for all the simulations discussed from here on in this chapter.

Table 3.1 Mesh refinement study for analyzing RDS

	I	II	III	IV	V
Node count	5772	17970	85195	142120	217362
Element count	1013	3350	18172	30914	47991
Max stress (MPa)	99.36	115.69	221	210.27	215.24
deformation(mm)	0.301	0.300	0.299	0.299	0.299
Stress contour	Discontinuous	Discontinuous	Continuous	Continuous	Continuous

Deformation contour	Discontinuous	Continuous	Continuous	Continuous	Continuous
Simulation time (min)	0.1	0.2	0.9	1.5	2.6

3.2.1.3 Large Deformation vs. Small deformation formulation

During excessive pressure loading, there is a possibility of seeing non-linear large deformation strain, primarily in the elastomer. Theoretically, small deformation strain is described by

$$\varepsilon_{ij} = \frac{1}{2}\left(\frac{\partial u_i}{\partial x_j} + \frac{\partial u_j}{\partial x_i}\right), \quad (1)$$

Where ∂u_i represents displacement in the *i* direction and ∂x_j represents original length in the *j* direction. Upon expanding it, we get the following strain matrix:

$$\begin{matrix}\varepsilon_{11} & \varepsilon_{12} & \varepsilon_{13} \\ \varepsilon_{21} & \varepsilon_{22} & \varepsilon_{23} \\ \varepsilon_{31} & \varepsilon_{32} & \varepsilon_{33}\end{matrix} = \begin{bmatrix} \frac{\partial u_1}{\partial x_1} & \frac{1}{2}\left(\frac{\partial u_1}{\partial x_2} + \frac{\partial u_2}{\partial x_1}\right) & \frac{1}{2}\left(\frac{\partial u_1}{\partial x_3} + \frac{\partial u_3}{\partial x_1}\right) \\ \frac{1}{2}\left(\frac{\partial u_2}{\partial x_1} + \frac{\partial u_1}{\partial x_2}\right) & \frac{\partial u_2}{\partial x_2} & \frac{1}{2}\left(\frac{\partial u_2}{\partial x_3} + \frac{\partial u_3}{\partial x_2}\right) \\ \frac{1}{2}\left(\frac{\partial u_3}{\partial x_1} + \frac{\partial u_1}{\partial x_3}\right) & \frac{1}{2}\left(\frac{\partial u_3}{\partial x_2} + \frac{\partial u_2}{\partial x_3}\right) & \frac{\partial u_3}{\partial x_3} \end{bmatrix}$$

Similarly large deformation strain is described by Lagrangian strains [47] as follows:

$$E_{ij} = \frac{1}{2}\left(\frac{\partial u_i}{\partial x'_j} + \frac{\partial u_j}{\partial x'_i} + \frac{\partial u_k}{\partial x'_i}\frac{\partial u_k}{\partial x'_j}\right), \quad (2)$$

Where vectors x' and x represent a point in 3D space corresponding to the undeformed/initial and deformed configurations respectively, as shown in Figure 3.9, where u represents the displacement between the two points.

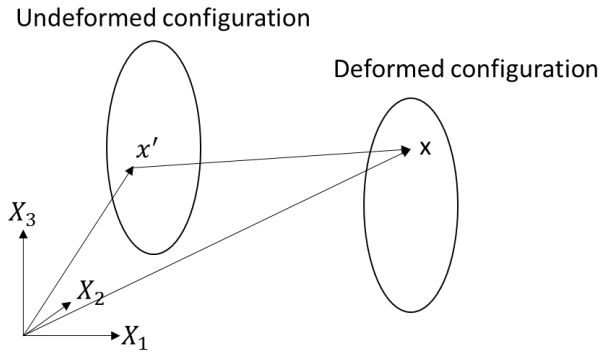

Figure 3.9 Relationship between a point in reference/initial/undeformed and deformed configuration

The large deformation formulation gives more accurate results as it involves higher order terms in the strain definition. However, this comes at a price of longer simulation times. Table 1 compares the results obtained by using both small deformation and large deformation formulations for the case of 0.3mm diameter nylon fiber reinforced silicone RDS with 120 axial/radial fibers, when the applied pressure is 2MPa (Table shows the volume averaged stress and deformation values in the fibers. Detailed post processing of the results will be discussed later in section 3.2.3.

Table 3.2 Accuracy vs. Simulation time with small and large deformation formulations

	Small Deformation Formulation	Large Deformation Formulation
Stress (MPa)	36.329	39.226

Deformation (mm)	0.11735	0.11627
Simulation time (minutes)	15	330

It can be seen from Table 3.2 that large deformation formulation predicts the stress induced in the fiber to be 7.4% more than what small deformation formulation calculates. Similarly a difference of 0.93%can be seen in the deformation result. However, in order to obtain these results, large deformation formulation took 22 times more simulation time than what is needed for small deformation. Further, during proper operation, the RDS must have minimal compliance, and large strain represents a failure due to excessive compliance of the seal. Because of this, the small deformation formulation was applied in all of the parametric studies.

3.2.2 Post-processing

Section 3.2.1 discussed the procedure for setting up the FEA problem. The purpose of this section is to present the post-processing. Results presented in this section are for a baseline case, the parameters of which are presented in Table 3.3.

Table 3.3 Parameters for the baseline RDS analysis case

Parameter	Value
Thickness of RDS	0.635mm
Convolution radius	1.587mm
Piston radius	24.6mm
Fluid Pressure	2MPa
Number of Fibers	45

Figure 3.10 shows the total deformation of a sector of the RDS and that of the fiber. The maximum deformation is in the elastomer region between two consecutive fibers as shown in Figure 3.10(a). The elastomer does not undergo much deformation around the fiber, as the fiber supports the load. Further, maximum deformation in the fiber (and therefore the maximum strain) is a skewed towards the outer radius of the convolution, as shown in Figure 3.11. This is because of the increase in circumferential area towards the outer part of the convolution compared to its inner region.

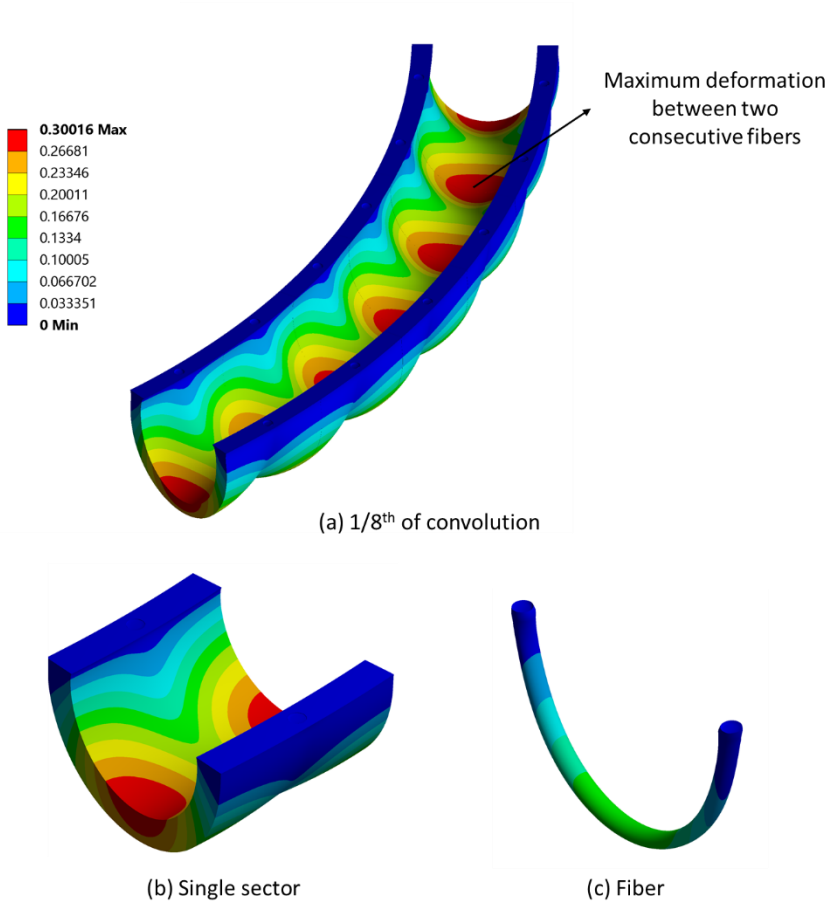

Figure 3.10 Total deformation of (a) 1/8th of convolution (b) Single sector and (c) fiber of RDS (Note: deformation is 4X)

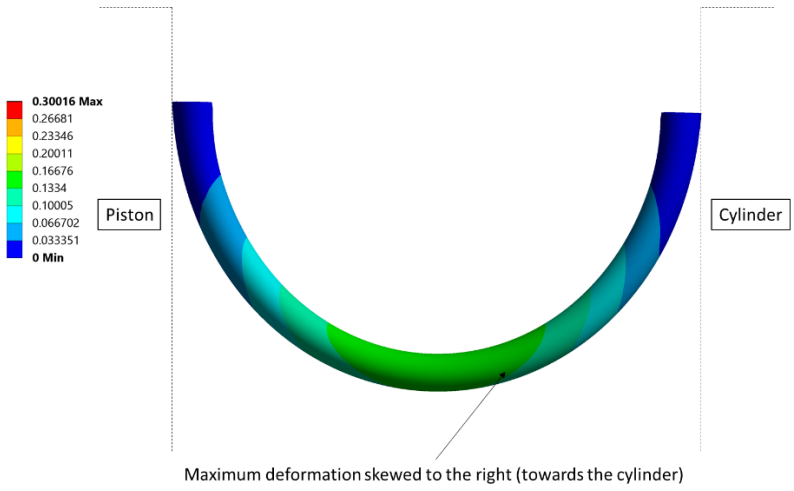

Figure 3.11 Maximum deformation in the fiber

Figure 3.12 and Figure 3.13 shows the VonMises stress induced in the elastomer and fiber of the RDS. Because of the fixed displacement constraints and bonded contact, it is normal to expect high fictitious stresses at the fiber and elastomer ends. Ignoring such high local stresses due to the boundary conditions, it can be observed that the maximum stress in the fiber and elastomer is near the center of the convolution on the outer radius, where the strain is greater.

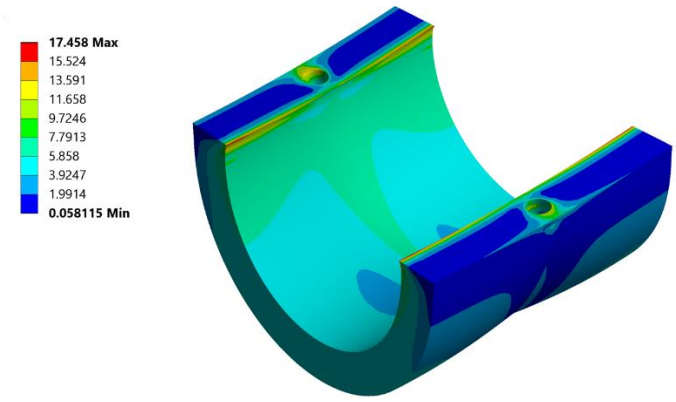

Figure 3.12 VonMises stress in elastomer region of RDS

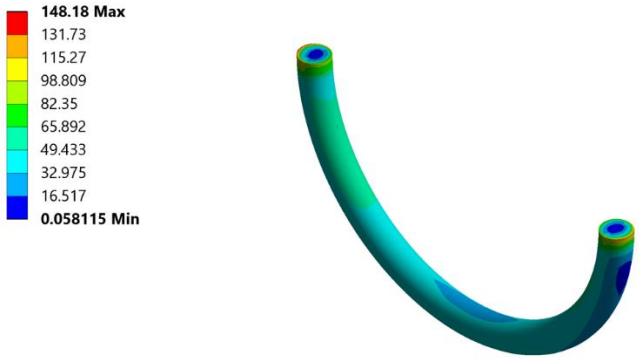

Figure 3.13 VonMises stress in the fiber of RDS

Based on the approach presented in this section, the post-processing results can be compared as follows:

I. The maximum deformation in the fiber and elastomer can be used as one of the metrics to judge the pressure capability of RDS. Less deformation in the elastomer corresponds to the case where RDS can withstand more pressure.

II. The stress induced in the fiber and elastomer near the center of the convolution on the outer radius can be used as another measure to compare one RDS behavior with that of the other during FE analysis. Reduced stress in the fiber corresponds to the case where the RDS can withstand more pressure

III. Instead of using the deformation or stress value at a particular node in the fiber or elastomer to compare different cases, it is better to use an averaged nodal deformation and stress result that represents the RDS behavior as a whole, independent of the node/element selected in the high stress/deformation region. A method of deriving averaged results using APDL code is presented in section 3.3.1.3

3.3 Parametric Study

The primary factors of interest that directly affect the pressure withstanding capability of RDS are: the number of fibers, fiber diameter, fiber pattern, and young's modulus of the elastomer. Parametric studies were carried out using FEA to understand the importance of each parameter and how they can effect RDS behavior, results of which are discussed in section 3.3.1 to 3.3.4. Meshing methods, contacts applied between surfaces, loading and boundary regions remain the same as presented in section 3.2 for all the different analyses explained from here on, in this chapter.

3.3.1 Fiber Diameter and Number of Fibers

A parametric study was carried out with 45, 60, 90, 120, and 180 axial/radial fibers and with various fiber diameters of 0.1mm, 0.3mm, 0.5mm. It should be noted that the number of fibers and the fiber diameter could be increased beyond 180 and 0.5mm respectively when manufacturing RDS. These numbers are chosen arbitrarily so that the fiber diameter would be able to fit inside a RDS of thickness 0.635mm, while modeling each sector of the RDS. Varying the number of fibers is equivalent to changing the angle of each sector, which is then revolved 360^0 about the center of the RDS to get the full convolution geometry.

In this case study, unfilled nylon and silicone were considered to be the fiber and elastomer materials respectively. A separate parametric study was conducted to understand the effect of using various other fibers and elastomers on the behavior of RDS, which is discussed

later in this chapter. Following table shows the properties of unfilled nylon fiber and silicone.

Table 3.4 Properties of unfilled nylon and silicone [12, 37]

	Unfilled Nylon Fiber	Silicone
Modulus	E_x=117.2MPa E_y=117.2MPa E_z=117.2MPa G_{xy}=397MPa G_{yz}=397MPa G_{xz}=19.85MPa	$E = 50$MPa
Poison's ratio	ϑ_{xy}=0.25 ϑ_{yz} =0.25 ϑ_{xz}=0.25	$\vartheta = 0.48$

The parametric study was done in two stages. In the first stage, the number of fibers was kept constant and fiber diameter was varied. In the second stage, the fiber diameter was kept constant and the number of fibers was changed.

3.3.1.1 Varying fiber diameter by keeping a constant number of fibers

Figure 3.14 shows how the deformation of the fibers vary as the fiber diameter is decreased from 0.5mm to 0.3mm to 0.1mm, while keeping the number of fibers fixed at 120. The applied pressure is 2MPa and the loading and boundary regions are same as mentioned in section 3.2. The figure shows that the maximum deformation in the convolution near the

center of the fiber increases as the fiber diameter decreases, which is intuitive because, as the fiber diameter decreases, more of the load acting on the seal is taken up by the elastomer. For the sake of clarity and convenience, just $1/8^{th}$ of whole convolution region is showed in the figure.

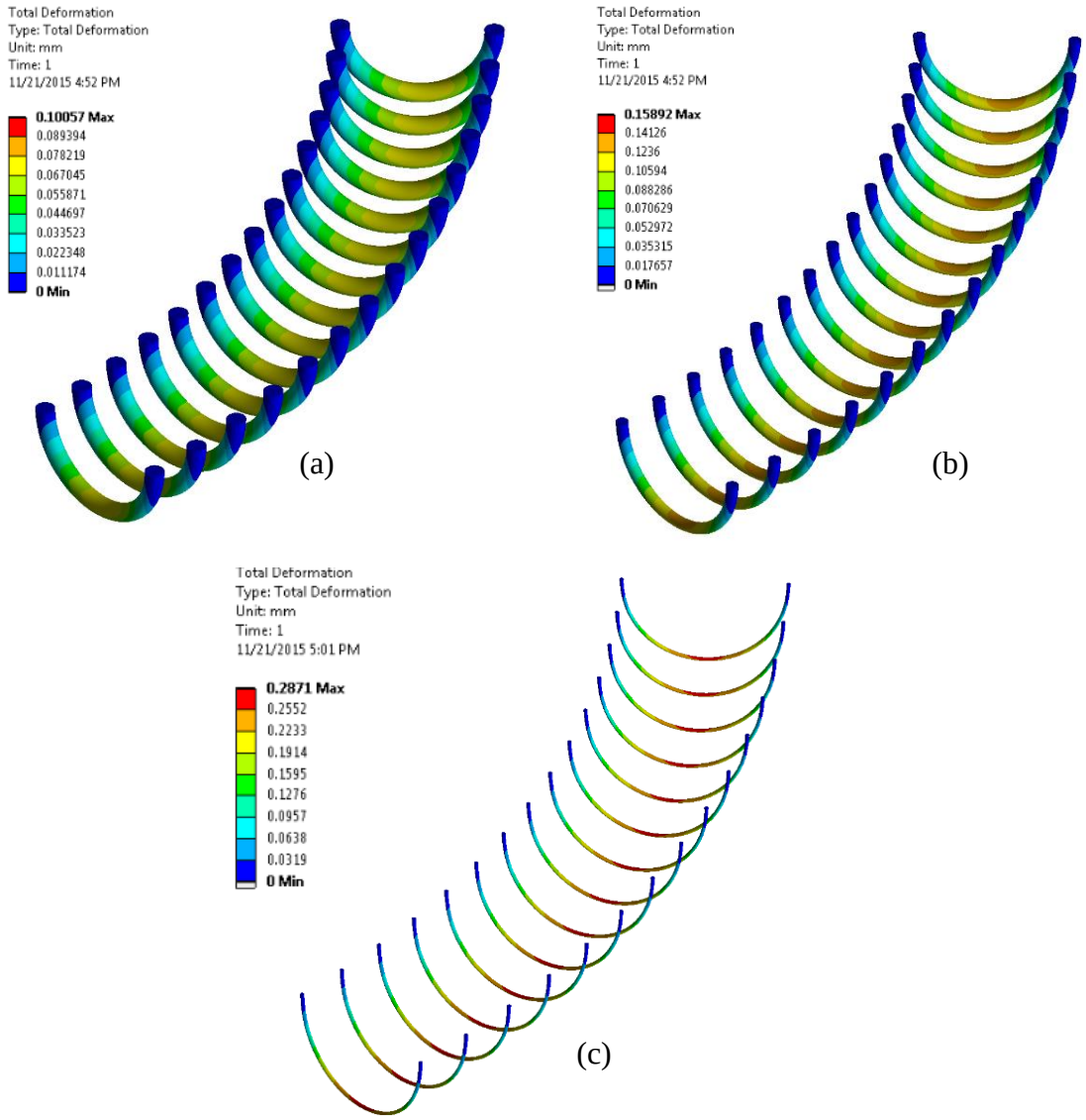

Figure 3.14 Deformation in the fibers (1/8th of full convolution) of diameters (a) 0.5mm (b) 0.3mm (c) 0.1mm

Figure 3.15 shows the variation in the Von Mises stress induced in the fibers as the fiber diameter is decreased. Maximum total equivalent stress experienced by the convolution increases as the fiber diameter decreases from 0.5mm to 0.1mm. This can be expected

because, as the fiber diameter decreases, the ability to withstand the load exerted on the RDS decreases, thereby resulting in more induced stress in the fiber.

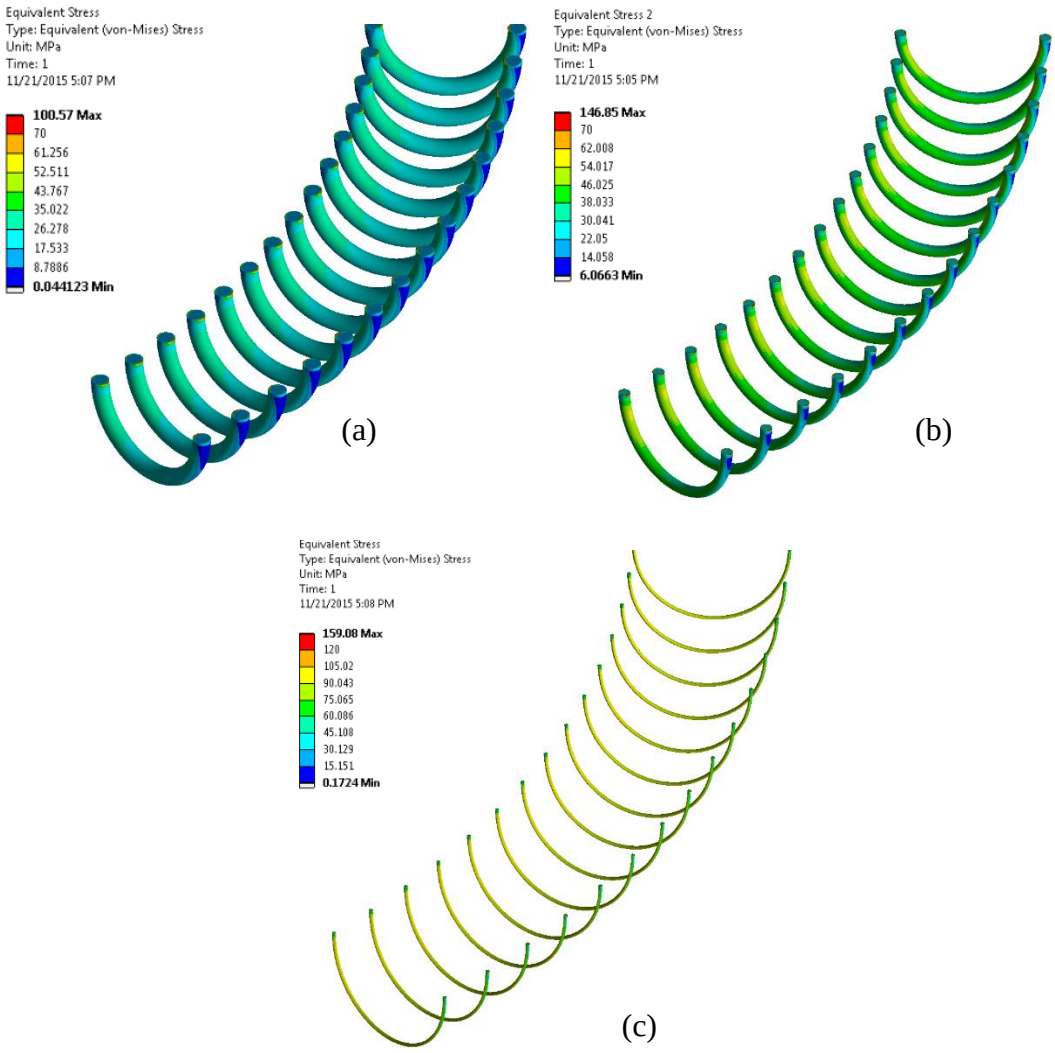

Figure 3.15 VonMises stress induced in the fibers of diameters (a) 0.5mm (b) 0.3mm (c) 0.1mm

The yield strength of nylon is between 51 – 64 MPa depending on the constituents added to it to improve some of its properties. Figure 3.15 shows that the stress induced in the fibers of diameter 0.1mm far exceeds the yield strength and thereby would result in the

failure of RDS even at such a low pressure of 2MPa. Thus, it is observed that the larger the fiber diameter, the better is the load withstanding capability.

3.3.1.2 Varying number of fibers by keeping fiber diameter as a constant

Figure 3.16 shows the variation of deformation in the fibers as the number of fibers are increased from 45 through 90 to 180, keeping fiber diameter as a constant at 0.5mm and applying a pressure of 2MPa. It can be seen from Figure 3.16 that as the number of fibers increase, the deformation in the fibers decrease. This resulting deformation pattern is expected because, as the number of fibers increase, the fiber volume fraction in the seal increases. As the fibers have a greater strength compared to the elastomer, increasing the fiber volume fraction automatically reduces the amount of load taken by the elastomer thereby reducing the deformation of the RDS.

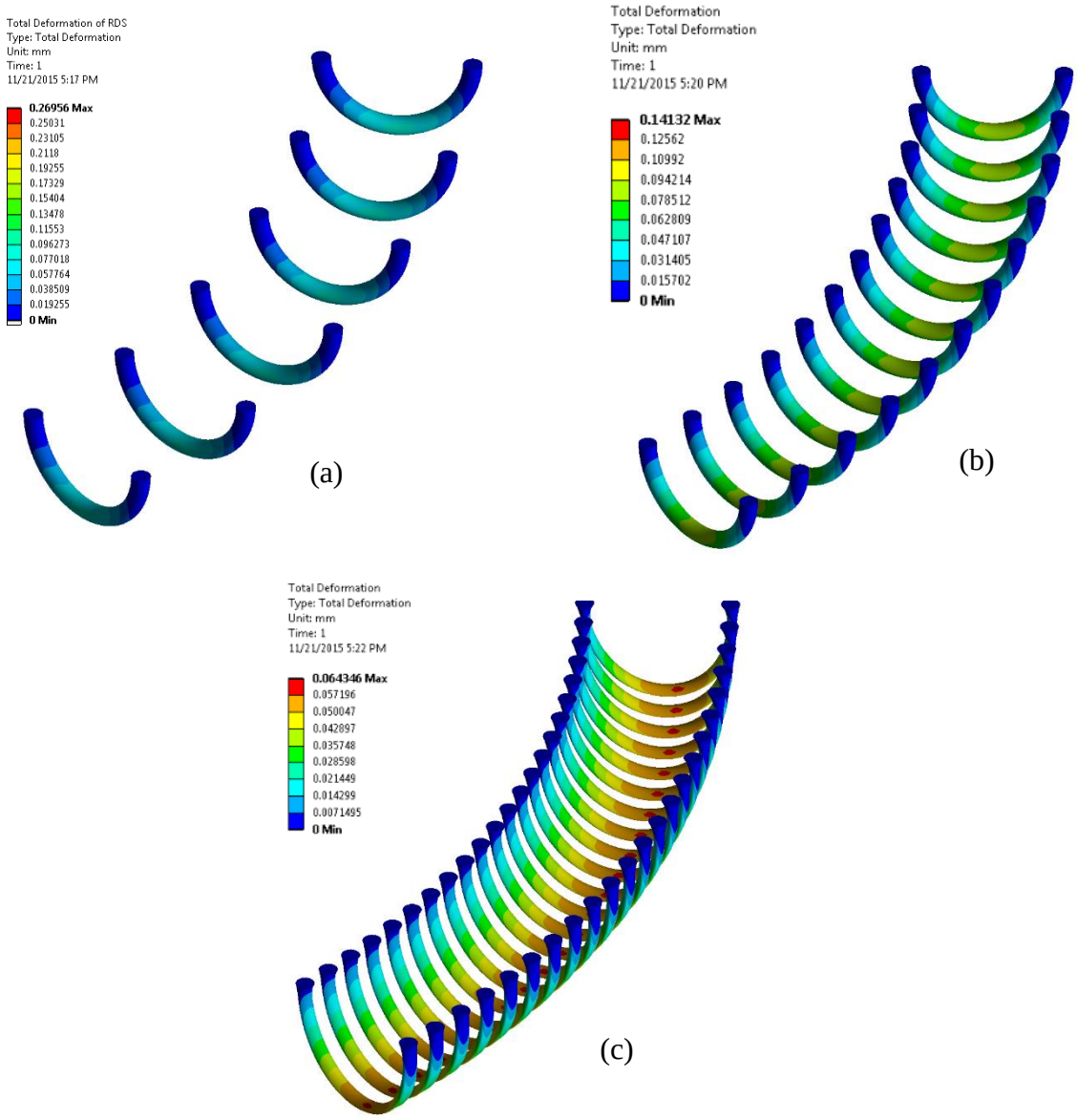

Figure 3.16 Deformation in the fibers, with number of fibers in convolution being (a) 45 (b) 90 (c) 180

Figure 3.17 shows the variation of VonMises stress in the fibers with increase in number of fibers keeping fiber diameter as a constant at 0.5mm. Even though it is pretty unclear when comparing the range of values of stress distribution across various cases in the figure, it can be observed that as the number of fibers increase, the stress induced in the fibers decrease. In order to ease the process of comparing the performance of one RDS with that

of the other, volume averaged VonMises stress and deformation are calculated and then used as a base for comparison, which is explained in section 3.3.1.3.

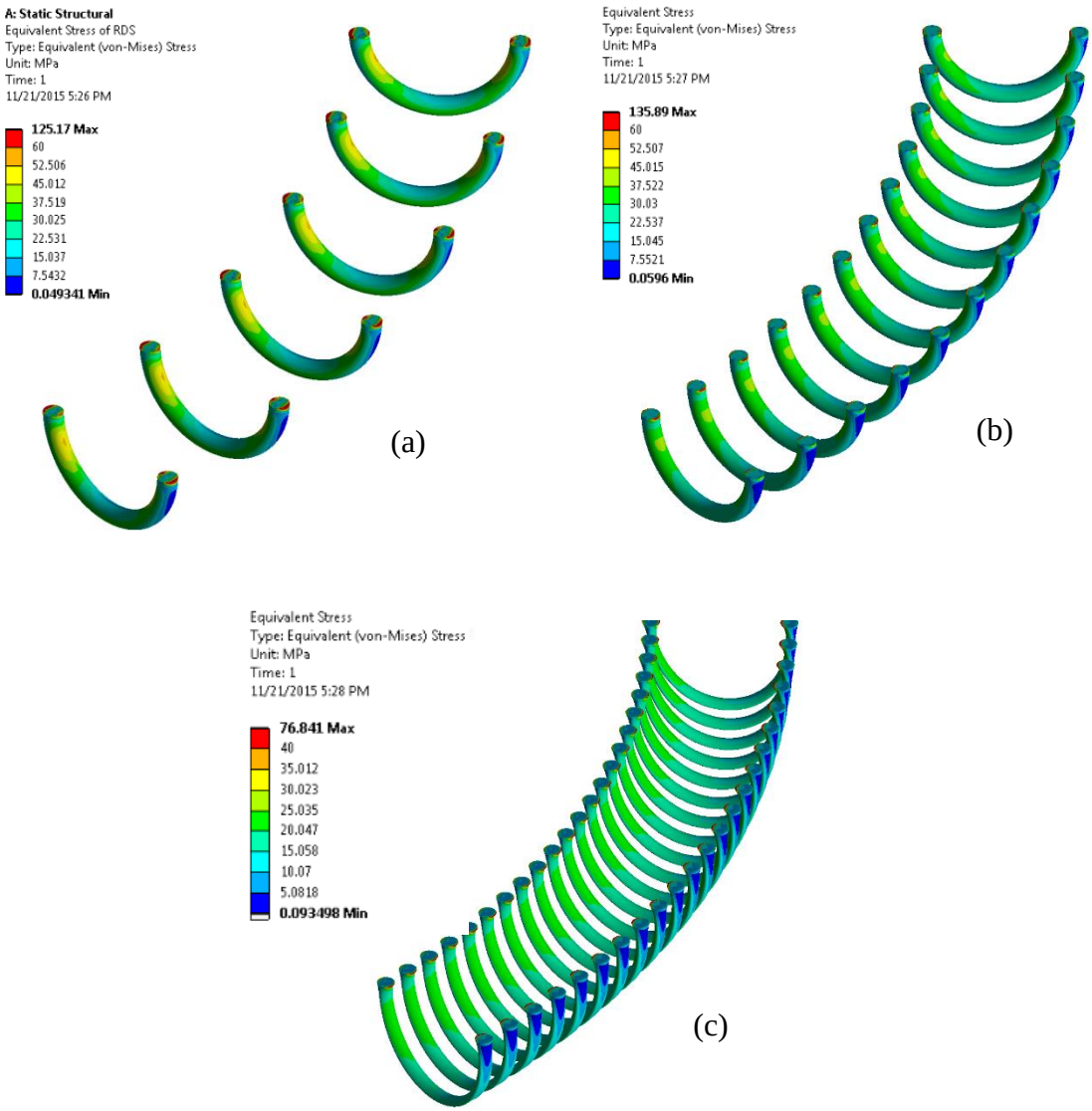

Figure 3.17 Stress in the fibers, with number of fibers in convolution being (a) 45 (b) 90 (c) 180

Figure 3.18 has been provided in order to show the variation in the deformation of elastomer in RDS as the number of fibers are increased from 45 to 180. It should be noted that the deformation shown in the figure is scaled to 6 times the true deformation. It can be

observed that the elastomer bulges out between the fibers in all the cases, as explained in the section 3.2. This bulging between the fibers is gradually reduced as the number of fibers increase, because most of the load is taken by the fibers, thereby reducing the deformation of the elastomer as well as the stress induced in it. The bulging effect between the fibers is undesired as it leads to increased compliance and thereby reduces the volumetric displacement of the pump.

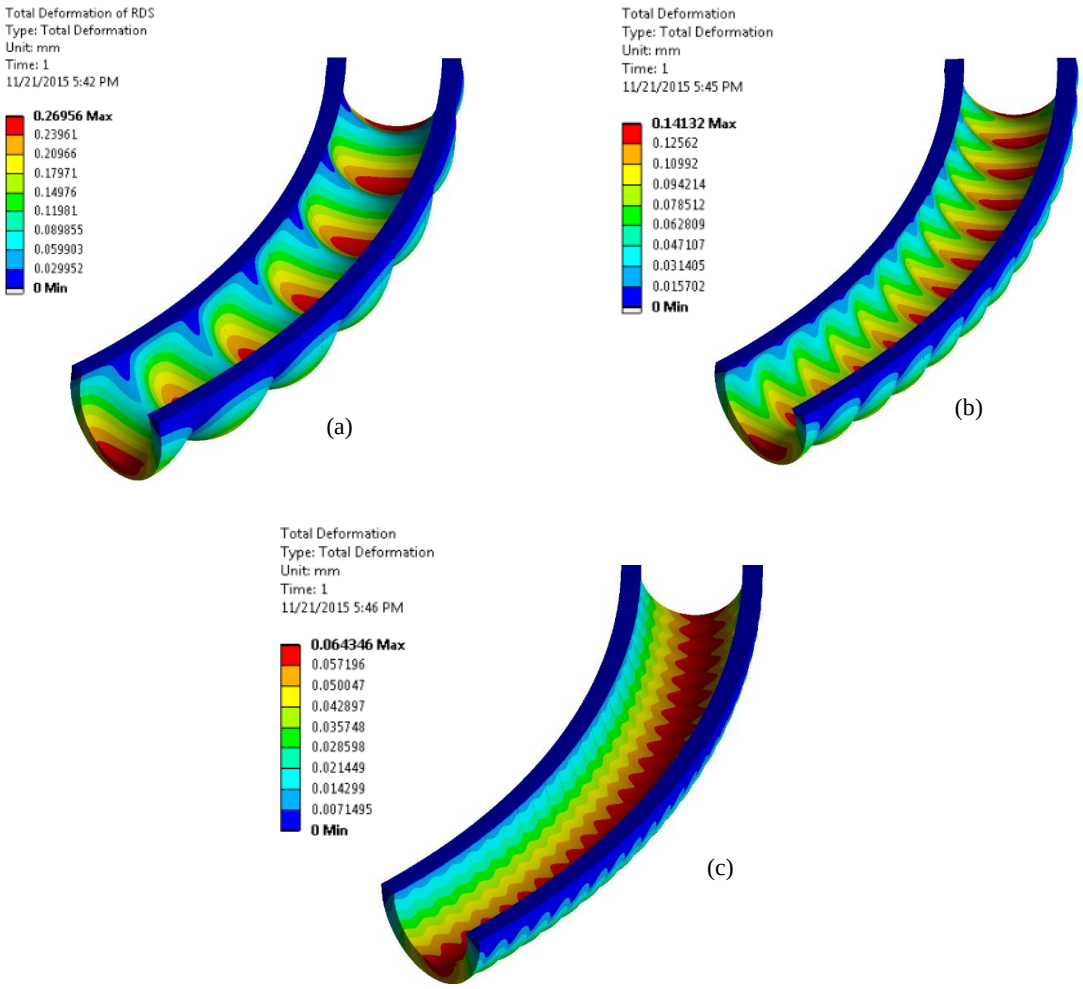

Figure 3.18 Deformation in the elastomer, with number of fibers in convolution being (a) 45 (b) 90 (c) 180

3.3.1.3 Volume Averaged Results

Sections 3.3.1.1 and 3.3.1.2 showed color contour plots of the variation in deformation and stress in the fiber and elastomer as the number of fibers and fiber diameter was changed. It is quite difficult to compare one case with that of the other through such plots. Hence, in order to facilitate a better comparison, an APDL (ANSYS Parametric Design Language) code has been written (Appendix B) to calculate volume averaged VonMises stress and deformation, which can then be used as a base to numerically compare any two cases. The following equations show the corresponding definitions.

$$\sigma_{v,stress} = \frac{\sum(V_i * \sigma_i)}{\sum V_i} \quad (1)$$

$$\delta_{v,deformation} = \frac{\sum(\delta_i)}{N} \quad (2)$$

where

V_i: volume of i^{th} element

σ_i: stress observed in the i^{th} element

δ_i: deformation observed at i^{th} node

N: number of nodes in the selected set

$\sigma_{v,stress}$: volume averaged stress

$\delta_{v,deformation}$: volume averaged deformation

To perform these averaging calculations, a set of elements needs to be chosen. These elements are selected from the fiber and elastomer mesh individually, in the regions where maximum deformation and VonMises stress is expected, so that comparison between different cases could be made using the maximum values observed.

For example, as shown in Figure 3.19(a) and (c), for the purpose of calculating averaged deformation, nodes are selected for the fiber and elastomer in the regions where the maximum deformation is observed. i.e., for the fiber it is near the center of the convolution and for the elastomer it is at the either ends of the sector. Similarly, for the calculation of volume averaged stress, elements are selected from the center of fiber and center of elastomer, as maximum stress is observed in those regions, as shown in Figure 3.19(a) and (b). Once, the solver calculates the elemental stresses and the nodal displacements at the selected elements/nodes, the APDL code then calculates the volume averaged VonMises stress and averaged deformation in both the fiber and the elastomer.

Elemental stress used in calculating volume averaged stress refers to the averaged value of the stress calculated at Gauss Points. Nodal stresses are not used because they are calculated by extrapolating the stress at gauss points to the nodes. Hence, nodal stress results depend on the shape function of corresponding element – some might be better than others. This might result in inducing slight error in the nodal results. Hence, elemental stresses were used in calculating volume averaged stress instead of nodal stresses.

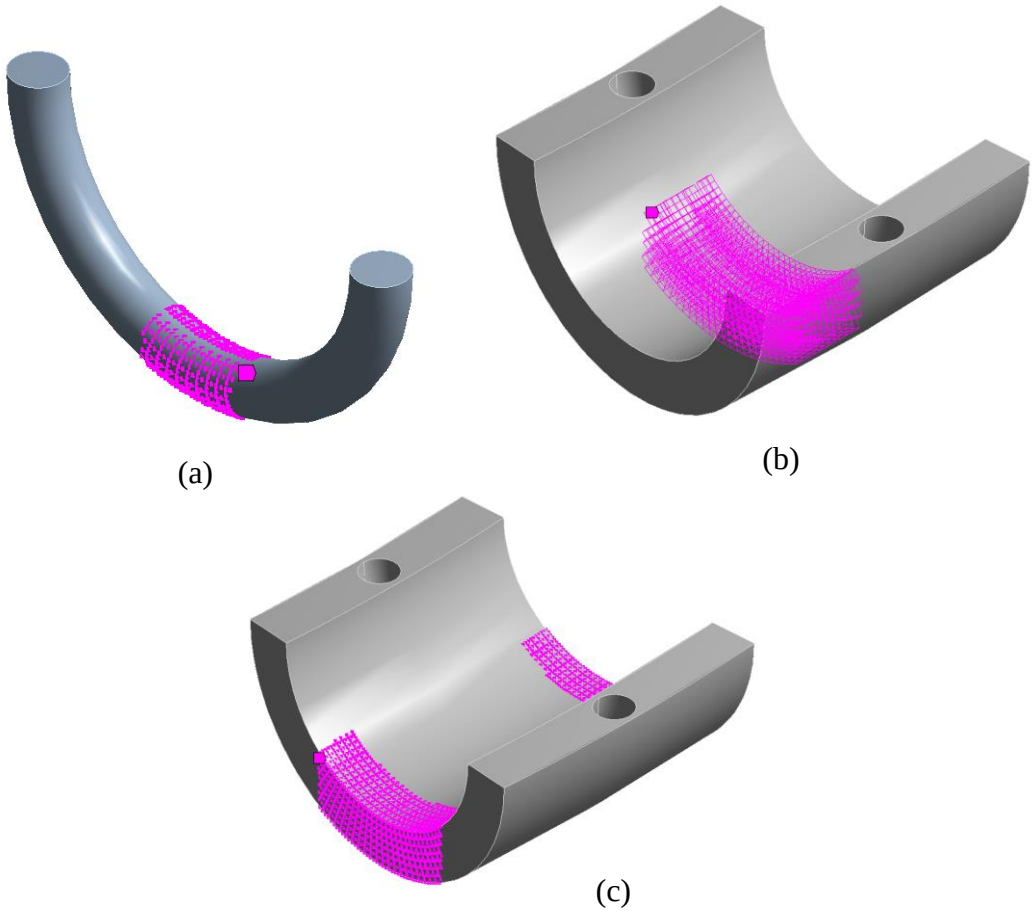

Figure 3.19 (a) nodes/elements selected at the center of convolution for calculating deformation/stress in fiber (b) elements selected in elastomer for calculating von Mises stress (c) Nodes selected in elastomer for calculating the deformation

Figure 3.20 shows the volume averaged VonMises stress in the fiber as both the number of fibers and the fiber diameter is varied. As explained previously in this section, the stress induced in the fibers decreases as the number of fibers increases and also it decreases as the fiber diameter increases. Similar pattern can be observed from Figure 3.20. Figure 3.21 shows the variation of volume averaged stress in the elastomer. It can be observed that similar to the variation seen in the fibers, the stress induced in the elastomer also decreases

as the fiber diameter increases. It can also be observed that the stress induced decreases as the number of fibers increases.

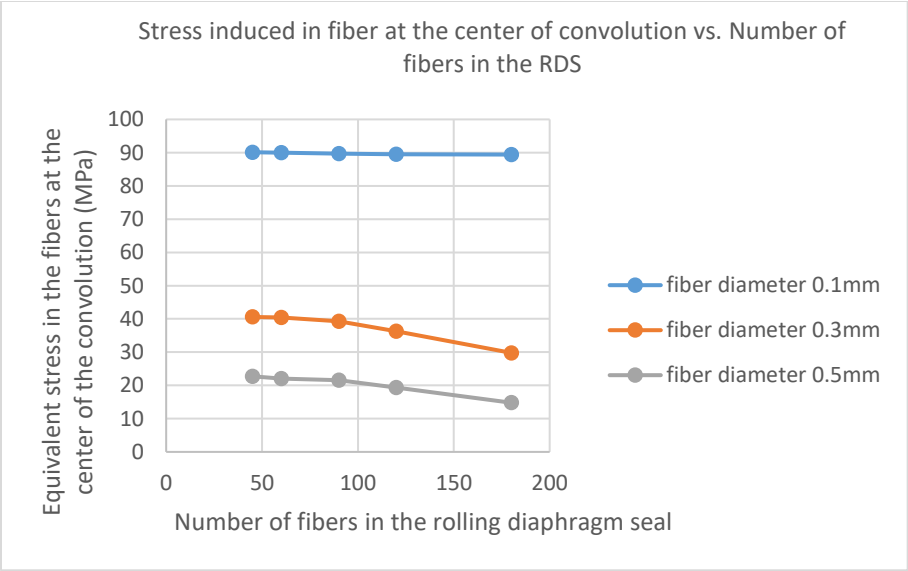

Figure 3.20 Variation of stress induced in the fiber with fiber diameter and number of fibers in RDS

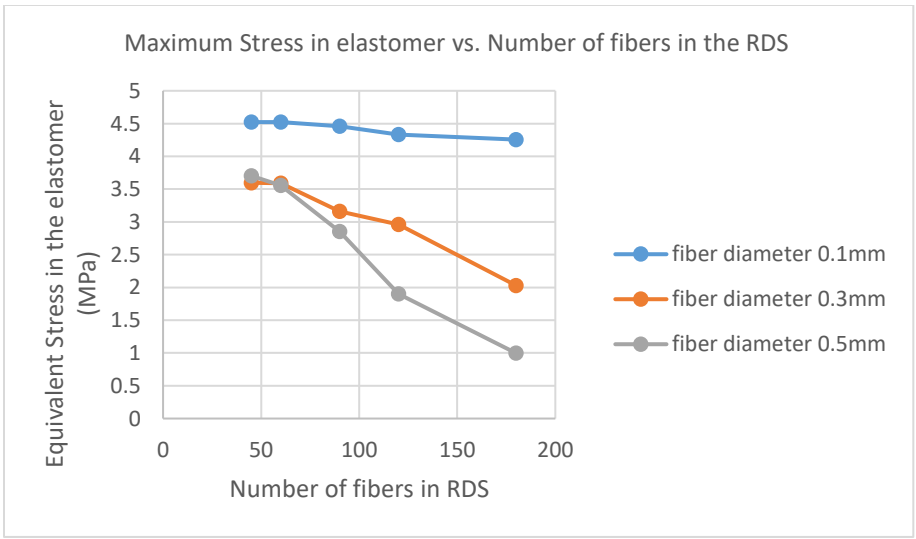

Figure 3.21 Variation of stress induced in the elastomer with fiber diameter and number of fibers in RDS

Figure 3.22 shows that the deformation in the fiber at the center of the convolution decreases as the fiber diameter and number of fibers increases. It should be noted that the

number of fibers and the fiber diameter could be increased beyond 180 and 0.5mm respectively. These numbers are chosen so that the fiber diameter would be able to fit inside a RDS of thickness 0.635mm, while modeling each sector of RDS. The maximum deformation in the elastomer, which usually occurs between any 2 consecutive fibers, also decreases with the fiber diameter and the number of fibers as shown in Figure 3.23.

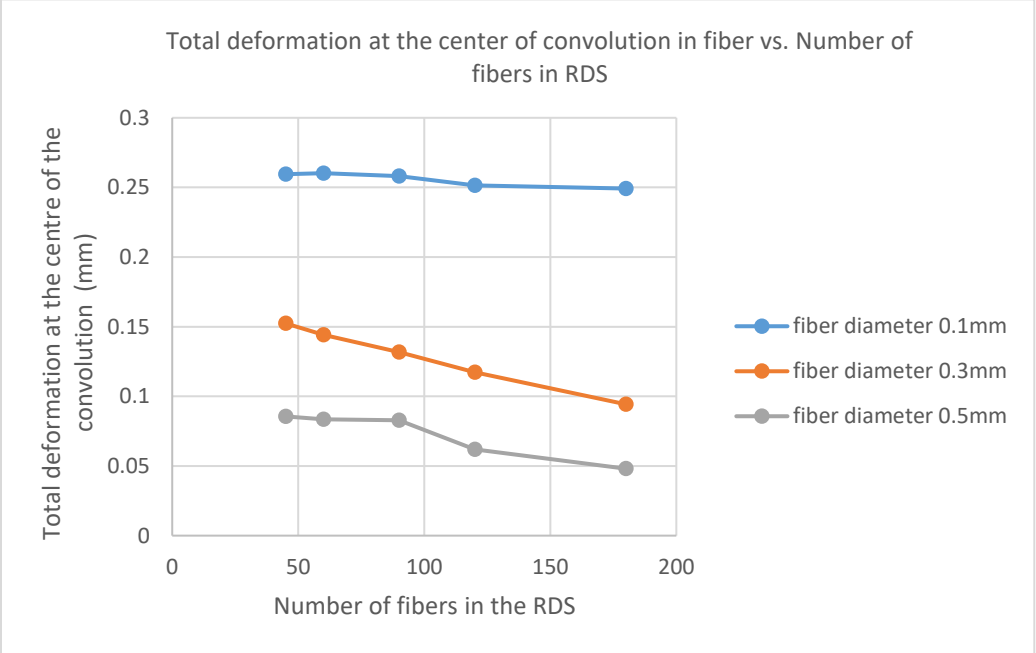

Figure 3.22 Variation of deformation in fiber with fiber diameter and number of fibers in RDS

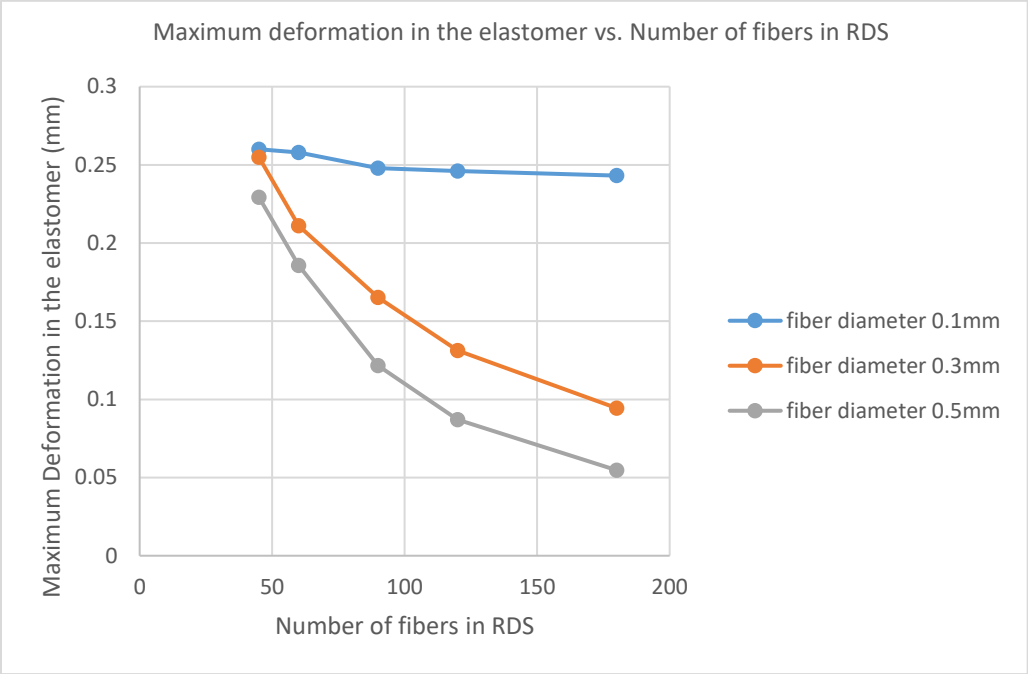

Figure 3.23 Variation of deformation in elastomer with fiber diameter and number of fibers in RDS

From the parametric FEA results, it can be concluded that increasing the fiber diameter and the number of fibers for a given thickness of rolling diaphragm seal reduce the deformation and stress induced in both the fiber and the elastomer, thereby improving the pressure withstanding capability.

3.3.2 Young's Modulus of Elastomer

This section describes the results of another parametric study that has been conducted to understand the behavior of RDS as the young's modulus of elastomer is varied. In this study, modulus of elasticity of elastomer is varied from 50 MPa to 5 MPa .The six different cases considered in the study are shown in Table 2.6.

Table 2.6 Various combinations of inputs used for parametric analysis in ANSYS

E (fiber) (Pa)	E_{matrix} (Ratio =E_{fiber}/ E_{matrix}) (Pa)
1.649E9	5E7 (Ratio=32.98)
	2.5E7 (Ratio=65.96)
	1.25E7 (Ratio=131.92)
	8.34E6 (Ratio=197.721)
	6.25E6 (Ratio=263.84)
	5E6 (Ratio=329.8)

Note that the results in Figure 3.24 to Figure 3.27 are formulated such that R indicates the ratio of modulus of elasticity of fiber to the modulus of elasticity of elastomer. Stress and deformation results are shown as R is increased from 32.98 to 329.8 for all the cases. The variable 'R' indicates how soft/compliant the elastomer is, compared to that of fiber.

Resultant averaged deformation values for the fiber with a change in the young's modulus of elastomer is shown in Figure 3.24. It can be observed that as the modulus of elasticity of elastomer was reduced (indicated by an increase in R in this case as described before), the deformation of fiber increases. This is intuitive because, as the elasticity modulus of elastomer is reduced, it can't handle greater loads and hence the fibers sees an increase in load, resulting in larger deformation in materials with low elastomeric young's modulus

value. We can also observe that the deformation of the fiber doesn't increase much after a given amount of softening of the elastomer.

Figure 3.25 shows the stress induced in the fiber with varying young's modulus of elastomer. Similar to the pattern observed before, the stress induced in the fiber increases as the elastomer's young's modulus decreases. Similar explanation can be given to the deformation pattern and stress induced in the elastomer as shown in Figure 3.26 and Figure 3.27.

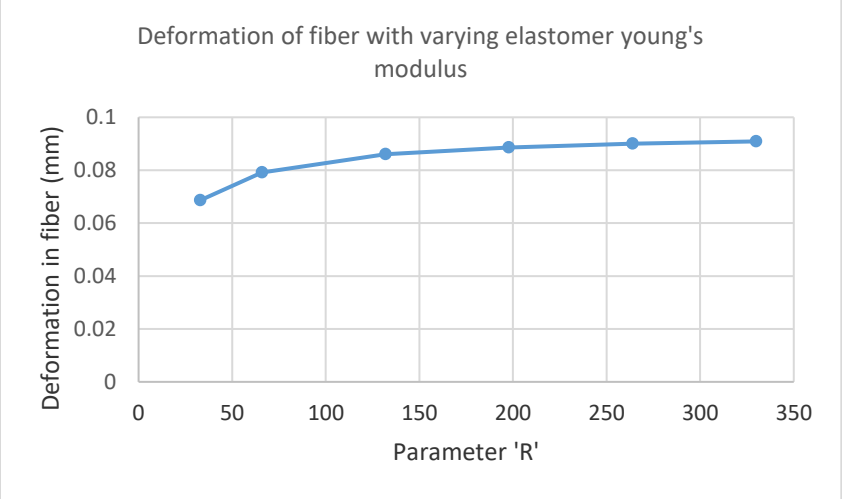

Figure 3.24 Variation of deformation in fiber with young's modulus of elastomer

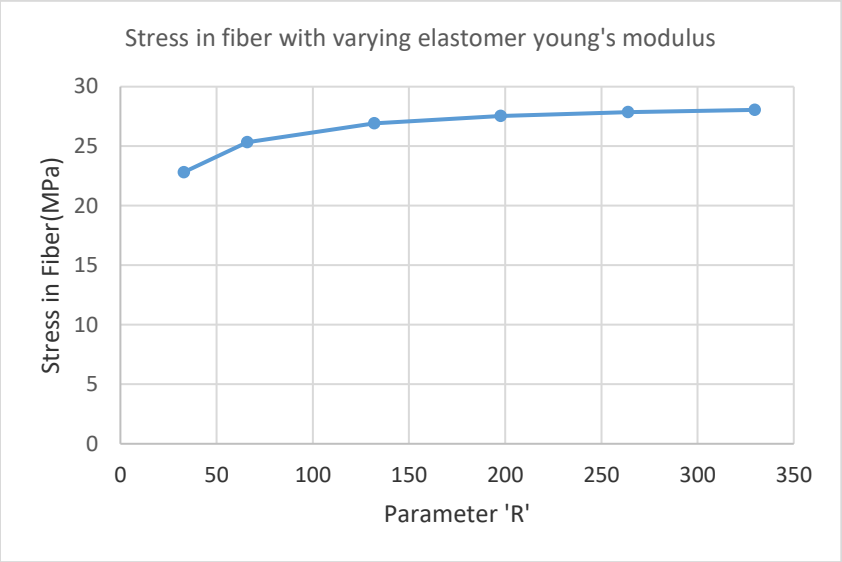

Figure 3.25 Variation of stress in fiber with young's modulus of elastomer

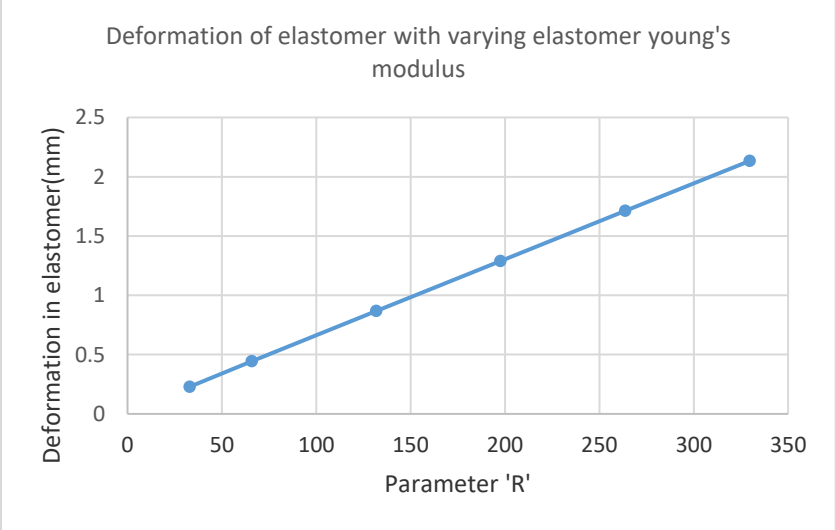

Figure 3.26 Variation of deformation in elastomer with young's modulus of elastomer

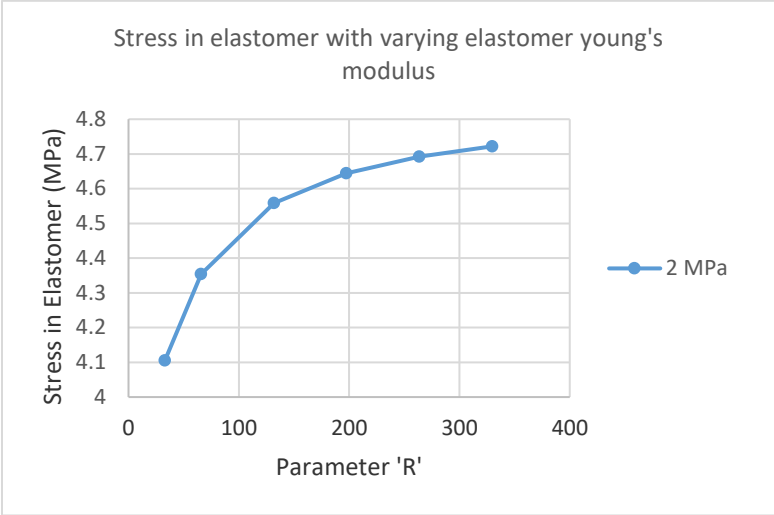

Figure 3.27 Variation of stress in elastomer with young's modulus of elastomer

From this parametric study, it can be concluded that the modulus of elasticity of the elastomer must be as high as possible in order to reduce the deformation and stress values observed in the RDS.

3.3.3 Fiber-Elastomer Combinations

Nylon and silicone were used as materials for the fiber and elastomer respectively in the previous parametric FEA simulations. In an attempt to find out the best combination of fiber-elastomer materials that could withstand higher pressures, a study has been carried out where various combinations of fibers and elastomer materials are analyzed, for the stresses and the deformation that they would see under increasing pressures. The different types of materials considered and the results obtained are discussed in this section.

Nylon, cotton, nomex, kevlar, polyester are the commonly used fibers and silicone, nitrile, fluorosilicone, hydrogenated nitrile, fluorocarbon, ethylene propylene, epichlorohydrin homopolymer, neoprene, epichlorohydrin copolymer, polyacrylate are the commonly used elastomer materials for the manufacturing of RDS [39]. Table 3.5 shows the properties of various elastomer materials, while Table 3.6 shows the properties of fibers.

Table 3.5 Properties of commonly used Elastomers in manufacturing RDS [39]

Elastomer	**Young's Modulus (GPa)**	**Poisson's ratio**	**Yield Strength (MPa)**
Silicone	0.005-0.05	0.48	7-11.5
Fluorosilicone	0.005-0.05	0.48	8.2-12.1
Nitrile	0.0018-0.0021	0.488	4-7
Hydrogenated Nitrile	0.0018-0.0021	0.488	6-10
Neoprene	0.00165-0.0021	0.488	12-24
Fluorocarbon	0.0025-0.0038	0.498	10-14
Epichlorohydrin Homopolymer	0.0015-0.0021	0.48	0.7-2.1
Epichlorohydrin Copolymer	0.0015-0.0021	0.48	1.4-2.8
Polyacrylate	7.8e-4-0.00165	0.48	1.3-3
Ethylene Propylene	7e-4 – 0.0017	0.48	1.5-2.5

Table 3.6 Properties of commonly used fibers in manufacturing RDS [39]

Fiber	**Young's Modulus(Y) GPa**	**Young's Modulus(X/Z) GPa**	**Poisson's Ratio**	**Yield Strength MPa**
Nylon	1.3-1.65	0.392	0.4-0.42	51.1-63.8
Cotton	5.5-28	2.4347	0.25-0.3	100-350
Nomex	1.01e-5-1.97e-5	0.8945	0.442-0.488	0.00356-0.00655
Kevlar	62-80	13.7693	0.35-0.37	2.5e3-3e3
Polyester	9.7-17.2	2.73015	0.333-0.367	25.1-55.2

As the fiber is orders of magnitude stiffer than the elastomer, the stress in both the fiber and elastomer for a given geometry should be nearly identical When FEA was carried out on the RDS with the fiber diameter being 0.3mm and the number of fibers are 120, stress in the fiber and in the elastomer was found to be 55.15 MPa and 6.22 MPa. As the FEA is linear, these values can be extrapolated to get the stress induced in the fiber and elastomer at different pressures. A similar discussion is presented later in this section for the cases with different fiber diameters and number of fibers. These stress values would remain approximately the same for any combination of fiber and elastomer (see Appendix C). Hence, it is enough to compare the stresses observed with different material properties to determine if they would fail. This helps to identify the combination of fiber-elastomer that can withstand maximum pressure.

Theoretically, one can argue that if the elastomer fails, the fibers can continue to take the load until the stress exceeds the failure strength of the fiber. But, in the case of rolling diaphragm seals, if elastomer fails, then it loses the capability to effectively withstand high pressures and hence failure of elastomer is considered to be failure of RDS. Going by this explanation, the following can be observed by comparing the yield strength of various fibers and elastomers presented in Table 3.5 and Table 3.6 with the stress induced in RDS under different conditions:

I. Kevlar has the highest yield strength of all the fibers and hence can support the highest pressure. As expected, by comparing the yield strength from Table 3.6 and stress induced in fibers at various pressures, it can be observed that Kevlar doesn't

fail even at 12MPa, but the elastomer materials that accompanies it fail at 2.6MPa if it is Fluorosilicone, 3.2MPa if it is Fluorocarbon and 3.9MPa if it is Neoprene.

II. Yield strength of cotton, nylon, polyester and nomex fibers is less than that of kevlar. Hence, any combination of these fibers with various elastomers would never be able to withstand pressures more than 2MPa.

From this study, it can be concluded that only Kevlar/Neoprene can withstand pressures close to 4MPa for the controlled case of 120 fibers with a diameter of 0.3mm. When the fiber diameter was increased to 0.5mm and number of fibers are changed to 180, it was found that Kevlar/Neoprene composite was able to withstand maximum pressure of 8.7MPa. Thus, it can be concluded that even with the increase in the fiber diameter or number of fibers, a significant increase in the pressure withstanding capability (saturating at around 8-9MPa) is not observed using any combination of fiber and elastomer.

3.3.4 Fiber Pattern

From the previous sections, it has been observed that the pressure withstanding capability of the RDS can be improved by using larger diameter fibers, a larger number of fibers and by using materials that have a higher young's modulus. Similar to these design variables, the nature of the fiber pattern within a given thickness of RDS seemed to be one of the major parameters that might improve the RDS behavior at higher pressures. Some of the possible fiber patterns will be discussed first in this section, which would then be followed by presenting remarks on how they affect the deformation and stress induced in rolling diaphragm seals.

Table 3.7 shows the various fiber patterns used for the study and a small description of each case shown in the figure is given below:

Case I: represents a 1^0 sector with a single fiber of 0.3mm diameter, resulting in 360 fibers when the sector is revolved around the center of the RDS.

Case II: represents a 1^0 sector with a single fiber of 0.4mm diameter, resulting in 360 fibers

Case III: represents a 1^0 sector with 2 fibers of 0.3mm diameter each, in 2 different layers, resulting in 720 fibers

Case IV: represents a 1^0 sector with 2 fibers of 0.4mm diameter each, resulting in 720 fibers

Case V: represents a 1^0 sector with 3 fibers, resulting in 1080 fibers in total. The inner fibers are 0.3mm in diameter and the outer fibers are of 0.2mm in diameter

Case VI: represents a 1^0 sector with 4 fibers, resulting in 1440 fibers in total. The inner fibers, middle fibers and outer layer fibers are of diameters 0.3mm, 0.2mm, and 0.3mm respectively.

Table 3.7 Fibers arranged in different patterns and the stress induced in them

Arrangement of Fibers	Stress(Mpa)	Arrangement of Fibers	Stress(Mpa)
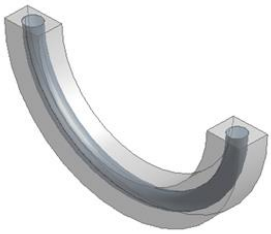 Case I	89.48	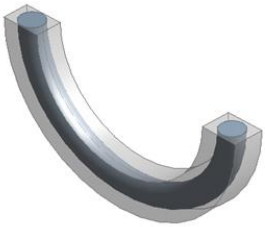 Case II	51.95

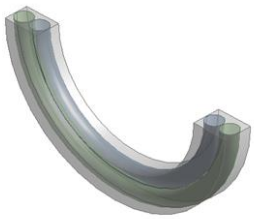 Case III	50.18 in inner fiber and 41.85 in outer fiber	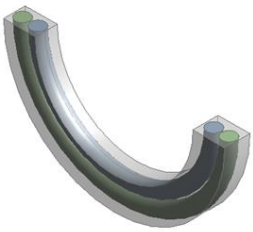 Case IV	31.20 in inner fiber 23.06 in outer fiber
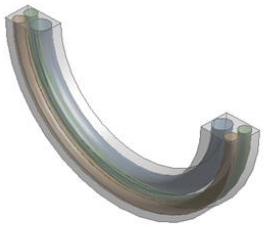 Case V	51.30 in inner fiber and 46.537 in outer fiber	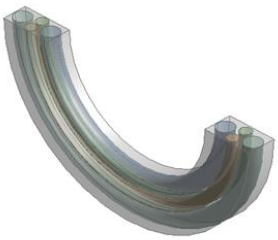 Case VI	39.60 in inner fiber, 34.08 in middle fiber and 27.00 in outer fiber

Theoretically, increasing the number of rows of fibers should have a significant effect in reducing the stress induced in the fibers, as it is equivalent to increasing the fiber volume fraction. FEA simulations on all the above described cases were conducted on a Nylon/Silicone RDS at a constant pressure of 8MPa. The maximum VonMises stress induced in the fibers, as shown in Table 3.7, was used as a measure to compare the performance of all the above cases.

Case I vs II: It was observed that the stress induced in fibers for case I and II were 89.48MPa and 51.95MPa respectively, where the yield strength of Nylon is 51MPa. Thus fibers in both the cases fail at 8MPa pressure.

Case (I and II) vs III: Even though 720 fibers of 0.3mm diameter each were used in case III, stress induced in the fibers is found to be around 50.18MPa in the inner fibers and

41.85MPa in the outer fibers, which is almost equivalent to the stress induced in the fibers in case II. Thus, in terms of effectiveness, case II is still better than case III.

Case IV: Stress induced in the fibers in case IV was around 31.20MPa in the inner fibers and 23.06MPa in the outer fibers. Thus it can be concluded that using 2 layers of fibers (like in III) would be useful only when we use little larger diameter fiber.

Case V: The stress induced was found to be 51.30MPa in the inner fibers and 46.54MPa in the outer fibers. From the standpoint of pressure handling, we can see that this case is not better than IV as it uses 1080 fibers, when compared to just 720 fibers in case IV and also resulting in an induced stress that is greater than what can be seen from case IV. Hence it is observed that case IV dominates case V.

Case VI: Considering that this case uses 1440 fibers, the amount of stress induced in the inner fibers is 39.60MPa, the middle fibers is 34.08MPa, and in the outer fibers is 26.99MPa. Hence, this case is similar to what can be seen from case IV except that case IV just uses 720 fibers. Hence again in terms of effectiveness, case IV seems to a better option compared to case VI.

From the above case studies, following conclusions can be drawn:

1. Fiber diameter plays a more important role in handling the pressure than the number of fibers and the fiber pattern used.
2. By comparing case IV with all the other cases, it can be observed that using different fiber patterns might be an effective alternate to improve the pressure withstanding capability.

3.4 Conclusions

This chapter describes the various parametric finite element analysis studies carried out on rolling diaphragm seals to understand the effect of various design parameters on its pressure withstanding capability. Only the convolution portion was analyzed as it is the most critically stressed part of RDS. The fiber and elastomer were modeled individually with a bonded contact defined at their interface. Cyclic symmetry boundary conditions were used to significantly reduce solver time. An APDL code was also written to calculate the volume averaged VonMises stress and deformation, which was then used to compare the performance of one RDS with that of another.

The effect of different design parameters like number of fibers, fiber diameter, young's modulus of elastomer, and fiber pattern on behavior of RDS was explored. Increasing the number of fibers and fiber diameter improved the pressure withstanding capability of RDS by reducing the deformation and stress induced in the elastomer. Similarly it was found that using an elastomer with high young's modulus improves the RDS performance. Further, it was observed that using different fiber patterns might be an effective alternative to improve the pressure capability.

4. Structural Finite Element Analysis of Cam Pump Assembly

4.1 Introduction

The 3 cylinder, 10cc/rev third generation variable displacement linkage pump (VDLP) presented in chapter 2 achieved high efficiency at all displacements and also performed well at low shaft speeds. However, the weight of the pump and its flow ripple limits its use in many applications. The cam driven variable linkage pump, mentioned in section 1.1.2 addresses these issues by replacing the crank and coupler links with a cam and roller-follower, as shown in Figure 1-5, thereby increasing the power density of the resulting pump. Additionally, the torque ripple can be controlled through design of the cam profile and the displacement of pump can be increased by using a multi-lobe cam. Figure 4.1 shows a radial cam-driven VDLP with 3 lobes and 5 pistons.

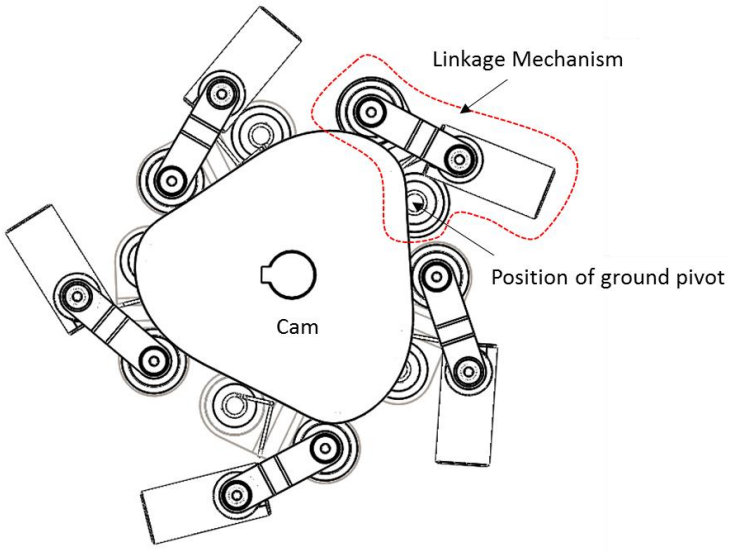

Figure 4.1 Cam driven adjustable linkage pump with 3-lobe cam and 5 linkage mechanism assemblies

This pump design was optimized for efficiency, piston side load, pump size, and torque ripple. The working principle and a description of its components will be discussed in next section.

4.1.1 Working principle of cam driven adjustable linkage pump

As observed in the isometric and exploded views shown in Figure 4.2, the primary linkage mechanism consists of a piston-cylinder, connecting rod, rocker link, and cam-follower pair. The roller-follower is connected to the joint between the rocker link and the connecting rod. As the cam rotates, the roller-follower causes the rocker link to oscillate about the movable ground pivot. The rotation of the rocker link drives the connecting rod, causing the piston to reciprocate in the manifold.

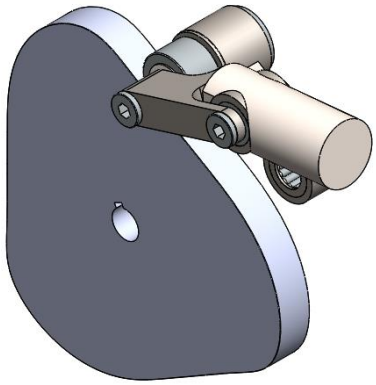

(a) Isometric View of the Linkage Mechanism Assembly

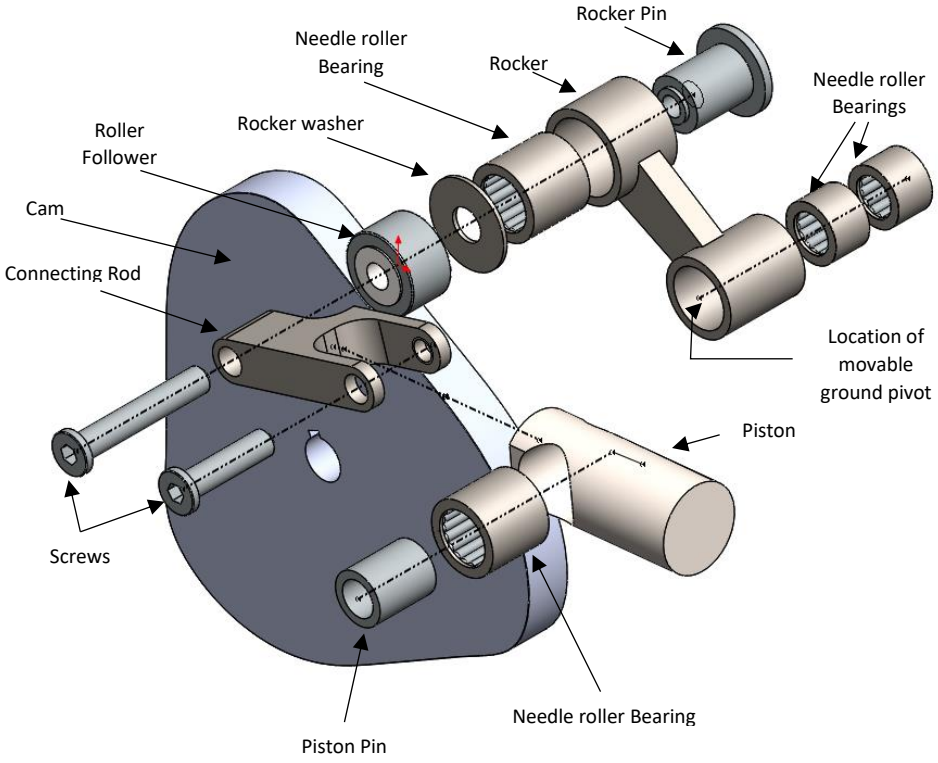

(b) Exploded View of cam driven linkage pump

Figure 4.2 (a) Isometric (b) Exploded view of the cam driven linkage pump

Similar to the third generation crankshaft driven VDLP, the displacement of the cam driven pump is varied by moving the adjustable ground pivot through an arc with a hydraulic actuator, as shown in Figure 4.3. The figure shows the back view of the cam with the adjustment mechanism and the isometric view of the adjustment mechanism along with the linkage mechanism.

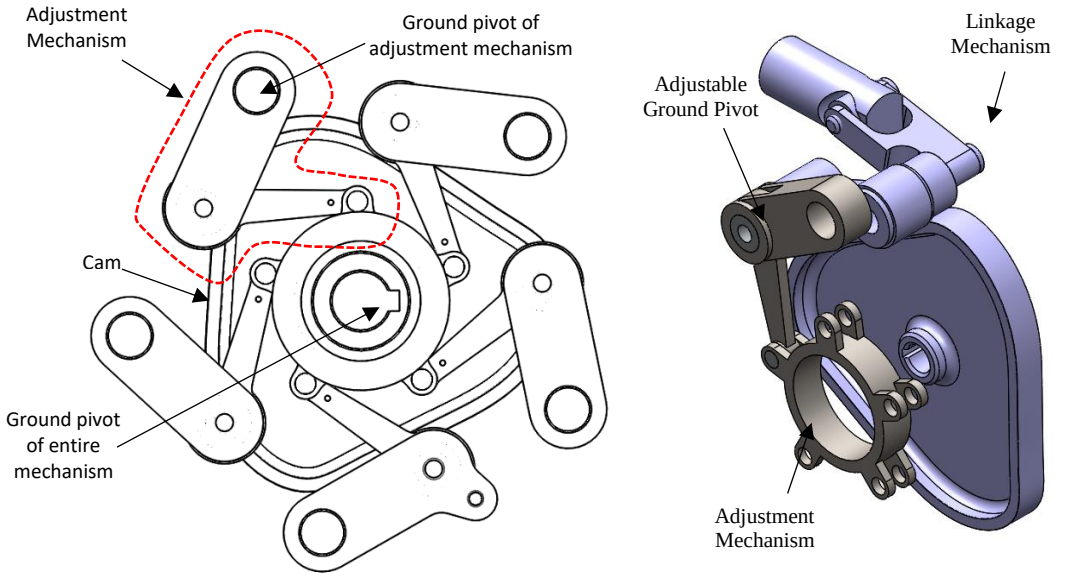

Figure 4.3 Back view and isometric view of the cam driven VDLP

The adjustment and linkage mechanism assemblies are connected near the adjustable ground pivot. The adjustable ground pivot shown in the Figure 4.3 connects to the adjustment ring using the adjustment link and adjustment pin as shown in Figure 4.4. Since there are five rockers in the pump assembly, the adjustment ring is designed to connect to all the five ground pivots with the adjustment links.

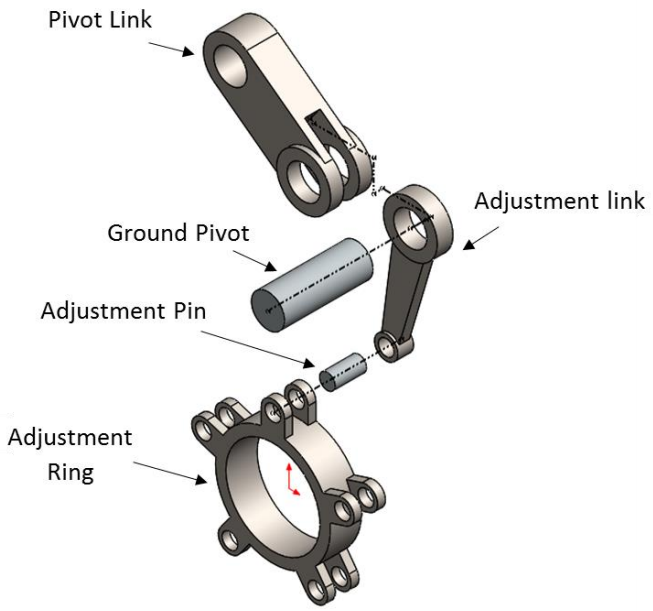

Figure 4.4 Exploded view of the adjustment mechanism assembly

In summary, the cam driven VDLP provides a large displacement in a small package because of the multiple strokes of each piston during every rotation of the multi-lobe cam and the compact radial packaging. The adjustable ground pivot of the rocker moves along an arc when the adjustment ring is rotated, thereby providing the necessary variable pump displacement. The cam pump is more compact, lightweight and power dense than the crankshaft driven third generation VDLP.

The entire pump design was led by Dr. Shawn Wilhelm and the author's role in the project was to analyze the stresses and deflections of the mechanism and aid in driving design iterations. The need for design iterations will be discussed in the next section.

4.1.2 Need for improving the stiffness of linkage assembly

The links of the cam driven mechanism are in offset parallel planes to avoid link to link interference. When hydraulic force is applied on the piston, each link is put into bending due to the multiple planes of the mechanism. This bending load causes deflection of the links, pins, and bearings, resulting in a reduced piston stroke with increased pressure. In addition, these bending loads create additional friction in the bearings, reducing the mechanical efficiency.

To minimize the mechanism deflection, a focus of the detailed design of the pump was on enhancing the stiffness of the linkage mechanism assembly. This was achieved by changing the geometry of the connecting rod and rocker links, and changing the position of the piston with respect to the cam. One of the most efficient ways to drive the design process is by using Finite Element Analysis (FEA) as a design tool. Design iterations can be performed faster and the analysis results can be used to make the necessary design decisions to obtain a stiffer linkage assembly with reasonable stress levels.

A great deal of caution needs to be taken when defining contacts, generating the mesh and applying simplified boundary and loading conditions in order to execute the FEA rapidly, accurately and without any convergence issues. The linkage mechanism assembly comprises of more than ten different components, making the multi-body simulation more challenging to execute using limited computational resources and within a limited time interval. Various ways to approach a multi-body FEA simulation, development of a

simplified bearing model and the method of using the analysis results to drive the design process are the focus of this chapter.

4.1.3 Overview of chapter

The objective of this chapter is to present the method of using multi-body static structural FEA to drive the design of the cam-driven VDLP mechanism assembly. Section 4.1 presented the advantages of the cam driven VDLP compared to the crankshaft driven VDLP, as well as the need for using FEA as a design tool to improve the stiffness of the linkage mechanism assembly. Section 4.2 presents a detailed description of setting up a multi-body FEA problem, where the emphasis is on explaining why a given combination of linear and nonlinear contacts were used at various joints and how local and global mesh controls and simplified boundary and loading conditions can be applied to obtain realistic and accurate results without convergence issues. A simplified bearing model that reduces the computational time is also discussed in this section. In section 4.3, FEA is used as a design tool to improve the stiffness of the linkage mechanism assembly by carrying out three design iterations. Section 4.4 contains concluding remarks.

4.2 Finite element analysis of cam pump linkage assembly

The stiffness of the pump linkage mechanism is important to the volumetric efficiency and reducing frictional losses at various joints. For the initial analysis, the adjustment mechanism assembly is assumed to be sufficiently rigid to prevent significant deformation under load.

4.2.1 Setting up base model for analysis

The initial design, referred to as the base model, was used to guide the FEA analysis decisions. Simplifications made to the CAD geometry, local and global mesh controls used, boundary and loading conditions applied, contacts enforced at various joints of the base model, and simplified bearing model are discussed in the next few sub sections.

4.2.1.1 Geometry

Figure 4.5 shows the side and top views of the base model of the linkage mechanism assembly. All the components are manufactured using alloy steel. The cross section views of the linkage assembly at planes A, B, and C as shown in Figure 4.5 are presented in Figure 4.6. This figure shows how various components of the assembly are connected together.

1. The cross section view at plane A shows how the connecting rod and piston fit together using a low head socket cap screw, needle roller bearing and piston pin.
2. The cross section view at plane B shows how the connecting rod, roller-follower and rocker are connected using a low head cap screw, rocker washer, rocker pin and a needle roller bearing.

3. The cross section view at plane C shows how the rocker and ground pivot fit together using two needle roller bearings

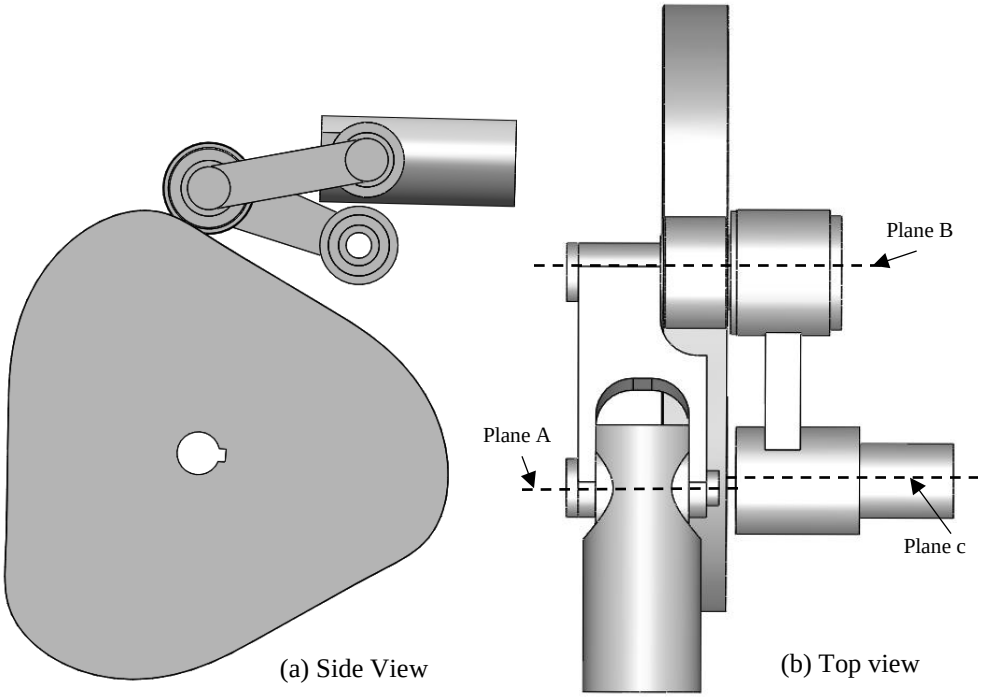

Figure 4.5 Side and Top views of Base Model (Initial design)

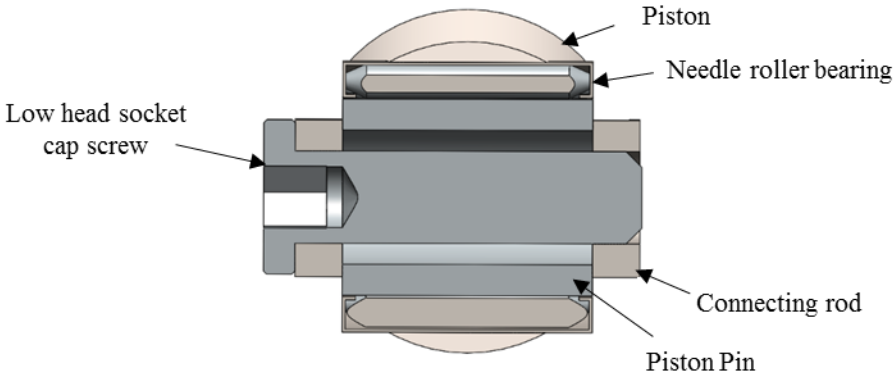

(a) Cross section view at Plane A

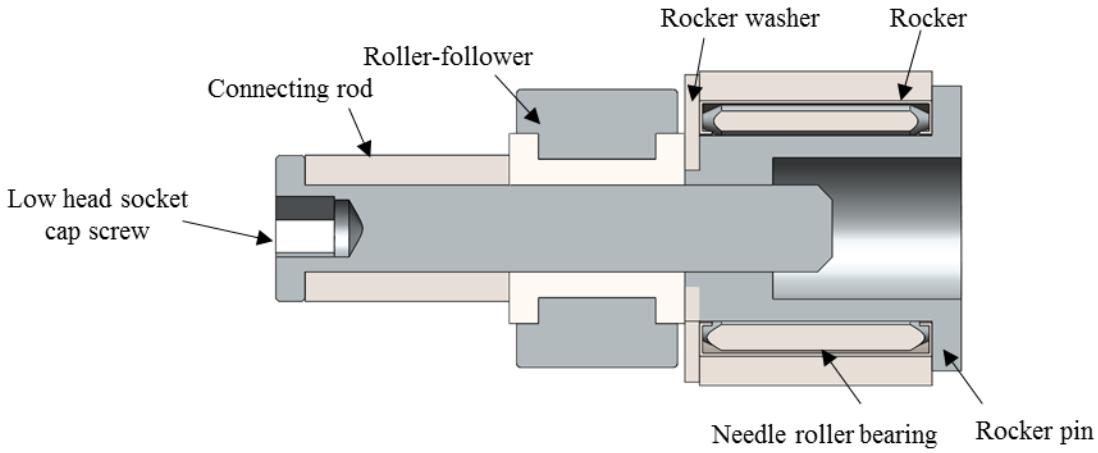

(b) Cross section view at Plane B

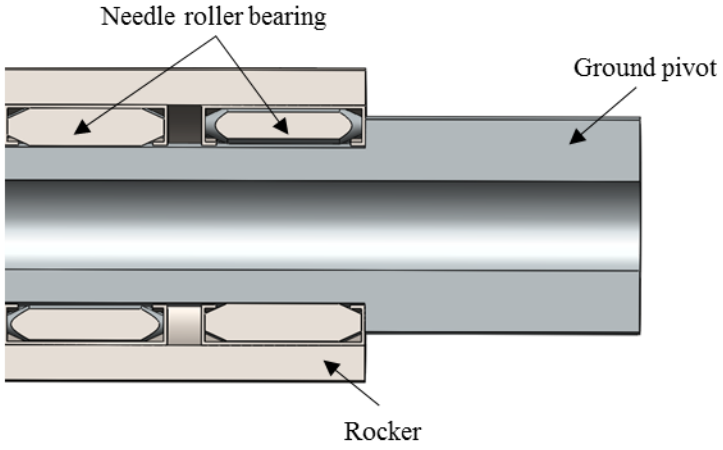

(c) Cross section view at Plane C

Figure 4.6 Cross section view of linkage assembly at (a) Plane A (b) Plane B (c) Plane C

CAD models of the low head socket cap screws were simplified for the analysis to reduce the computational time, as shown in the cross section views in Figure 4.6. The threads of the screws were neglected because the sharp threads result in bad quality mesh elements and demanded additional solver time. As the threads do not have any significant effect on the deformation or stress in the linkage, they were ignored in the analysis. No bolt pretension was applied on the screws. Instead they are assumed to be in bonded contact with the parts they are screwed into.

4.2.1.2 Mesh

The following steps were implemented to generate the mesh on the mechanism assembly and to improve it in order to obtain an accurate solution:

1. First, global mesh controls (like relevance center, mid-side node controls, element size etc.) were used to make adjustments on a global/assembly level. Relevance center, one of the global meshing controls in ANSYS, provides a control of the fineness of the mesh for the entire model. Instead of using the default option for relevance center, “fine” option was chosen to improve the fineness of the mesh on a global level for the entire linkage assembly.

   Improvement in the mesh on a global scale by changing the relevance center from “coarse” to “fine” can be observed from Figure 4.7(a) and Figure 4.7(b) respectively. However, it can be observed from Figure 4.7(b) that the connecting rod and rocker have just two and one element respectively across their thickness,

which is too coarse for an accurate solution. Hence, body sizing controls (local mesh control) were applied to address this situation.

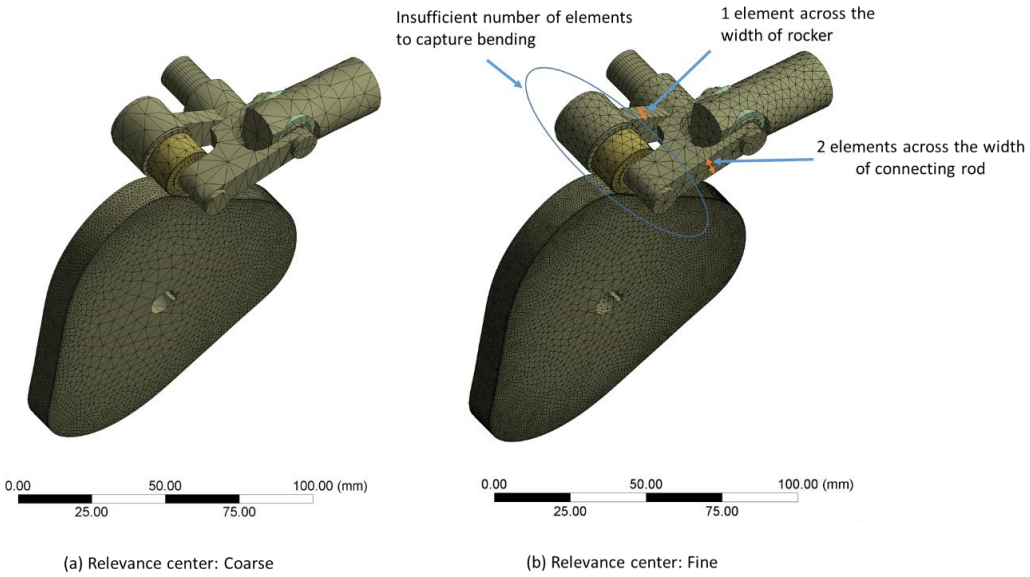

Figure 4.7 Improving the mesh using global mesh controls in ANSYS

2. The "body sizing" option in ANSYS imposes a local maximum size on all elements that are inside the boundary of the body. This option was used to refine the mesh on the follower, rocker, connecting rod, piston and the components used to connect them. A mesh convergence study was conducted to find out the right body size on all the critical parts as shown in Table 4.1 Case I refers to the mesh obtained after using global mesh controls (Figure 4.7). Case II, III, IV and V refers to a body sizing of 3mm, 2mm, 1mm, 0.75mm respectively applied to the components discussed above.

Table 4.1 Mesh convergence study

	Case I	Case II	Case III	Case IV	Case V
Element Number	93,074	93,707	114,043	403,368	607,692
Node Number	190,237	190,650	223,032	662,236	936,982
Axial piston deformation	2.031 mm	2.015 mm	2.004 mm	1.960 mm	1.953 mm
Maximum deformation	3.713 mm	3.689 mm	3.675 mm	3.634 mm	3.628 mm
Contours	Discontinuous	Continuous	Continuous	Continuous	Continuous
Solver time	1.17 hours	1.48 hours	2.37 hours	5.76 hours	8.57 hours

From Table 4.1, it can be observed that the axial piston deformation and the overall deformation converged by case IV (with body sizing of 1mm). Case V saw only a 1.6% change in piston displacement with a significantly higher computational time. Hence, the mesh generated in case IV, as shown in Figure 4.8, was used for further analysis.

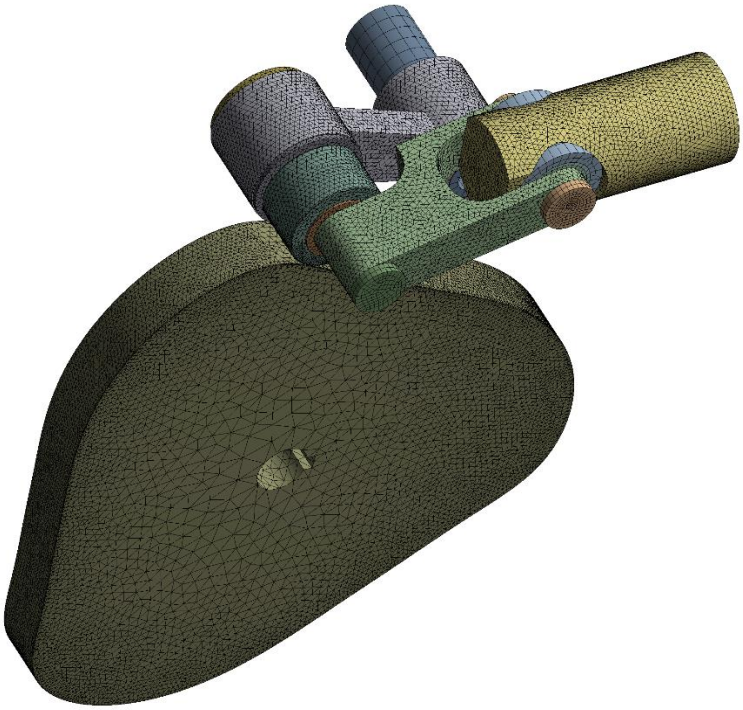

Figure 4.8 Mesh generated on linkage mechanism assembly after applying global and local mesh controls

3. Identifying the maximum contact stress near the cam-roller contact and the amount of roller slide on the cam are important to the design. Enhancing convergence and the quality of results for structural contact requires the use of the *contact sizing option* in ANSYS to create similarly sized meshes where faces and bodies are in contact. Once a contact sizing option is set at an interface, a relevance option[5] can be chosen to control the size of elements at that interface.

   Another mesh convergence study was conducted using the mesh generated in Case IV discussed before as the base case. The relevance option was changed from 2 to

[5] Relevance in contact sizing option refines the element size at interface "relative" to the original element size.

1.5 to 1 to 0.5 and it was observed that the results converged well when the option was set to one with a reasonable solver time.

Using the above discussed three steps, a quality mesh was generated and then evaluated against metrics such as element quality, aspect ratio, and skewness. This mesh was used for all the simulations discussed from here on in this chapter.

In an assembly, whenever individual components tightly fit together and where contact stresses between interfaces is not critical for the analysis, they can be merged into a single part. Mesh generated on such parts of the assembly is called as a conformal mesh, where node connectivity is maintained across the components of the part. In the current geometry, a conformal mesh was generated on the connecting rod, low head cap screw, and piston pin as well as on the low head cap screw, roller, rocker pin and rocker washer as shown in Figure 4.9.

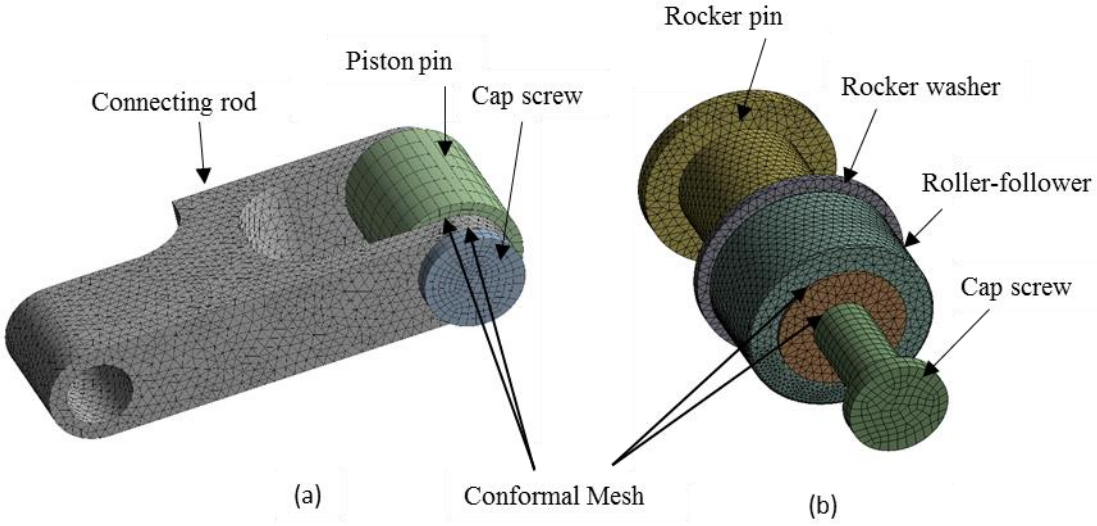

Figure 4.9 conformal mesh on (a) connecting rod, screw, piston pin and bushing (b) follower, screw, rocker pin and washer

4.2.1.3 Loading and Boundary Conditions

The input force to the FEA was a 12 kN hydraulic force acting on the piston in the direction shown in the Figure 4.10. The piston translates inside of the cylinder bore. In the model, this is captured by constraining the piston displacement in all directions except along the *x*-axis as shown in Figure 4.10. Further, the center of cam and one end of the ground pivot are fixed. All the applied loading and boundary conditions can be seen in Figure 4.10.

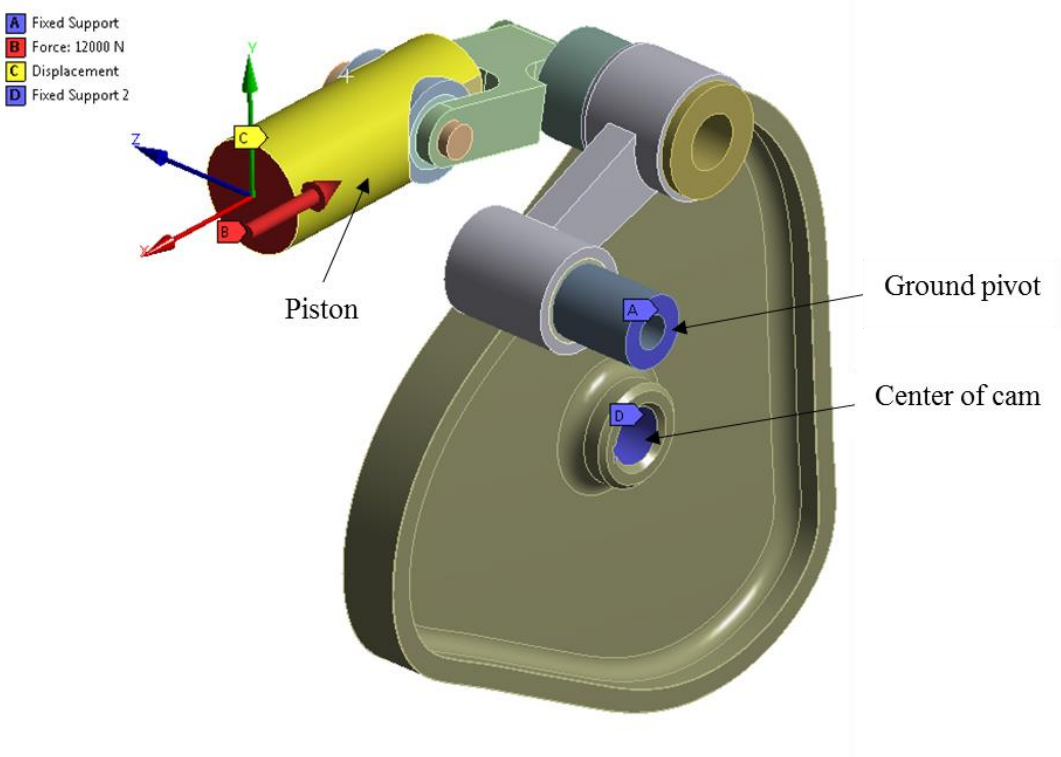

Figure 4.10 Boundary and Loading conditions on the linkage mechanism assembly

4.2.1.4 Contacts

As mentioned in chapter 3, whenever there is a chance that two surfaces might come into contact with each other, a contact has to be defined in ANSYS. Either linear contacts (bonded, no separation) or nonlinear contacts (frictionless, frictional, rough) can be defined at the contact interfaces. Linear contacts should be used when there is little or no movement between the surfaces. They are computationally inexpensive, but usually give inaccurate results when enforced at surfaces that have large relative motion or gaps that change in size as the load is applied. Non-linear contacts can be used in such cases, but they are more computationally expensive [5]. The primary contact options include:

1. *Bonded contact* ensures that the surfaces will be together irrespective of gap, penetration and loading.
2. *No separation contact* does not allow the separation of geometries in contact
3. *Frictionless contact* allows the two surfaces to slide freely and the gap can open and close depending on the loading.
4. *Rough contact* ensures that the surfaces can separate depending on loading but cannot slide
5. *Frictional contact* allows the surfaces to slide based on the user defined coefficient of friction and separation is allowed.

A combination of linear and nonlinear contacts were used in this analysis, as shown in Figure 4.11. The augmented Lagrange contact algorithm [5] was selected for all of the contacts, allowing ANSYS to perform a contact search at gauss integration points of each element. The selection of the contacts at each joint is discussed in section 4.2.2.

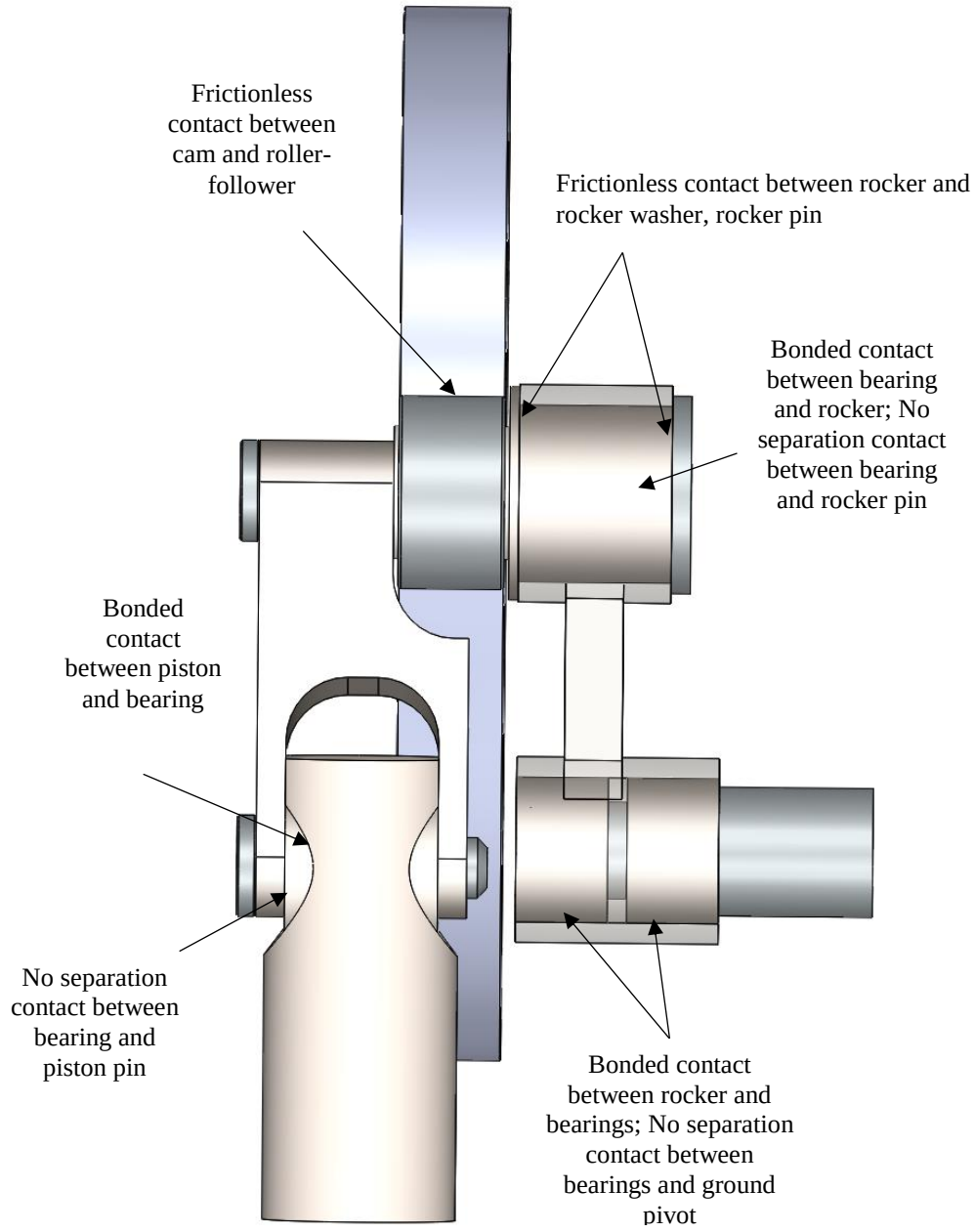

Figure 4.11 Linear and Nonlinear contacts enforced at various joints in the cam pump linkage assembly

4.2.1.5 Bearing Model

As mentioned in section 1.1.2, from the view of computational cost, it is not feasible to model the full detail of the multiple rolling elements in the bearings due to the large number

of contacts between the individual rollers and races. In an attempt to reduce the number of contacts and to speed up simulations, an equivalent fictitious young's modulus for the bearings is calculated and the entire bearing with rollers and inner and outer races is substituted with a bushing of same dimensions, but made of material with the calculated equivalent young's modulus, as shown in Figure 4.12. It should be noted that the bearing model was developed to simplify the process of capturing the deflection of bearings during FEA, while the expected life and bearing ratings were used to select the bearings.

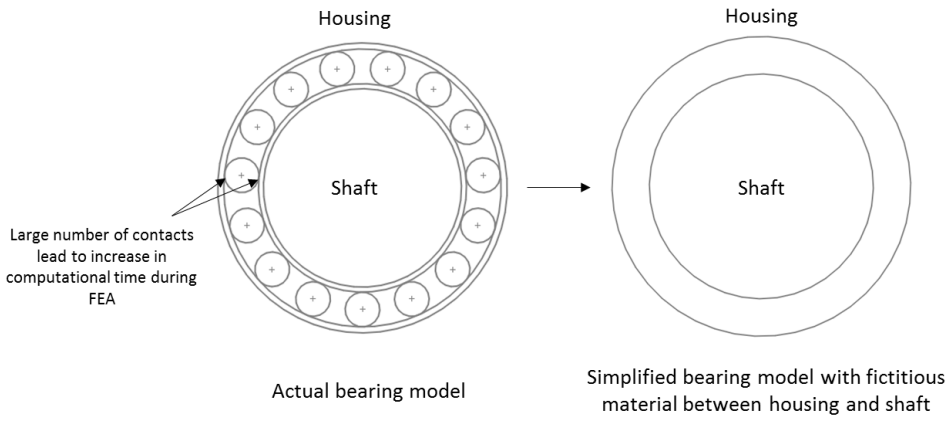

Figure 4.12 Actual vs. simplified bearing model

The force vs. deformation relationship in a roller-raceway contact is non-linear due to line contact and the force dependent contact area. Harris [5] and Houpert [6] developed many analytical relationships describing the behavior of tapered and cylindrical roller element bearings. While Houpert developed a uniform approach for both types of rolling element bearings, Harris developed individual relationships for both tapered and cylindrical roller element bearings. Analytical calculations developed by Harris are widely used in the

bearing industry today and hence were applied in obtaining the equivalent bearing's modulus for the simplified model.

Harris showed that the relationship between radial load acting on the inner ring of the bearing (F_r), maximum load that a roller experiences (Q_{max}), and the number of rollers (Z) is given by:

$$F_r = ZQ_{max}J_r \tag{4.2}$$

Where J_r, the Sjovall integral is defined as

$$J_r(\epsilon) = \frac{1}{2\pi}\int_{-\theta_1}^{\theta_1}[1 - \frac{1}{2\epsilon}(1 - \cos\theta)]^n \cos\theta \, d\theta \tag{4.3}$$

Where $\in = \frac{1}{2}(1 - \frac{P_d}{2\delta_r})$ and θ_1 represents the angular extent of the load zone in the bearing, which depends on the diametrical clearance (P_d) and radial shift of inner ring (δ_r) as

$$\theta_1 = \cos^{-1}\frac{P_d}{2\delta_r} \tag{4.4}$$

Diametrical clearance is an important parameter that effects stresses, deflection, load-distribution, and life in roller bearings and hence it also effects the equivalent modulus of the bushing. As the diametrical clearance in the bearings used in the pump was little to none, P_d is assumed to be zero in all the bearings in the linkage assembly, resulting in $J_r(\epsilon)$ to be equal to 0.2453. From equation 4.4, it can be observed that zero clearance corresponds to a case where the radial load applied on the inner ring is distributed onto half of the entire rollers in the bearings. However, the amount of radial load that each roller experiences varies with its angular position, with the roller at 0^0 taking up the maximum load (Q_{max})

as shown in Figure 4.13. Similarly, θ_1 would be less than 90^0 if clearance exists and it would be greater than 90^0 if the clearance is negative (preloaded bearing).

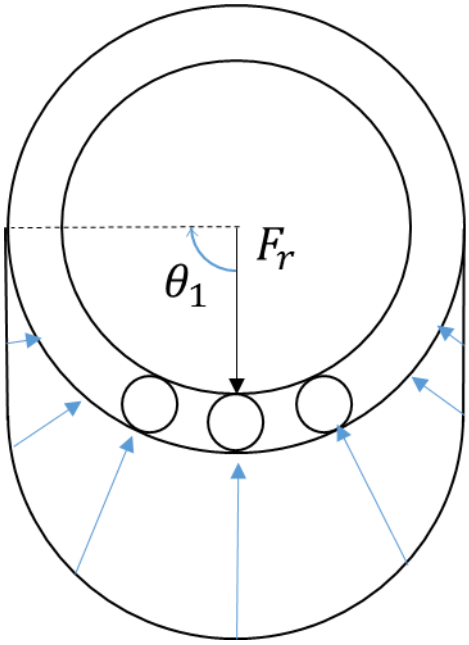

Figure 4.13 Rolling element load distribution in the case of zero diametrical clearance

The relationship between the maximum load experienced by the roller and the deformation, *u*, it undergoes is given by

$$Q_{max} = k_n u^n; \text{n} = 1.1 \text{ for roller bearings} \tag{4.5}$$

where the load deflection factor, $k_n = \frac{k_1}{2^n}$ and $k_1 = 7.86e4 * l^{\frac{8}{9}}$ (for steel roller-raceway contact)

This results in

$$F_r = Z k_n u^n J_r \tag{4.6}$$

$$\frac{dF}{du} = n u^{n-1} Z J_r k_n \tag{4.7}$$

Equations 4.6 and 4.7 describe the load-deformation and stiffness-deformation relationships. The load vs deformation for two bearings in the linkage assembly are plotted

in Figure 4.14. The maximum dynamic load rating of the bearings in the piston and rocker are 12.2 kN and 15.8 kN respectively. From Figure 4.14, deformation of the rollers at these forces would be 0.0088 mm and 0.0164 mm respectively.

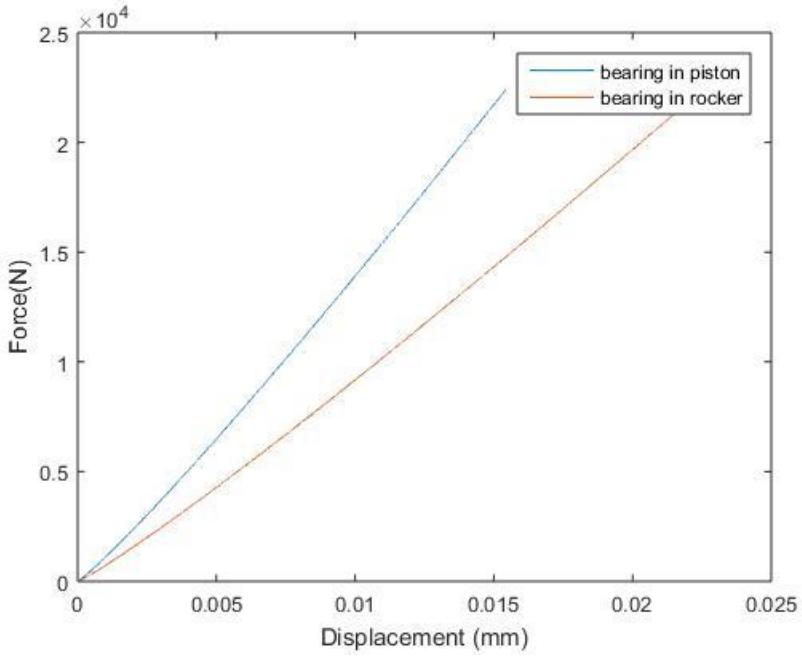

Figure 4.14 Force vs. deformation plot of bearings in piston and rocker

The row of needle rollers in the bearings can now be substituted with a bushing of equivalent elastic properties as the needle rollers. A 2-D FEA model was created with a bushing replacing the needle rollers between inner and outer rings. A bonded contact was used between the outer ring and bushing and a no separation contact was used between inner ring and bushing. The objective was to determine the modulus of elasticity for the bushing to create the same deformation as the rolling element bearing at the given radial load. Using an iterative analysis in ANSYS, elastic moduli of 9.525GPa and 8.35GPa was found for the bearings in piston and rocker respectively.

The amount of time needed to set up this model was less than the model developed by Claesson. However, this model cannot account for the changing stiffness of the roller elements with deformation. Further, axial and torsional stiffness of the rollers is not taken into account. The procedure mentioned above can also be used for ball bearings to obtain a simplified bushing model [5].

4.2.2 Linear vs. nonlinear contacts at various joints

A method of setting up a multibody static structural FEA of the linkage mechanism assembly was presented in the previous section. A combination of linear and nonlinear contacts were enforced at various joints of the assembly as shown in Figure 4.11. In this section, different contact types and their influence on the analysis results will be discussed in order to guide the selection of appropriate contacts. Contacts are varied at one interface at a time while holding the others fixed.

4.2.2.1 Cam-roller joint

In practice, the cam roller rolls and slides on the cam as hydraulic load is applied on the piston. Bonded or no separation contact allow no or little sliding near the interface. Figure 4.15 compares the base model of frictionless contact with a bonded contact at the cam-roller interface. It can be seen that using a bonded contact under predicts the maximum overall deformation in assembly by 82% and is thus, not an appropriate simplification.

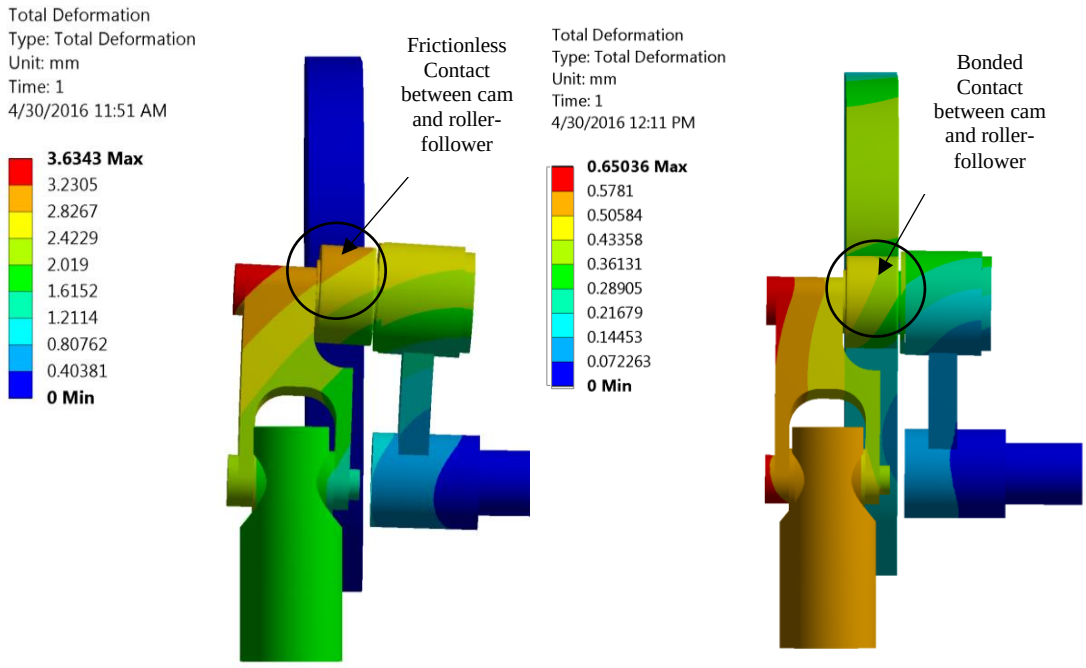

Figure 4.15 Linkage mechanism assembly deformation contour plot of (a) Base model (b) Base model with bonded contact enforced between cam and roller-follower

4.2.2.2 Bearing joint between rocker and rocker pin

Needle roller bearings are used between the rocker and rocker pin, where the outer race of bearing is fixed to rocker and the rocker pin acts as an inner race for the needle rollers. Bonded contact was defined between the outer race of the bearing (equivalent to outer surface of bushing in this analysis) and the rocker. However, if a bonded contact was used between the inner surface of bearing and the rocker pin, it would under predict the maximum deformation of the assembly by ~4.7% compared to the base model where no separation contact is used, as shown in Figure 4.16.

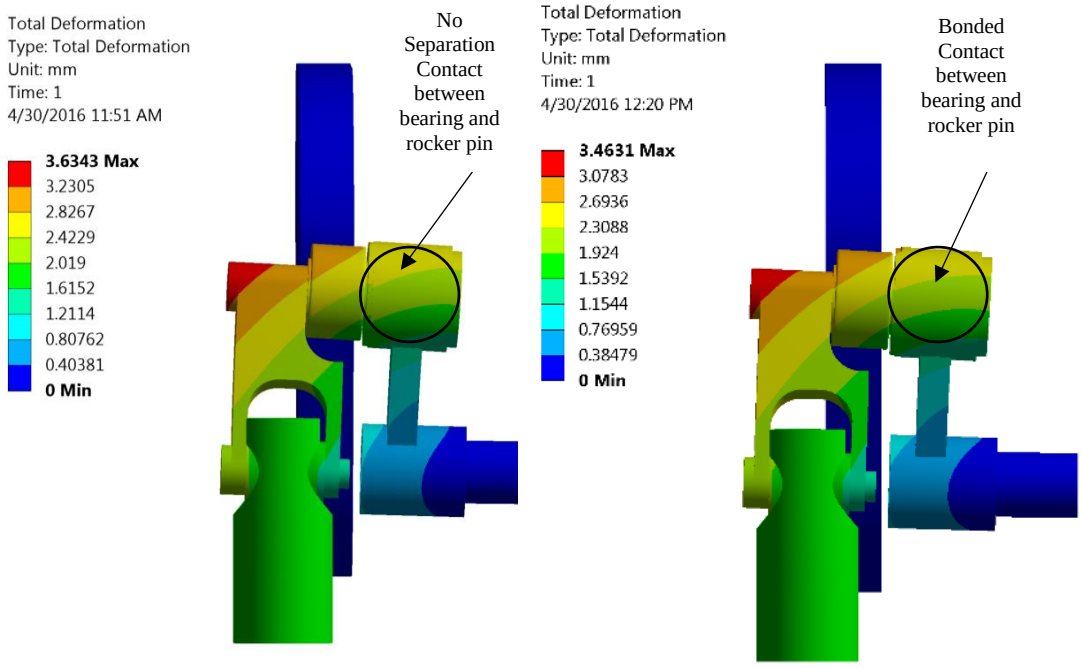

Figure 4.16 Linkage mechanism assembly deformation contour plot of (a) Base model (b) Base model with bonded contact enforced between inner surface of bearing and rocker pin

Using nonlinear contacts like frictionless and friction contact instead of no separation contact between the rocker pin and inner face of bushing would increase the complexity and solver time. Hence, to reduce computational time, no separation contact was defined between the bushing (needle roller bearing equivalent) and the rocker pin.

The joint between the rocker and ground pivot also uses a needle roller bearing rotating on a pin. Based on the findings at the rocker to rocker pin interface, bonded contact was used between the outer surface of bushing and the rocker, whereas no separation contact was used between bushing and ground pivot pin.

4.2.2.3 Sliding joint between rocker and washer, rocker pin

Axial motion of the rocker relative to the rocker pin is constrained by washers on both sides of the rocker, as shown in Figure 4.11. When the entire linkage assembly deflects about the ground pivot, some separation and rotational sliding occurs between the rocker and the washer, rocker pin. If a bonded contact were used, it would under predict the maximum deformation by ~6% compared to the base model where a frictionless contact is used, as shown in Figure 4.17. To allow the appropriate separation between the surfaces, frictionless contact was used between rocker, washers, and rocker pin.

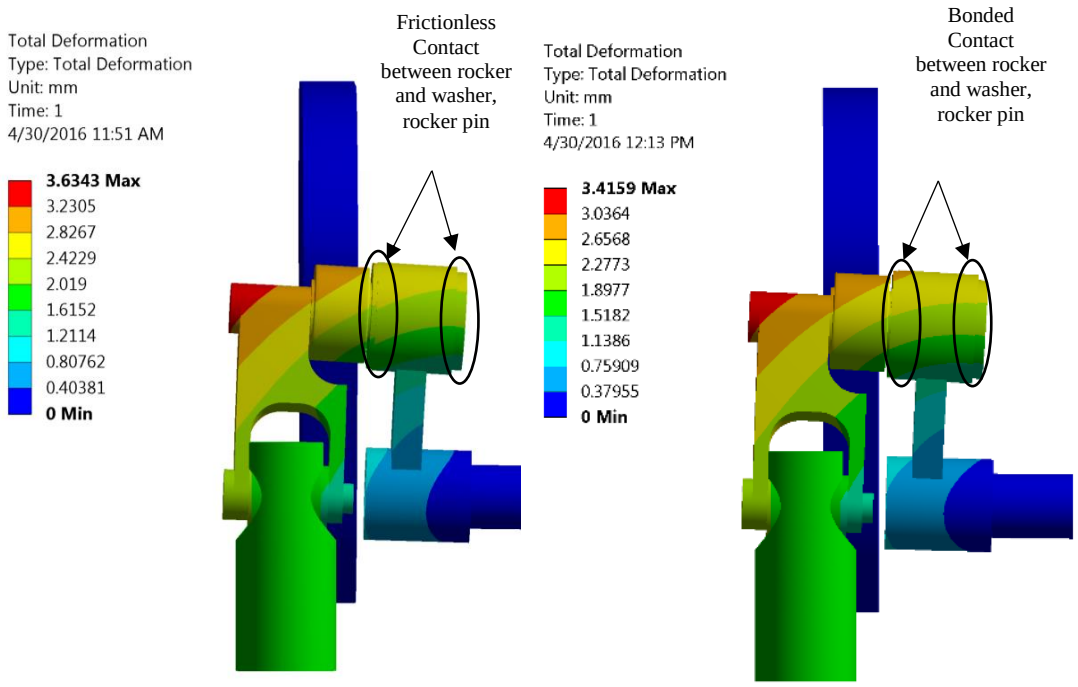

Figure 4.17 Linkage mechanism assembly deformation contour plot of (a) Base model (b) Base model with bonded contact enforced between rocker and washer, rocker pin

4.3 Design Iterations using FEA

The results of the static structural analysis performed on the linkage assembly are discussed in this section. Deformation of the linkage assembly about the ground pivot and the maximum VonMises stress are analyzed in order to assess the stiffness of linkage assembly and stress concentrations in various components respectively. This section describes three significant steps along the path of the numerous design iterations to address design deficiencies, thereby improving the stiffness of the linkage assembly.

4.3.1 Base Model

Results of static structural analysis performed on the base model are discussed in this section. Figure 4.18 and Figure 4.19 show the deformation of linkage mechanism assembly in isometric and top views respectively. The maximum deformation of 3.63mm was observed in the corner of connecting rod near low head cap screw. A large deflection was expected because the linkage assembly bends about the ground pivot and the roller slides axially on the cam. The maximum sliding of roller on the cam was found to be 2mm. A maximum deformation of approximately 3.2mm was observed in the rocker. Figure 4.19 shows that the deformation contours are centered about the ground pivot as expected.

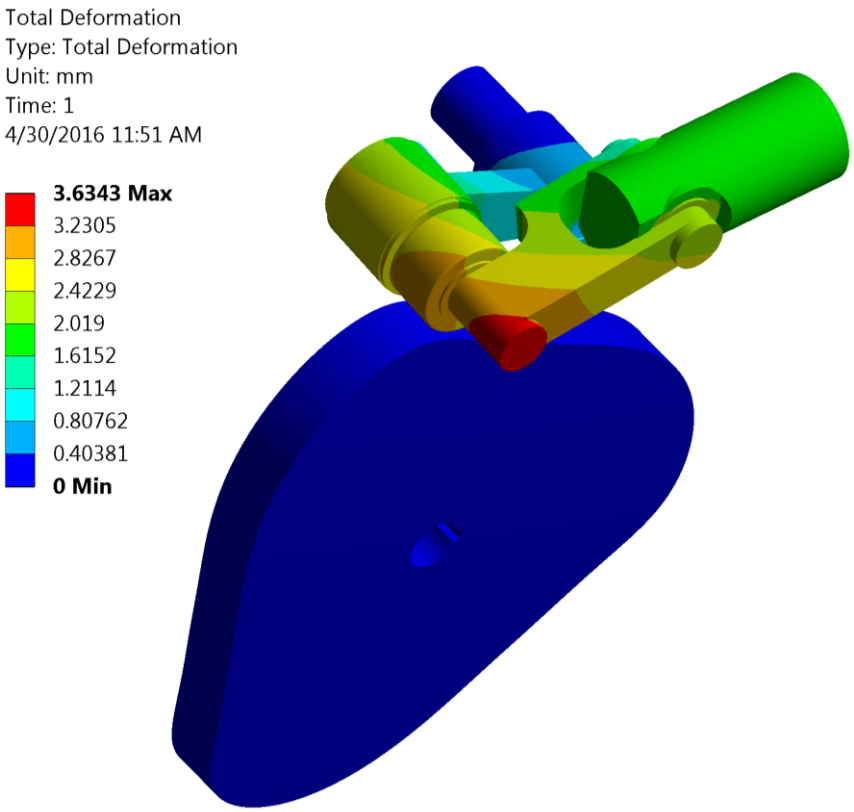

Figure 4.18 Linkage mechanism assembly deformation contour plot

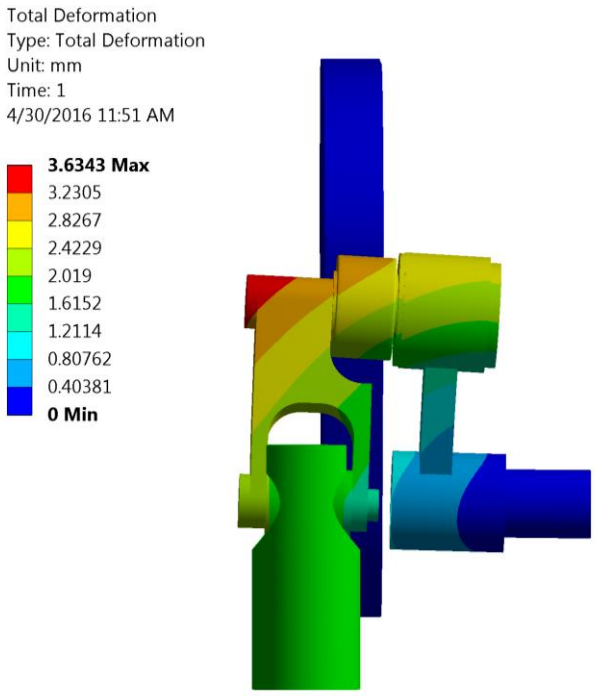

Figure 4.19 Top view of linkage mechanism assembly deformation contour plot

The pumping face of the piston deforms 1.94 mm in the axial direction (along the x-axis), as shown in Figure 4.20. Such a large axial deformation reduces the volumetric displacement of the pump.

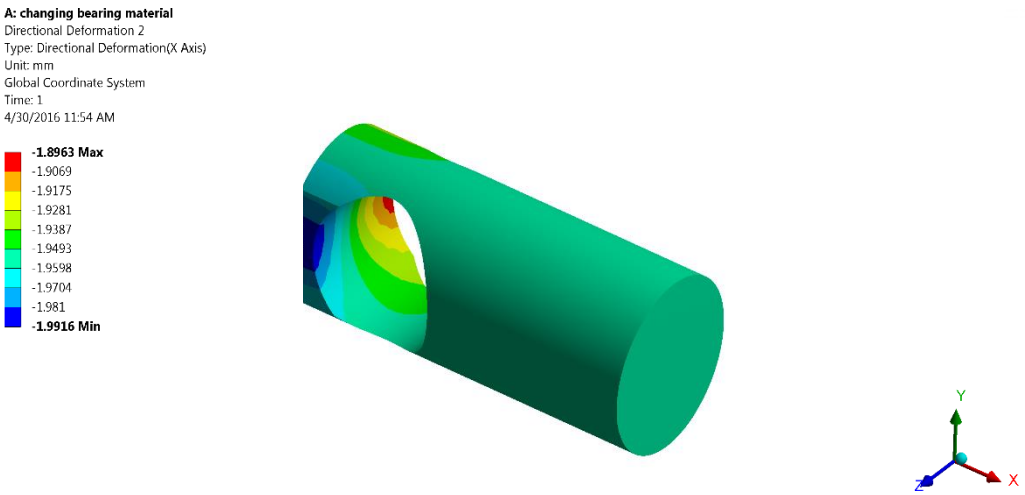

Figure 4.20 Axial piston displacement contour plot

Figure 4.21 shows the overall stress distribution in the linkage mechanism assembly. Numerical values of the stress observed in large portions of cam and piston are under 300MPa. The connecting rod and rocker both have sharp corners leading to high stress concentration, as shown in Figure 4.22 and Figure 4.23. The rocker does not offer much resistance to bending due to the thin cross-sectional area between the bearing supports.

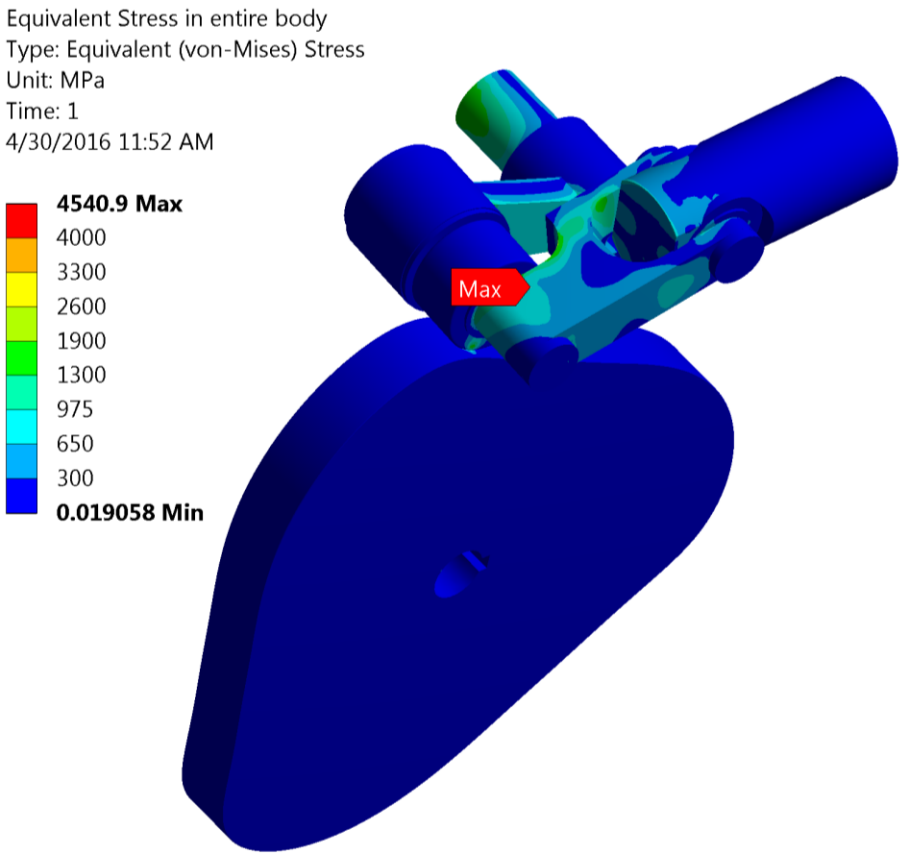

Figure 4.21 Cam pump assembly stress contour plot

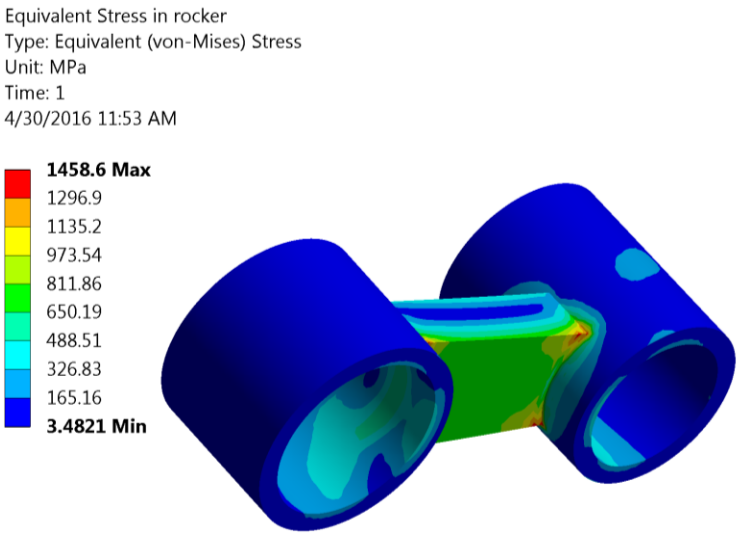

Figure 4.22 Stress contour plot of rocker

As seen in Figure 4.23, the two thin arms extending out from the connecting rod towards the piston and the L shaped groove on its top result in high stress regions in the connecting rod.

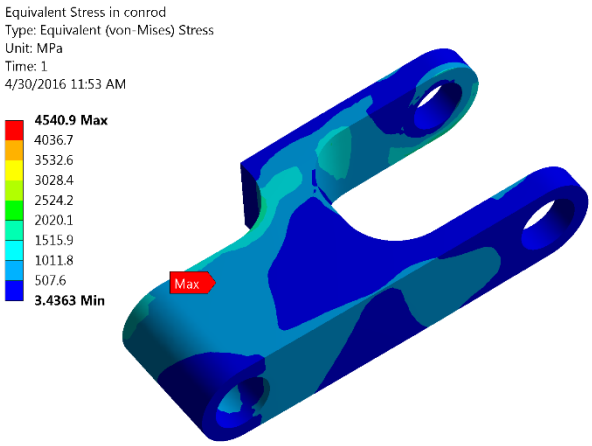

Figure 4.23 Stress contour plot of connecting rod

These results show that the linkage assembly is deforming a lot about the ground pivot, resulting in significant axial piston deformation. Further, stress concentration in the rocker and connecting rod are problematic. Design modifications made to reduce the axial

deformation of piston and alleviate the stress concentration in critical regions of rocker, connecting rod are discussed in sections 4.3.2 to 4.3.4.

4.3.2 Iteration 1

To reduce the mechanism deflection and stress concentrations, the piston position was changed by placing it in-line with the cam and the roller to decrease the moment of hydraulic force acting on the piston about the ground pivot, as shown in Figure 4.24. Figure 4.25 compares the change in the boundary conditions applied to the components because of including the adjustment mechanism assembly during the analysis.

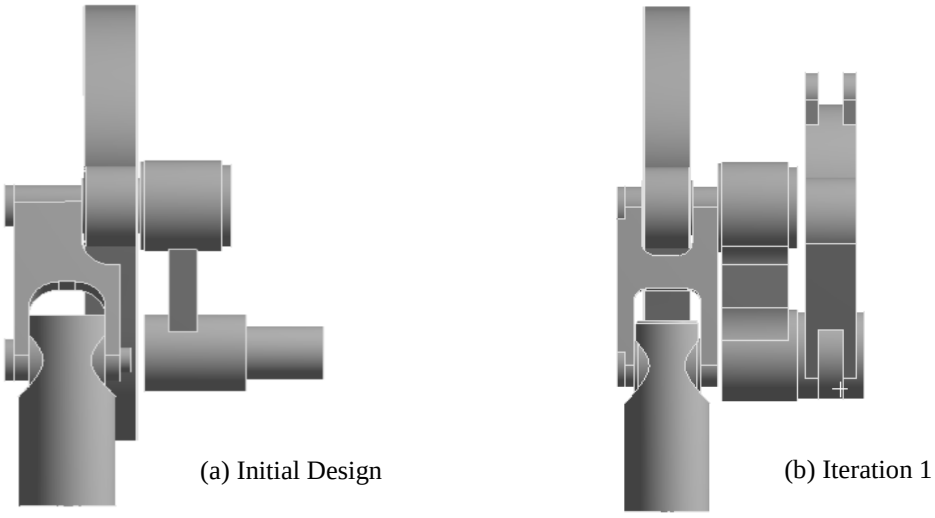

(a) Initial Design (b) Iteration 1

Figure 4.24 Top view of initial and iteration 1 cam pump assembly designs

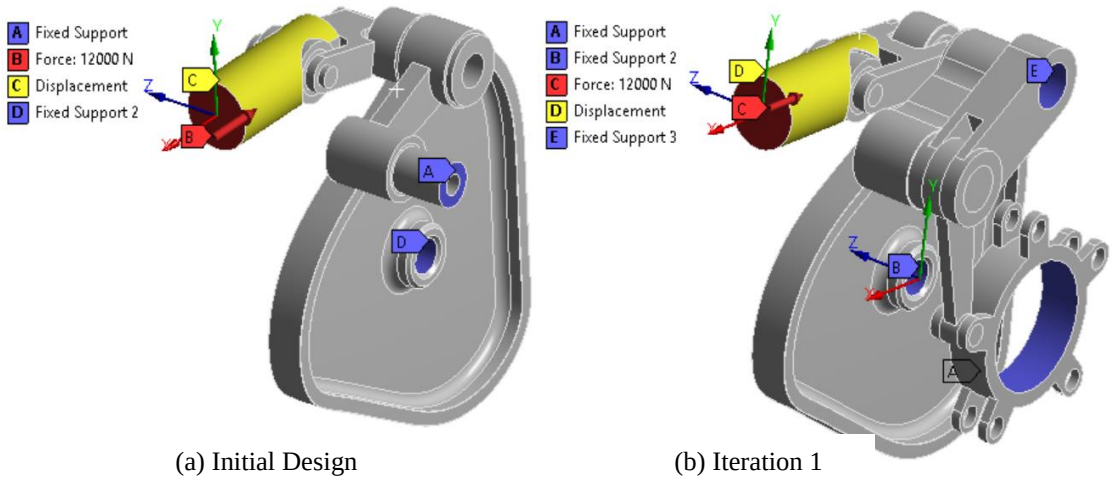

(a) Initial Design (b) Iteration 1

Figure 4.25 Boundary conditions of initial and iteration 1 cam pump assembly designs

The shape of the rocker and connecting rod were also changed significantly from the initial design to address the issue of stress concentration and improving the resistance to deformation of the assembly about the ground pivot, as seen in Figure 4.26 and Figure 4.27. The thickness of the arms of connecting rod was increased and it was modified to allow the roller to be placed between the arms. The thickness of the rocker in its middle portion was increased and fillets were included to avoid stress concentrations, as shown in Figure 4.27.

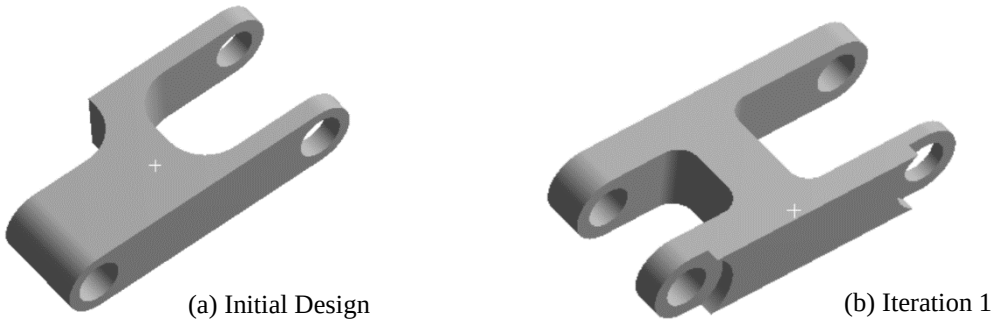

(a) Initial Design (b) Iteration 1

Figure 4.26 Comparison of connecting rod shape in initial design and iteration 1

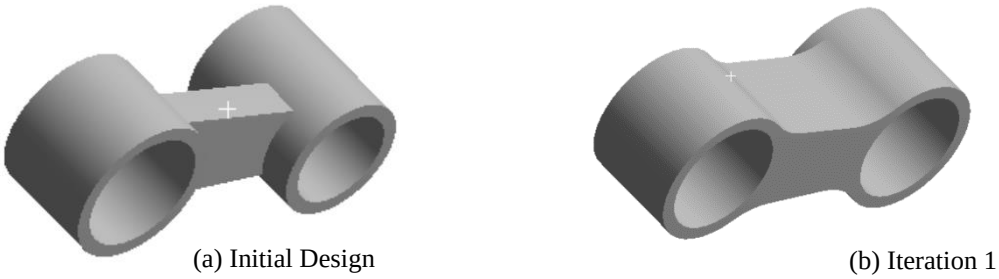

(a) Initial Design (b) Iteration 1

Figure 4.27 Comparison of rocker shape in initial design and iteration 1

Figure 4.28 and Figure 4.29 compare the deformation and stress in the initial design and the iteration 1 design assemblies. A 62.8% decrease in maximum deformation is observed in iteration 1, with a corresponding reduction in the axial displacement of the piston of 58%. The peak stresses are also decreased in comparison to the base model.

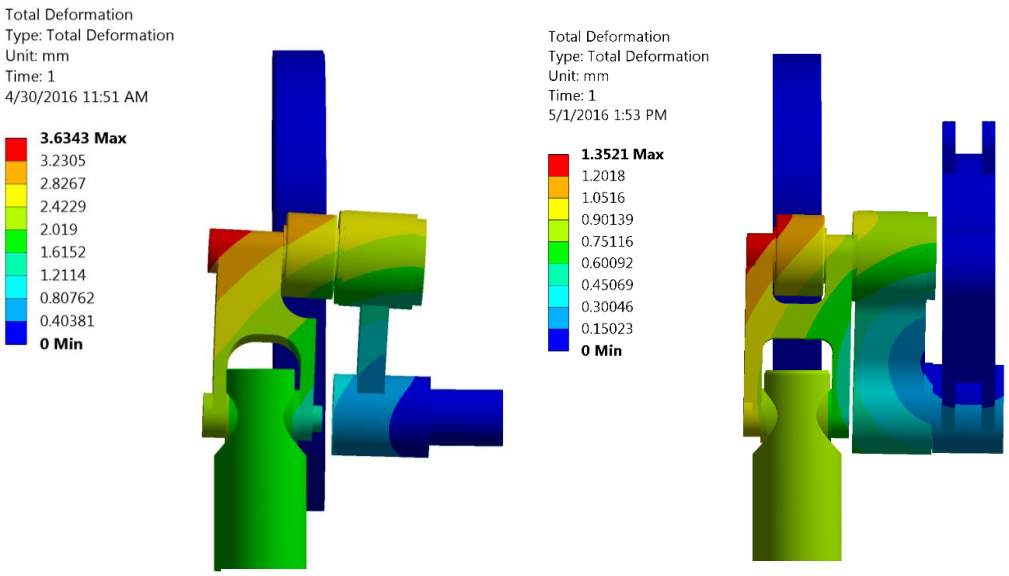

(a) Initial Design (b) Iteration 1

Figure 4.28 Comparison of cam pump assembly deformation contour plot in initial design and iteration 1

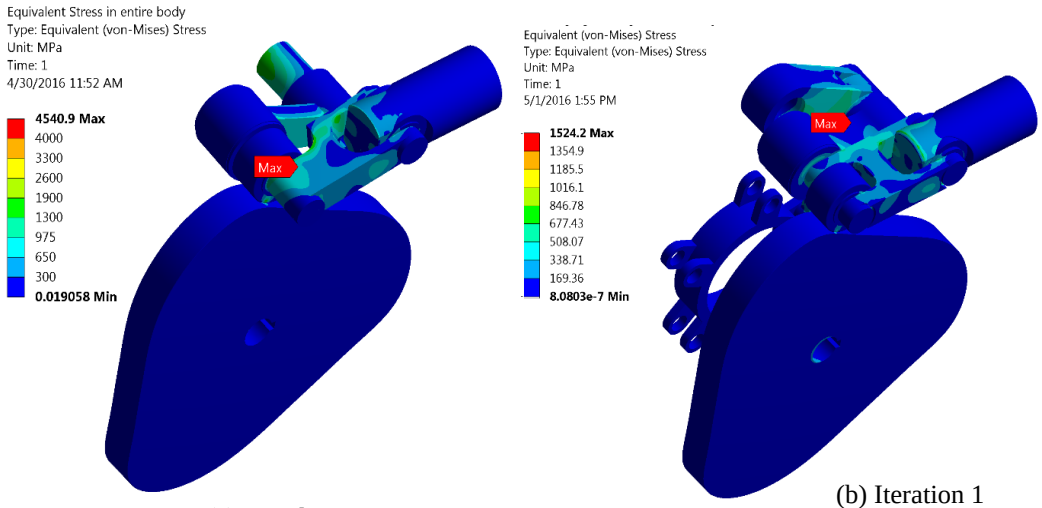

(a) Initial Design (b) Iteration 1

Figure 4.29 Comparison of cam pump assembly stress contour plot in initial design and iteration 1

Figure 4.30 shows that the stress concentrations in the rocker were reduced. The maximum VonMises stress in the connecting rod decreased over 4X in iteration 1, Figure 4.31, but is still quite high.

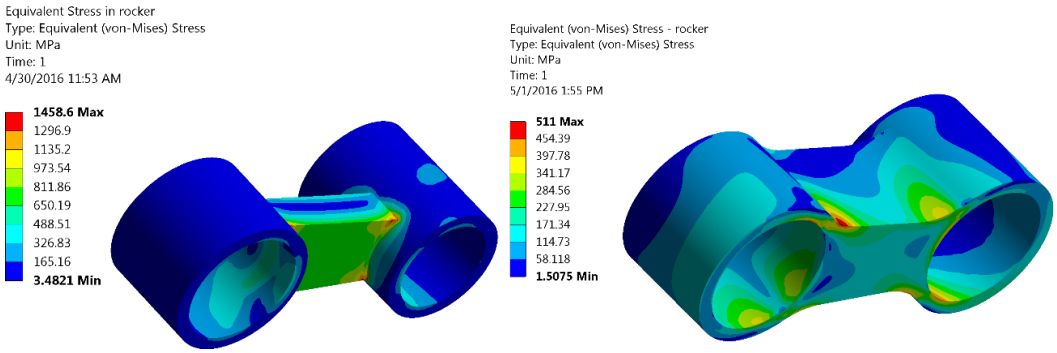

(a) Initial Design (b) Iteration 1

.

Figure 4.30 Comparison of rocker stress contour plot in initial design and iteration 1

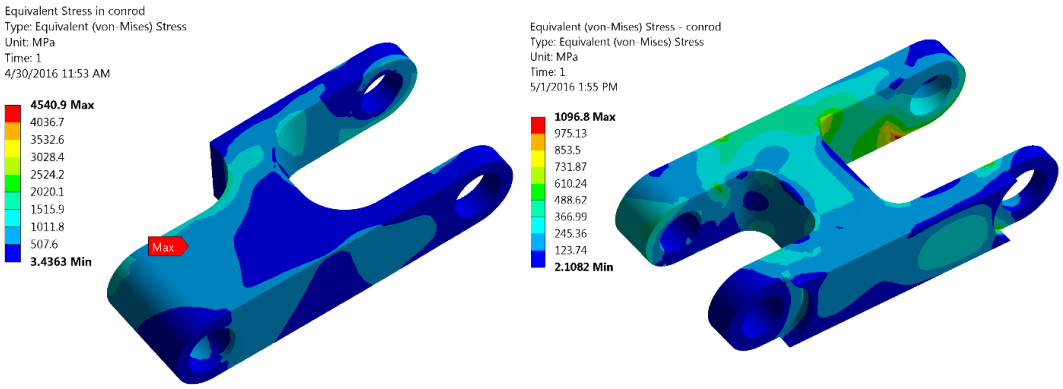

(a) Initial (b)

Figure 4.31 Comparison of connecting rod stress contour plot in initial design and iteration 1

Even though the axial piston displacement and maximum deformation of the assembly decreased in iteration 1, further reductions were required to meet the design specifications. Further design improvements were also needed on the connecting rod and rocker to address highly stressed regions.

4.3.3 Iteration 2

In order to reduce the deformation of the cam pump assembly, the axial distance between the piston and the fixed end of pivot link was decreased further in iteration 2, as shown in the Figure 4.32. While the piston was in line with the cam and the roller in iteration 1, in iteration 2, the piston was moved towards the adjustment mechanism, resulting in two opposing moments. The moment generated about the fixed end of pivot link in the adjustment mechanism is opposed by the moment generated near the cam-roller joint. Even though the latter is comparatively less than former, this new design can help to reduce the axial piston deformation.

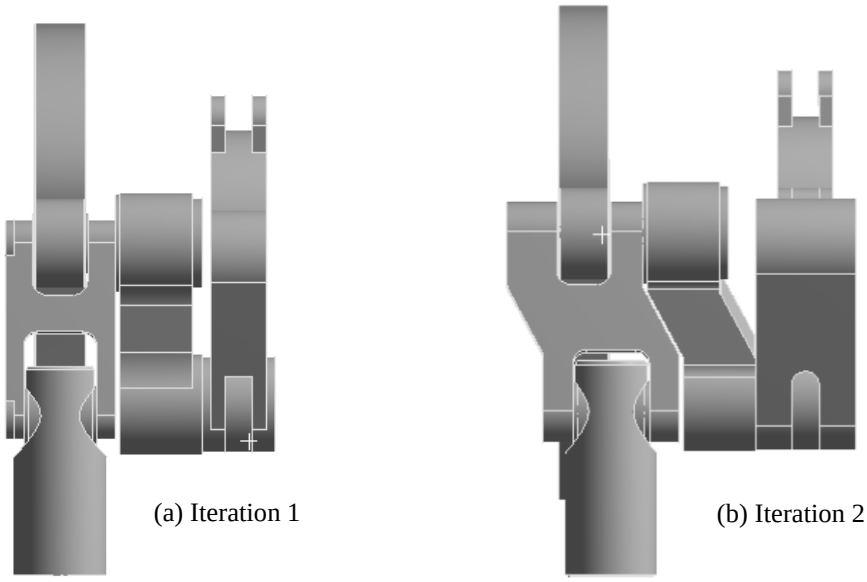

(a) Iteration 1 (b) Iteration 2

Figure 4.32 Top view of iteration 1 and iteration 2 cam pump assembly designs

Figure 4.32 also shows that the thickness of the pivot link is increased in iteration 2 to increase bending stiffness. The rocker and connecting rod in iteration 2 have a 'Z' shape in order to accommodate the movement of piston towards the adjustment mechanism.

Figure 4.33 and Figure 4.34 shows how the design of the connecting rod and rocker are modified from iteration 1 to 2.

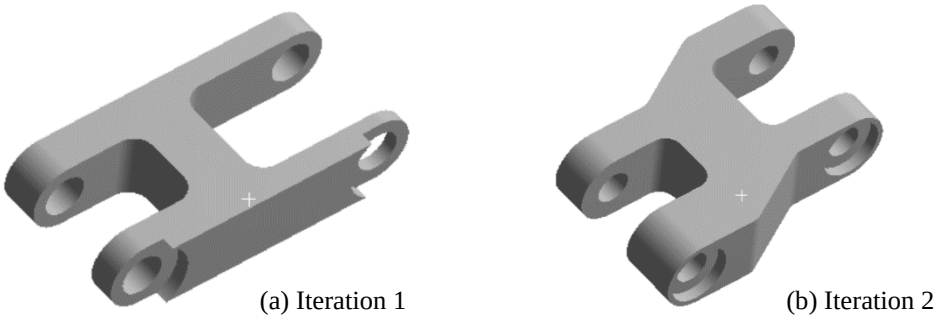

(a) Iteration 1 (b) Iteration 2

Figure 4.33 Comparison of connecting rod shape in iteration 1 and 2

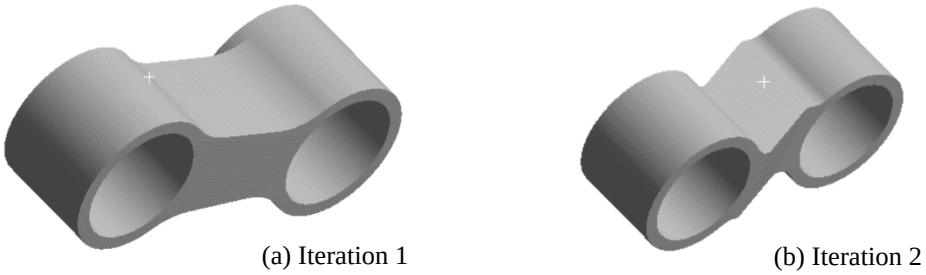

(a) Iteration 1 (b) Iteration 2

Figure 4.34 Comparison of rocker shape in iteration 1 and 2

A 4.6% decrease in the maximum overall deformation in the assembly was observed in iteration 2 when compared to iteration 1 (64.5% reduction compared to initial design), as shown in Figure 4.35. It can also be observed that the deformation of adjustment mechanism in iteration 2 is negligible. Further, a 19.7% reduction in the axial piston deformation is observed in iteration 2 compared to iteration 1 (66.4% reduction compared to the initial design). The maximum stress observed in the assembly also decreased in iteration 2 compared to iteration 1, as shown in Figure 4.36.

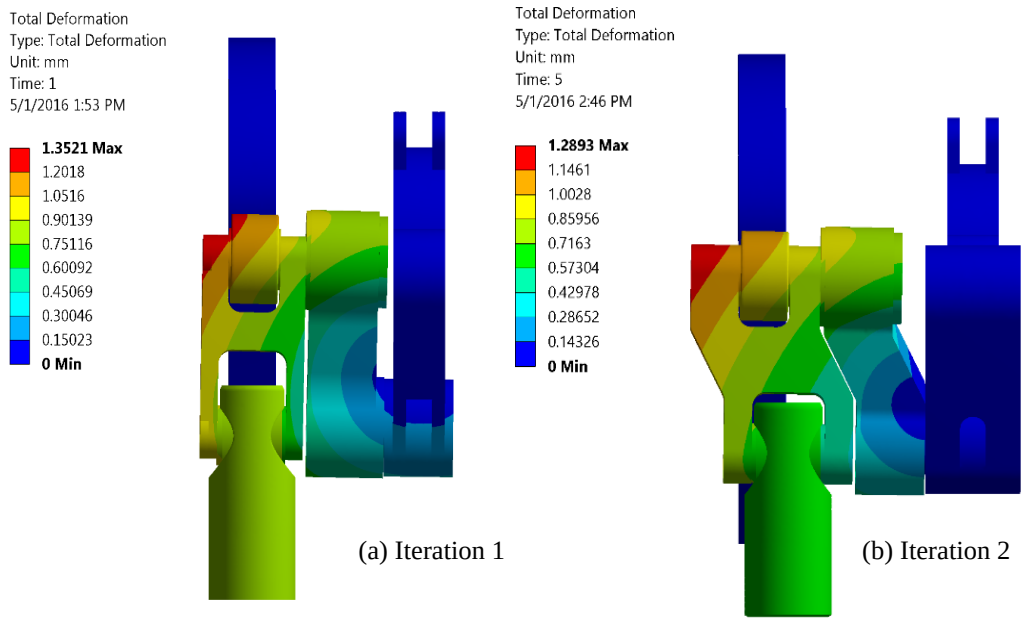

Figure 4.35 Comparison of cam pump assembly deformation contour plot in iteration 1 and 2

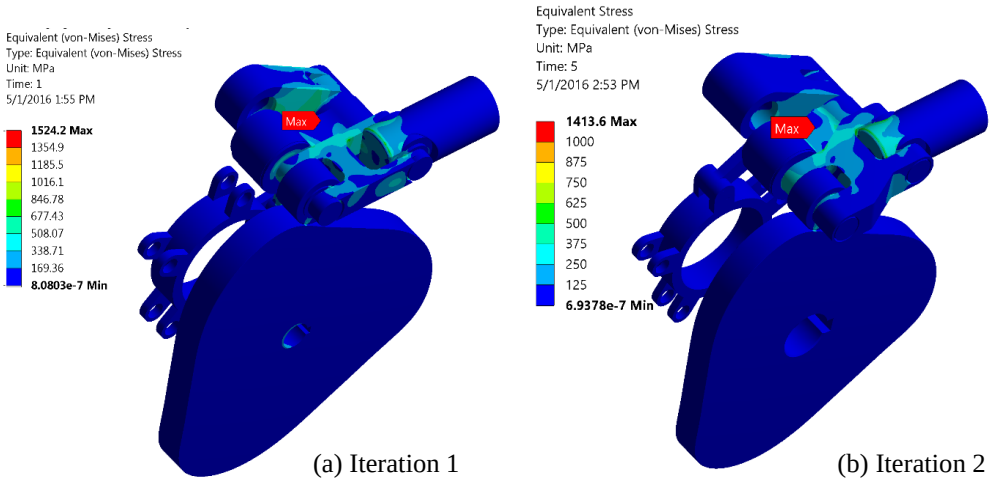

Figure 4.36 Comparison of cam pump assembly stress contour plot in iteration 1 and 2

Figure 4.37compares the stress contours of the rocker in iterations 1 and 2. The maximum stress induced in the rocker is considerably increased in iteration 2. The 'Z' shape design led to a high stress concentration zone in the rocker near the ground pivot where it bends about the pivot link. Figure 4.38 shows that the maximum stress in the connecting rod decreased significantly in iteration 2.

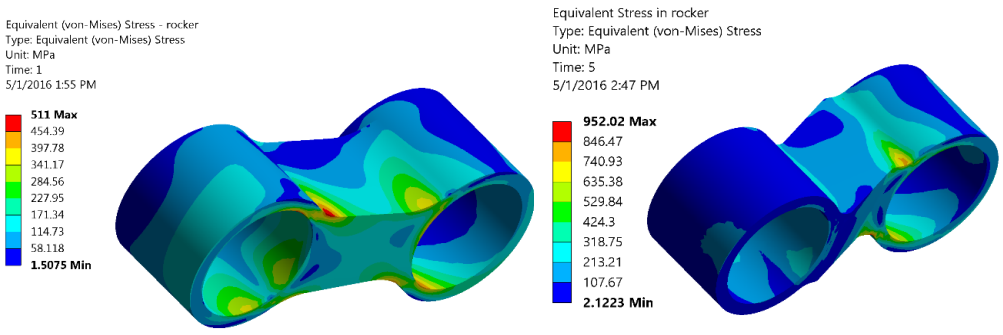

(a) Iteration 1 (b) Iteration 2

Figure 4.37 Comparison of rocker stress contour plot in iteration 1 and 2

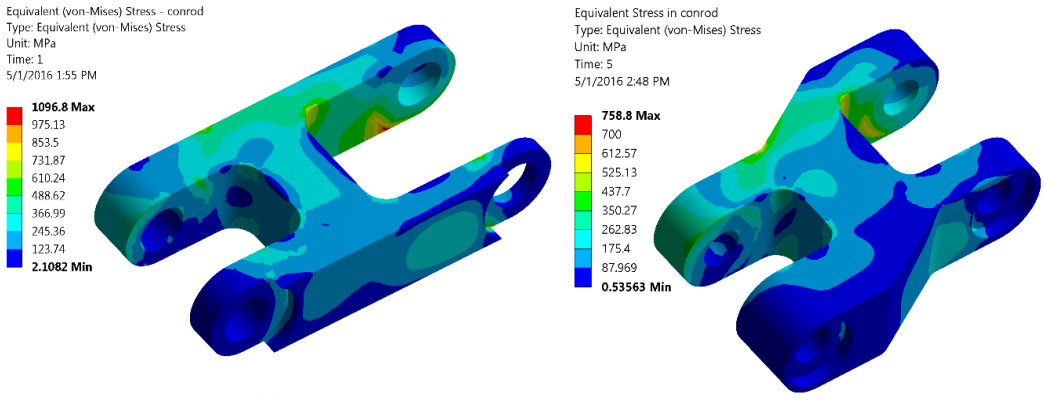

(a) Iteration 1 (b) Iteration 2

Figure 4.38 Comparison of connecting rod stress contour plot in iteration 1 and 2

From iteration 2, it can be observed that moving the piston towards the adjustment mechanism reduced the axial piston displacement and maximum assembly deformation. But, the stress induced in the rocker and the connecting rod are still above 700 MPa because of 'Z' shape. The stress at the cam-roller contact is also above 1 GPa. These issues are addressed in iteration 3, presented in next section.

4.3.4 Iteration 3

It was observed in the previous design iterations that the deformation and stress induced in the adjustment mechanism was low compared to the other components of the assembly.

Hence in iteration 3, the thickness of the pivot link was reduced towards the side facing the roller, as shown in Figure 4.39. This allowed the rocker to be moved into the available extra space between it and pivot link, thereby reducing the distance between the ground pivot and the piston axis. This reduced the out-of-plane moment on the assembly. Further, the cam and the piston were moved back in line with each other, with piston being still close to the adjustment mechanism. This iteration eliminated the 'Z' shape from the connecting rod, as shown in Figure 4.40 and Figure 4.41. Many chamfers and fillets were included in the rocker and connecting rod to minimize stress concentrations.

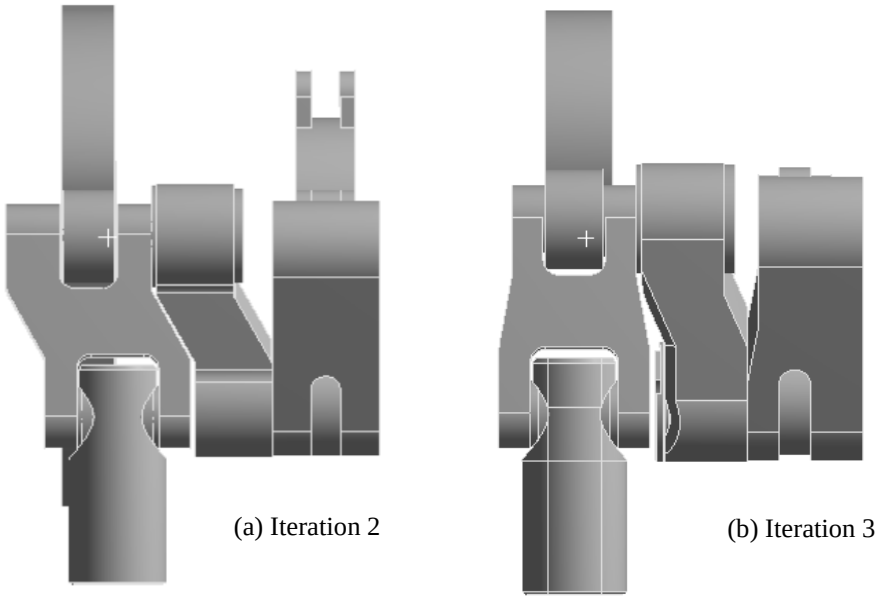

(a) Iteration 2 (b) Iteration 3

Figure 4.39 Top view of iteration 2 and iteration 3 cam pump assembly designs

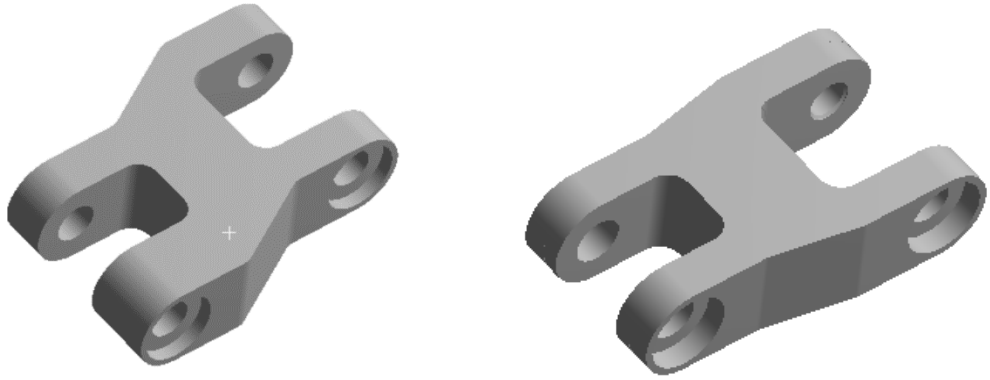

(a) Iteration 2 (b) Iteration 3

Figure 4.40 Comparison of connecting rod shape in iteration 2 and 3

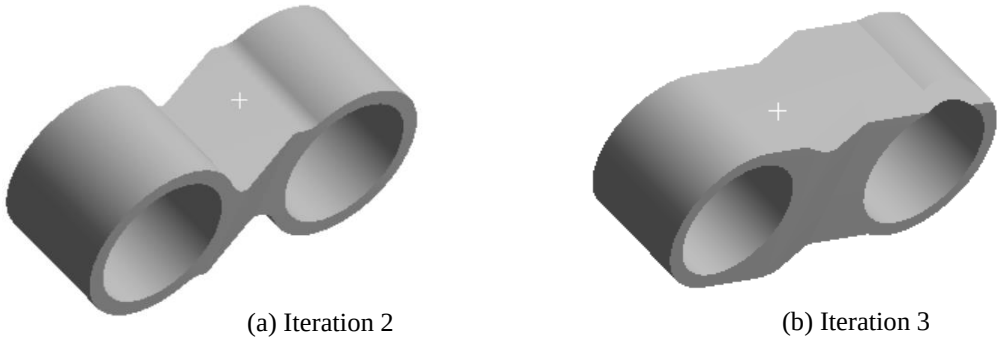

(a) Iteration 2 (b) Iteration 3

Figure 4.41 Comparison of rocker shape in iteration 2 and 3

A 35.2% reduction in the maximum deformation of assembly was observed in iteration 3 when compared to iteration 2 (77% reduction compared to initial design), as shown in Figure 4.42. This was mainly because of the reduced distance between piston and adjustment mechanism. Further, the axial piston displacement was reduced by 23% (74% compared to initial design). However, the maximum stress in the assembly, as shown in Figure 4.43, is on the same order as the stress observed in iteration 2. A circular cam was used in this iteration for computational efficiency. It is kinematically equivalent to the original cam as the distance between the center of curvature and the curvature surface where roller-follower sliding occurs is the same.

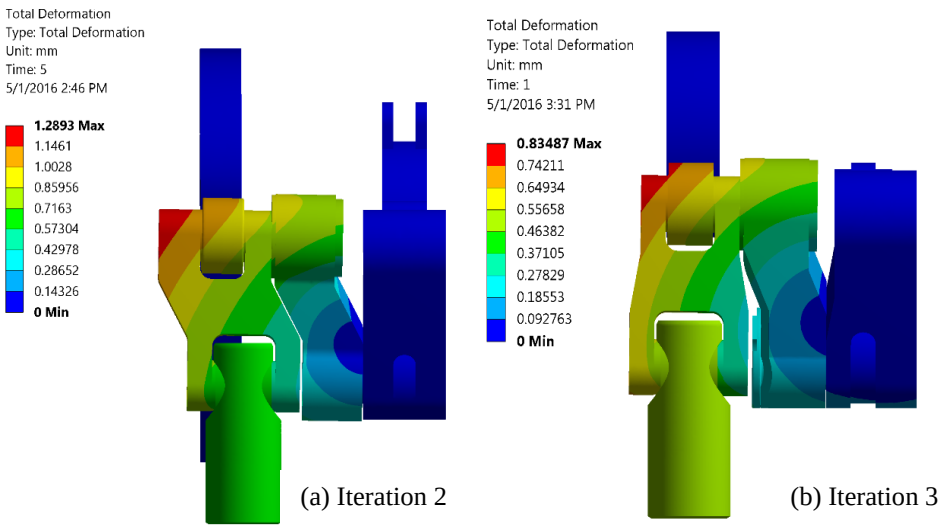

Figure 4.42 Comparison of cam pump assembly deformation contour plot in iteration 2 and 3

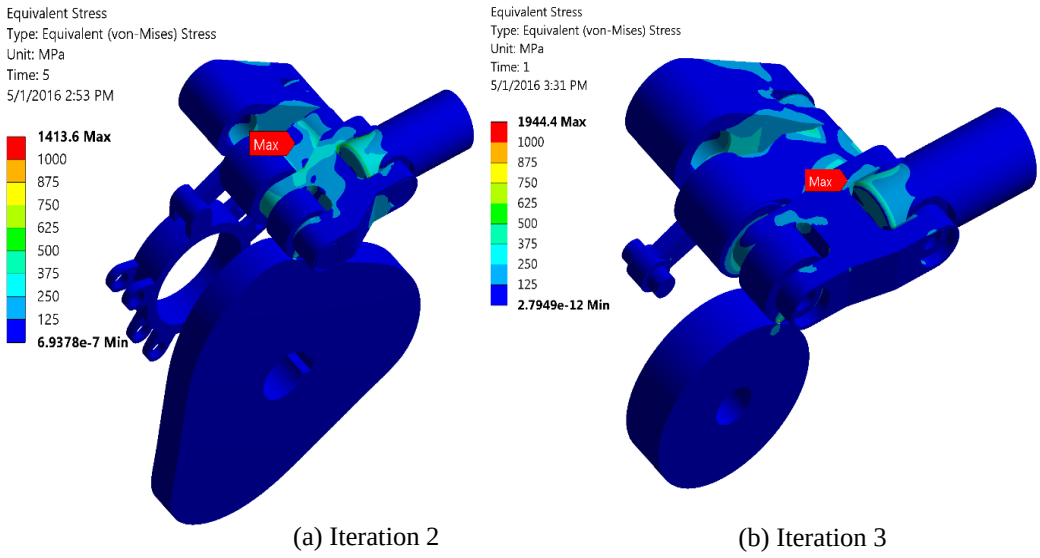

Figure 4.43 Comparison of cam pump assembly stress contour plot in iteration 2 and 3

Figure 4.44 and Figure 4.45 show that the overall stress in the rocker and the connecting rod are reduced when compared to the iteration 2 design, yet high stress concentration exist. Design requirement of making sure that the links do not fail in the worst case loading scenario was met, as observed in the figure. Stress induced in the links in iteration 3 is less than the yield strength of alloy steel, ignoring the small stress concentration zones. These

stress concentrations were further minimized by including fillets/chamfers during the manufacturing stage. Zero axial piston deformation cannot be achieved in reality, however, these design iterations aided in reducing the deformation to 0.48mm when the maximum possible load acts on the piston.

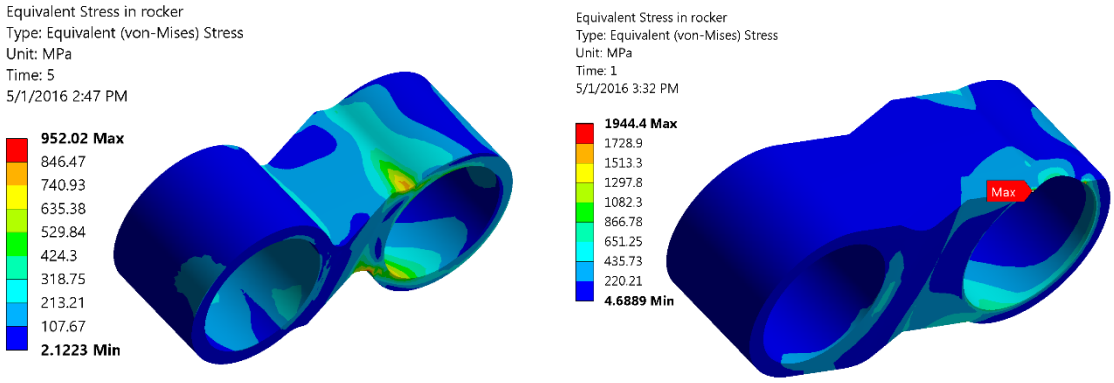

(a) Iteration 2 (b) Iteration 3

Figure 4.44 Comparison of rocker stress contour plot in iteration 2 and 3

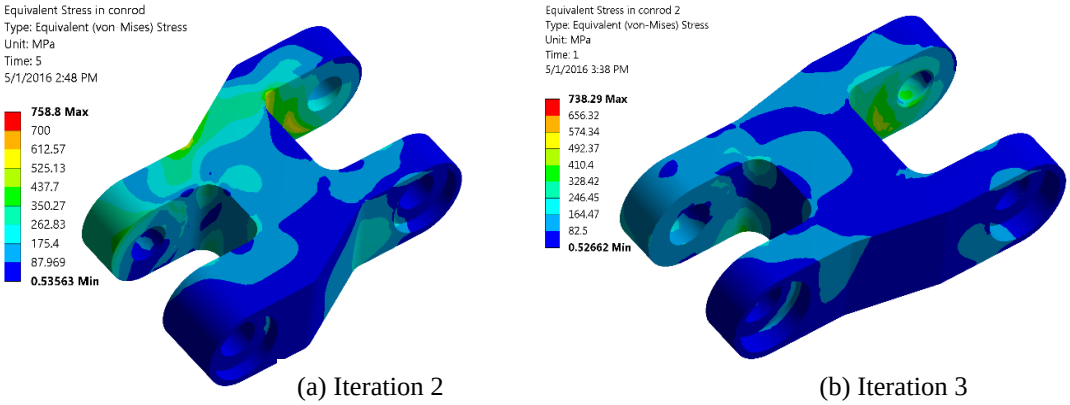

(a) Iteration 2 (b) Iteration 3

Figure 4.45 Comparison of rocker stress contour plot in iteration 2 and 3

4.4 Conclusion

In this chapter, the working principle of the cam driven variable displacement linkage pump was introduced and the need for improving the stiffness of its linkage assembly was presented. A method of using multi-body finite element analysis as a design tool to drive the design process was discussed. FEA of the initial linkage assembly design, referred to as the base model, was presented as an example to show the systematic approach to set up a multi-body simulation problem.

CAD models of low head socket cap screws and the full complement needle roller bearings were simplified for analysis to reduce the computational time. A simplified bearing model was developed, where the needle rollers were replaced by a bushing with equivalent elastic properties to the rollers. This model was computationally inexpensive, numerically stable and required less time to setup. Local and global mesh controls and boundary and loading conditions were also discussed. A combination of linear and nonlinear contacts were used at various joints in order to obtain realistic simulation results without any convergence issues. Different contact types were compared and their influence on the analysis results were discussed. It was observed that using linear contacts under predicted the overall deformation of the assembly in cases where surfaces have large relative motion or gaps that change in size as the load is applied.

FEA of the base model showed the axial piston displacement under load to be greater than 1.9mm and the stress in the rocker and connecting rod to be greater than 1GPa. In order to address these design deficiencies, three significant steps along the path of the numerous design iterations using FEA were presented. The design of rocker, connecting rod and the distance between the piston and the ground pivot were the major parameters that influenced the stiffness of linkage mechanism assembly. By the end of the third iteration, stress concentration in the rocker and the connecting rod were reduced to under 800MPa. A 74% reduction in the axial piston displacement and a 77% reduction in the overall assembly deformation was observed, which has the potential to improve the volumetric efficiency and minimize the frictional losses at various joints of the assembly. These results clearly show the advantage of using FEA to drive the complex design process within limited time. It should be noted that this chapter considered the analysis and design of parts subjected to static loading and did not take the fatigue into account in calculating the material strength limit.

5. Conclusions

5.1 Thesis Review and Conclusions

A large percentage of energy losses in fluid power systems are due to inefficient flow control methods. While conventional variable displacement pumps offer a better method of controlling the speed of actuator over metering valves, most of them are inefficient at low displacements. The variable displacement linkage pump architecture developed recently at the University of Minnesota, which is driven by an adjustable six-bar linkage, shows great promise to achieve high efficiency across the full displacement range. A primary reason for the high efficiency is the use of rolling element bearing in revolute joints instead of the hydrodynamic planar joints used in conventional pumps. Even though high mechanical efficiency was achieved in first two generation designs, volumetric efficiency of the linkage pumps was limited by their design and poorly performing check valves. Thus, a part of this thesis focused on the design and analysis of a new generation VDLP addressing issues of the previous pump prototypes. The primary findings of this investigation include:

- The single shear arrangement of links in the second generation VDLP resulted in out-of-plane deflection of coupler link, reducing the piston displacement. Hence, links were duplicated in the new generation design to place the joints in double-shear to cancel the moments acting on the coupler. Experiments showed that the volumetric efficiency improved by an average of 10% over the previous generation pump.

- FEA was conducted on the links and necessary design changes were made to ensure that the linkage mechanism was rigid enough to withstand the loads. No visible deflection was observed in the physical pump, which helped in improving the efficiency of the pump.
- The adjustment mechanism assembly, which is used to change the piston displacement, was designed in such a way that the control arms handle most of the forces and the rectangular cross beam bolted to the bottom of the control arms handles most of the moments from rockers. This reduced the deformation of adjustable ground pivot along the arc. FEA results were validated by comparing the numerical results of the rotational deflection of the adjustment mechanism assembly about its ground pivot with the results obtained through experiments.
- The experiments showed that the overall efficiency of the pump was around 80% above 20% displacement with volumetric efficiency being 90% at all conditions. This shows a significant improvement in the performance of new generation pump over the previous generation pumps.
- The new generation pump is capable of working at 3500 psi with a displacement of 10cc/rev. The size of the pump was reduced compared to the previous generation designs, advancing the pump towards commercialization.

Chapter 3 presented an investigation of improving the pressure withstanding capability of Rolling Diaphragm Seals (RDS). As circumferential fibers don’t have a greater role in withstanding the load, parameters that could improve the strength of RDS in axial direction

were explored by conducting extensive parametric FEA studies. As convolution is the highest stressed section of RDS and represents the location of possible blowout failure, only the convolution portion was analyzed. The primary factors of interest that were identified were number of fibers, fiber diameter, fiber pattern and young's modulus of elastomer. A parametric study was carried out with 45, 60, 90, 120, and 180 fibers and with fiber diameters of 0.1mm, 0.3mm, 0.5mm. The following conclusions can be drawn from the study:

- Increasing the fiber diameter and number of fibers reduces the deformation of elastomer and the stress induced in fiber, thereby increasing the pressure capability of RDS.
- The fiber diameter was found to be an important parameter that effects the pressure capability more than the number of fibers.
- Analysis showed that a Kevlar reinforced neoprene diaphragm seal (0.5mm fiber diameter and 180 fibers) would be able to withstand a maximum pressure of 8.7 MPa, before the elastomer fails.
- From the analysis results, it was observed that RDS cannot withstand pressures more than 9MPa even after using Kevlar/Neoprene, increasing the fiber diameter and number of fibers. Modifying the fiber pattern seems to be a solution to slightly improve this maximum limit.

Chapter 4 presented a systematic approach of using multi-body FEA to drive the design process, using a cam driven VDLP as a case study. The focus of the design was on

improving the stiffness of the linkage assembly to improve the volumetric efficiency. The primary findings of this study include:

- The CAD models of low head socket cap screws and the full complement needle roller bearings were simplified for analysis to reduce the computational time. A simplified bearing model was developed, where the needle rollers were replaced by a bushing with equivalent elastic properties to the rollers. This model was computationally inexpensive, numerically stable and required less time to setup. Local and global mesh controls and boundary and loading conditions were also discussed. A combination of linear and nonlinear contacts were used at various joints in order to obtain realistic simulation results without any convergence issues. Different contact types were compared and their influence on the results were discussed. It was observed that using linear contacts under predicted the overall deformation of the assembly in cases where surfaces have large relative motion or gaps that change in size as the load is applied.
- FEA of the base model showed that the axial piston displacement when the piston was under pressure was greater than 1.9mm and the stress in the rocker and connecting rod to be greater than 1GPa. In order to address these design deficiencies, three significant steps along the path of the numerous design iterations using FEA were presented. The design of rocker, connecting rod and the distance between the piston and the ground pivot were the major parameters that influenced the stiffness of linkage mechanism assembly. A 74% reduction in the axial piston displacement and a 77% reduction in the overall assembly deformation was

observed, which has the potential to improve the volumetric efficiency and minimize the frictional losses at various joints of the assembly. These results clearly show the advantage of using FEA to drive the complex design process within a limited time.

To summarize, in this thesis, a new generation variable displacement pump is presented, which is designed to improve the volumetric efficiency, reduce the size and advance it towards commercialization. The finite element analysis results were validated by comparing the rotational deflection of the adjustment mechanism assembly obtained through simulations with that of those from experimental results. Also, a preliminary study is presented on analyzing the behavior of rolling diaphragms under various conditions using finite element analysis, providing an insight into the possibility of modifying the design of the seal to improve the pressure capability. Further, this thesis also describes the structural analysis that supports the design of a cam driven radial configuration of the variable linkage pump. A systematic approach of using FEA to drive the design process, identifying proper contact interfaces, and a simplified bearing model has been presented, which can be used for designing next generation linkage pumps and for any similar applications.

5.2 Recommendations for Future Work

Future work on the crankshaft driven variable displacement pump could investigate different design solutions to redesign the linkage mechanism in order to minimize the weight. The split crankshaft design, efficient in terms of ease of manufacturing, consumes a lot of time to assemble, as the individual crankpins have to be aligned properly to prevent shaft wobble. It is also the weakest point in the entire design, as the subassembly entirely depends on the split shaft collars to hold the crankpins together. A better design in terms of ease of manufacturing and assembly would negate the odds of pump failure, reduce the cost and time taken for the assembly.

There are quite a few areas of research that would augment the analysis work presented in this thesis on rolling diaphragm seals. The presented finite element analysis approach does not consider any pre-strain in the material at the outer radius of the diaphragm. ANSYS Parametric Design Language may be used to incorporate pre-strain in the elements to get much more realistic results. The FEA approach presented here can be used to explore the effect of changing the thickness and convolution width of RDS. An attempt can be made to obtain analytical relationships to calculate deformation and stress, validate the numerical results and then use that to efficiently narrow down the parametric grid search, as running FEA parametric simulations consumes a lot of computational time.

The approach presented in the thesis to use FEA to drive the design iterations of the cam drive variable displacement pump can be extended to designing any other new generation pumps

efficiently and could be also used for similar applications. A general observation made during the simulations was that the piston deflection could be further reduced by using a double shear configuration instead of a single shear. It is recommended that the future designs use a double shear arrangement to reduce the piston deflection. Analytical expressions for obtaining the equivalent young's modulus of bearing can be developed, that would speed up the process of simplifying the bearing model, contrary to the time taking iterative FEA approach presented in the thesis.

Bibliography

[1]. “2015 annual report on the U.S. fluid power industry”, National Fluid Power Association

[2]. Love, L., Lanke, E., and Alles, P., 2012, "Estimating the Impact (Energy, Emissions and Economics) of the US Fluid Power Industry," Oak Ridge National Laboratory (ORNL)

[3]. Wilhelm, S., “Modeling, Analysis, and Experimental Investigation of a Variable Displacement Linkage Pump”, PhD thesis, University of Minnesota, 2015, http://hdl.handle.net/11299/175371

[4]. “Industrial hydraulics manual”, Eaton Hydraulic Training Services, 5th edition

[5]. McCandlish, D. and R.E. Dorey, "The Mathematical Modelling of Hydrostatic Pumps and Motors." Proceedings of the Institution of Mechanical Engineers, Vol. 198, 1984, pp. 165-174.

[6]. McCandlish, D. and R. Dorey. "Steady State Losses in Hydrostatic Pumps and Motors," 1981, pp.133-144.

[7]. Rodney B. Erickson, “Quick and easy guide to hydraulic pump technology and selection”

[8]. Manring, N. D., 2003, “Valve-Plate Design for an Axial Piston Pump Operating at Low Displacements,” ASME J. Mech. Des., 125(1), pp. 200–205.

[9]. Wang, S., 2012, “Improving the Volumetric Efficiency of the Axial Piston Pump,” ASME J. Mech. Des., 134, p. 111001.

[10]. Seeniraj, G. K., and Ivantysynova, M., “Impact of Valve Plate Design on Noise, Volumetric Efficiency and Control Effort in an Axial Piston Pump,” ASME 2006 International Mechanical Engineering Congress and Exposition, Fluid Power Systems and Technology, Chicago, IL, ASME Paper No. IMECE2006- 15001, Nov. 5–10, New York, pp. 77–84.

[11]. Wieczorek, U., and Ivantysynova, M., 2002, "Computer aided optimization of bearing and sealing gaps in hydrostatic machines- the simulation tool CASPAR," International Journal of Fluid Power, 3(1), pp. 7-20.

[12]. Wilhelm, S., and Van de Ven, J. D., 2011, “Synthesis of a Variable Displacement Linkage for a Hydraulic Transformer,” Proceedings of the ASME 2011 International Design Engineering Technical Conferences andComputers and Information in Engineering Conference, IDETC/CIE 2011, August 28–31, 2011, Washington, DC, ASME, New York, p. 8.

[13]. Wilhelm, S., and Van de Ven, J. D., “Design and Testing of an Adjustable Linkage for a Variable Displacement Pump” Journal of Mechanisms and Robotic of the ASME, NOVEMBER 2013, Vol. 5 / 041008-1

[14]. Wilhelm, S., and Van de Ven, J. D., “Adjustable Linkage Pump: Efficiency Modeling and Experimental Validation” J. Mechanisms Robotics 7(3), 031013

[15]. Wilhelm, S. R., and Van de Ven, J. D., 2014, "Design of a Variable Displacement Triplex Pump," International Fluid Power Exposition, Las Vegas, NV.

[16]. Wilhelm, S., and Van de Ven, J. D., “Efficiency Testing of an Adjustable Linkage Triplex Pump” , Proceedings of the ASME/BATH 2014 Symposium on Fluid Power and Motion Control FPMC2014, September 10-12, 2014
[17]. Wilhelm, S., and Van de Ven, J. D., “A linkage driven variable displacement pump”, Fluid Power Innovations and Research Conference presentations, Chicago, October 2015
[18]. Wilhelm, S., and Van de Ven, J. D., “A cam driven variable displacement linkage pump”, Fluid Power Innovations and Research Conference, Minneapolis, October 2016
[19]. Emil Claesson, “Modelling of roller bearings in Abaqus”, Master’s thesis, Chalmers University of Technology
[20]. Houpert, L., “A uniform analytical approach for ball and roller bearings calculations”, Journal of Tribology, 119(4), 851-858, 1997
[21]. Brown N.P., Heywood N.I., “Slurry Handling: Design of solid-liquid systems”, Elsevier Handling and Processing of Solids Series), 1991, 1st Edition
[22]. Haynes, J. M., "Axial piston pump leakage modelling and measurement," PhD, Cardiff University, 2007
[23]. White, J.F.C. and Seal, M.E.J., “Seasand handling and pumping at Cockburn Cement”, Proc. Hydrotransport 8, Paper A5 pp. 63-76, BHRA, Cranfield, 1982
[24]. Robert K. Flitney, “Seals and Sealing Handbook”, Elsevier Science; 5 edition, 2007
[25]. Frank R. Spellman., “Handbook for Waterworks Operator Certification: Intermediate Level”, Volume 2, CRC Press, 2000
[26]. Doyle B., Zalud T., October 1999, “Rolling Diaphragm Seals Stay Strong Under Pressure”, Machine Design;10/07/99, Vol. 71 Issue 19, p83
[27]. Marsh Bellofram., 2012, “Diaphragm Design Manual”
[28]. Dia.Com Corporation., 2008, “Diaphragm Design Guidebook”
[29]. J A Rietdijk., H C J Van Beukering., H H M Van der Aa., 1965, “A Positive rod or piston seal for large pressure differences”, Philips Technical review, vol 26
[30]. Larry D. Peel., 1998, “Fabrication And Mechanics of Fiber-Reinforced Elastomers,” Ph.D. thesis, Brigham Young University, http://users.tamuk.edu/kfldp00/research/papers/dissertation.pdf
[31]. Karthic Vuppaladhadyam Rathnam., Larry D. Peel., 2004, “Impact Resistant Fiber Reinforced Elastomer Composite Materials", SAMPE, Long Beach, CA
[32]. P. Maeder-York, et al., 2014, “Biologically Inspired Soft Robot for Thumb Rehabilitation,” in Proceedings of Design of Medical Devices Conference, Minneapolis, MN
[33]. Kevin C. Galloway., Panagiotis Polygerinos., Conor J. Walsh., Robert J. Wood, 2013, “Mechanically programmable bend radius for fiber-reinforced soft actuators”, 16th International Conference on Advanced Robotics
[34]. Koichi Suzumori., 1996, “Elastic materials producing compliant robots”, Robotics and Autonomous Systems, Volume 18, Issues 1–2, Pages 135–140.
[35]. ANSYS Inc., 2013, “ANSYS 13.0 Mechanical User’s Guide”, pages 414-417

[36]. Books Llc., 2010, "Elastomers: Rubber Properties, Natural Rubber, Viscoelasticity, Hyperelastic Material, Synthetic Rubber, Latex Allergy, Carbon Black"
[37]. Granta Design, 2015, "CES EduPack database"
[38]. Nam-Ho Kim, 2015, "Introduction to Nonlinear Finite Element Analysis", Springer US
[39]. Emil Claesson., 2014, "Modelling of roller bearings in Abaqus", M.S. Thesis, Chalmers university of technology
[40]. Warren C Young., Richard C Budynas., seventh edition, 2002, "Roark's formulas for stress and strain", pg 703, McGraw-Hill, New York, United States of America
[41]. "ANSYS Meshing User's Guide", ANSYS Inc, Version 16.1
[42]. "ANSYS Mechanical User's Guide", ANSYS Inc, Version 16.1
[43]. Tedric A. Harris, "Rolling Bearing Analysis", John Wiley and Sons, 3rd edition, 1991
[44]. Houpert, L., "A uniform analytical approach for ball and roller bearings calculations", Journal of Tribology, 119(4), 851-858, 1997
[45]. http://www.umich.edu/~bme332/ch3strain/bme332straindef.htm
[46]. http://www.digitaleng.news/de/verification-vs-validation/
[47]. "Crankshaft Assembly" Provisional Patent Application: 14/689,269, Filed April 17, 2015, Claims: Split crankshaft

Appendix A. Tolerance Stack up Analysis of the third generation prototype

1. Length of Crankshaft

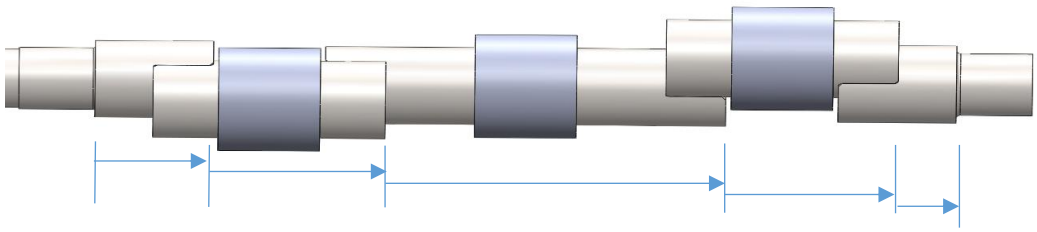

*All dimensions are in mm.

Description/Part	**Mean**	**Tolerance**
Tolerance of primary datum in input shaft		0.025
Input Shaft	30	0.025
Second Link	43	0.025
Third Link	87	0.025
Second Link	43	0.025
First Link	15	0.025
Length of crankshaft	218	0.15
	Maximum	**Minimum**
Extreme Limits	218.15	217.85

2. Verifying if AS2542 washers fit on either sides of crankpin raceways

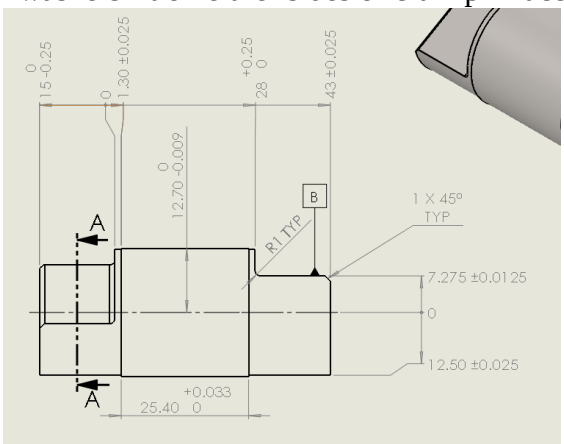

Nominal Dimension/Description (refer to the figure above)	Minimum	Maximum	Tolerance
1.3	1.275	1.325	0.025
25.4	25.4	25.433	0,+0.033
Extreme limits	26.675	26.758	
Total length of crank throw	28	28.25	0,+0.25

Hence, the length available for washer on the right side of the raceway in the figure shown above is
Minimum: 28-26.758=1.242 mm
Maximum: 28.25-26.675=1.575 mm
Width of the washer on left side of the crankpin should be less than 1.275 mm

3. Verifying if connecting rod and coupler can fit inside the double shear pin, rocker assembly

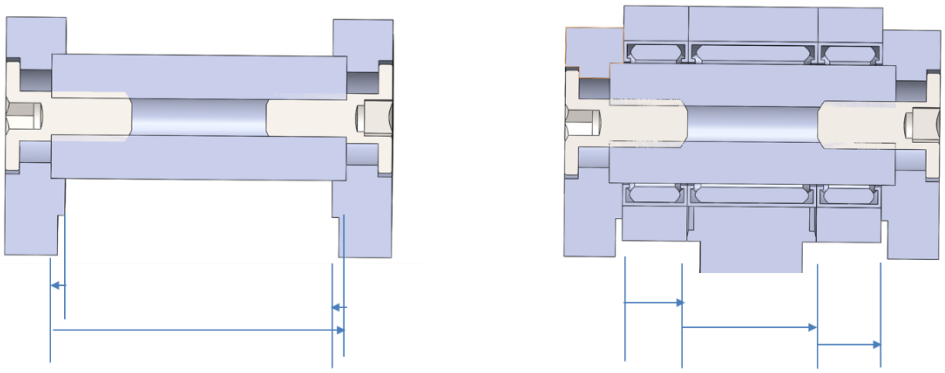

Description	Mean	Tolerance
depth in rocker	-2	0,-0.025
Double shear pin	42.1875	0,0.025
depth in rocker	-2	0,-0.025
space btwn rockers	38.1875	
	Minimum	Maximum
Gap	38.1875	38.2625

Description	Mean	Minimum	Maximum
width-con rod	9.525	0	0.025
space btwn conrods	19.05	0.025	0.0375
width-con rod	9.525	0	0.025
length of all the individual links	38.1	0.025	0.0875
	Maximum	**Minimum**	
Length	38.1875	38.125	

Therefore the minimum gap between connecting rod and the rocker = 38.1875-38.1875=0
Similarly, maximum gap= 38.2625-38.125 = 0.1375
This results in a close running fit between the rocker and connecting rod, which is essential for smooth running of linkage assembly.
4. Minimum amount of clearance between connecting rod and piston bearing mount

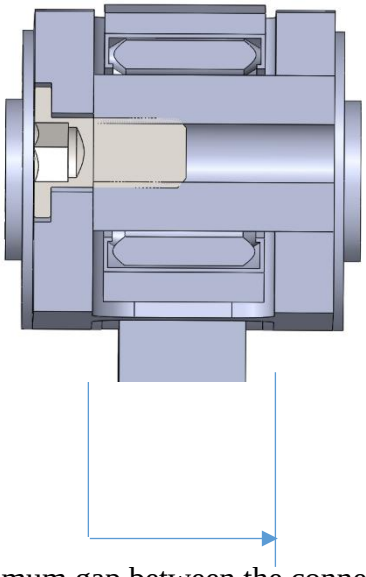

Minimum gap between the connecting rod=21.285
Maximum width of the piston bearing mount=19.21
Therefore, the minimum clearance we have here= 21.285-19.21=2.075

5. Verifying if the maximum width of the linkage assembly fits well between the control arms of adjustment mechanism assembly

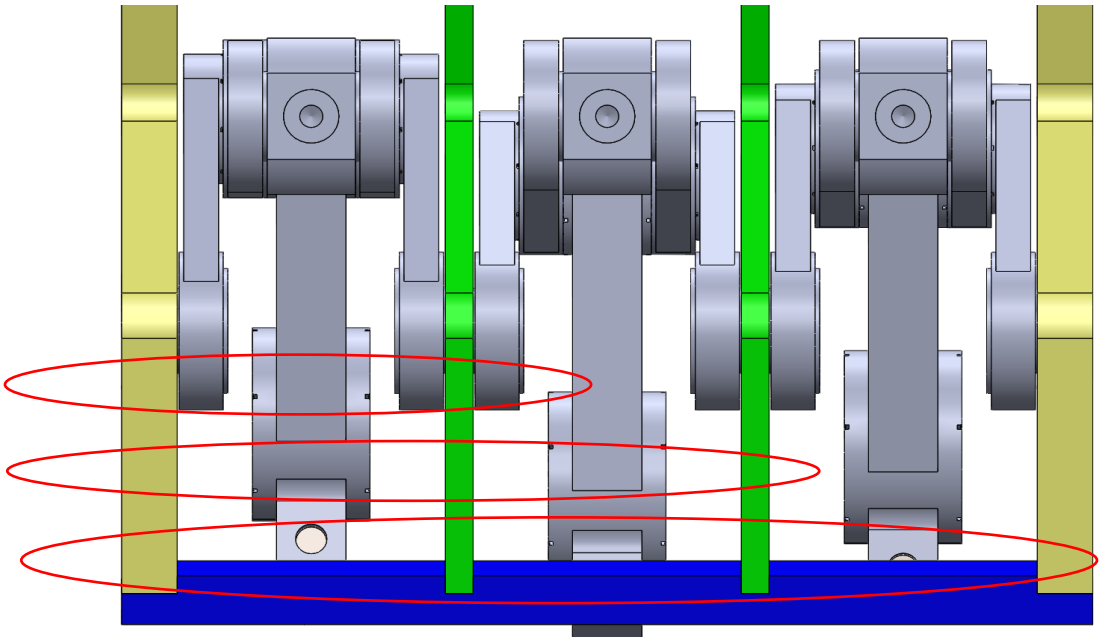

Maximum width of a single linkage can be found using the dimensions indicated in following figure

Description	**Mean**	**Tolerance**	**Minimum**	**Maximum**
rocker-width-bottom	9.525	0,0.025	9.525	9.55
rocker-depth-top	-2	0,-0.025	-2	-1.975
double shear pin	42.1875	0,0.025	42.1875	42.2125
rocker-depth-top	-2	0,-0.025	-2	-1.975
rocker-width-bottom	9.525	0,0.025	9.525	9.55
length	57.2375		57.2375	57.3625

Description	Mean	Tolerance	Minimum	Maximum
Width of rocker (bottom)	9.525	0,0.025	9.525	9.55
Depth in rocker (top)	-2	0,-0.025	-2	-1.975
Double shear pin	42.1875	0,0.025	42.1875	42.2125
Depth in rocker (top)	-2	0,-0.025	-2	-1.975
Width of rocker (bottom)	9.525	0,0.025	9.525	9.55
length	57.2375		57.2375	57.3625

Therefore the maximum width of a single linkage assembly=57.3625
Using the above numerical value, it can now be verified if the linkage assembly would fit between the control arms. However, separate stack up analysis has to be carried out on the adjustment assembly before move any further.
Following drawing of the rectangular cross beam at the bottom is provided to give a broad picture of what calculations are done here. It should be noted that the center to center distance of the linkage assemblies is 65mm.

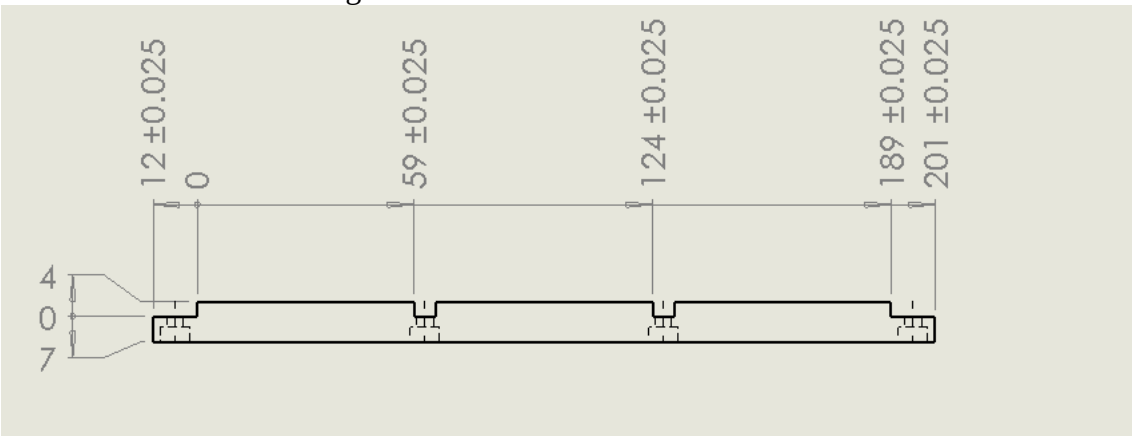

Description	Min	Max
Distance btn control arm and first ground pivot	58.975	59.025
Distance btn 2 ground pivots	58.946	59.058
Distance btn 2nd g.pivot and last control arm	58.946	59.058

The values provided in the table above can be calculated from the drawing of the rectangular beam provided above.
1st linkage assembly:

- Centerline of the 1st linkage assembly is taken as reference to start with (see the figure shown below)

Maximum Distance of center of 2nd linkage assembly from 1st (reference) = 43.025+23.325+ (25.474-25.4/2)-14 [please refer to the individual parts of crankshaft to understand how these values came up) = 65.124

However reference itself has a maximum tolerance stack up of 0.05, which makes the maximum distance of center of 2nd linkage assembly= 65.124+0.05=65.174

• Similarly minimum distance of center of 2nd linkage assembly from 1st (reference) = 42.975+23.275+(25.425-(25.425/2))-14+0.05=65.0125

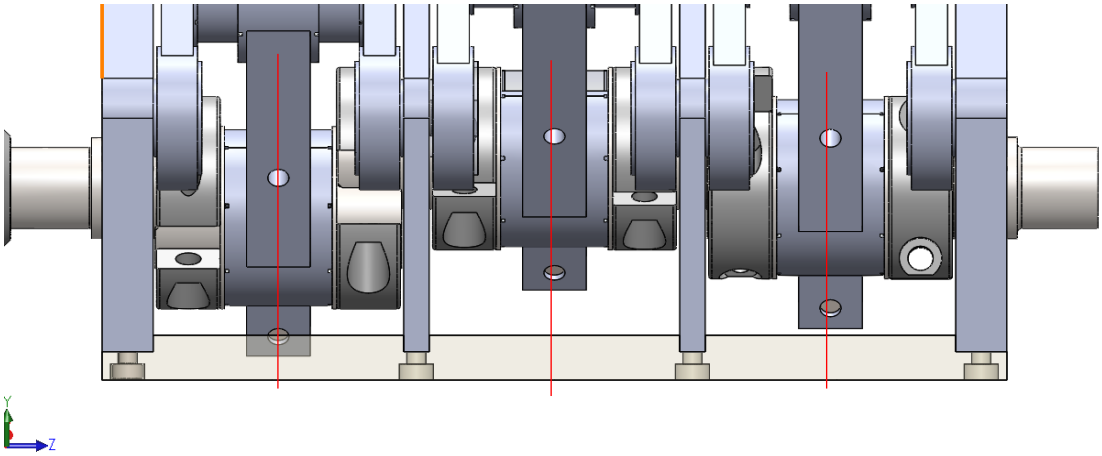

• Maximum Distance of center of 3rd linkage assembly from 1st (reference) = 43.025+87.025+1.325+ (25.474-25.4/2)-14 [please refer to the individual parts of crankshaft to understand how these values came up)

=130.149

But reference itself has a maximum stack up of 0.05, which makes the maximum distance of center of 2nd linkage assembly= 130.149+0.05=130.199

Similarly minimum distance of center of 3rd linkage assembly from 1st (reference) = 42.975+86.975+1.275+(25.425-(25.425/2))-14+0.05=129.9875

<u>2nd linkage assembly:</u>

- **Maximum position of center of coupler:**

Numerical value for Maximum position of rocker on right side should be less than the numerical value of position of 2nd ground pivot
65.174+ (57.3625/2) +29.5125=123.36775 < 123.975(actual position of left side of 2nd ground pivot)
Numerical value for Minimum position of rocker on left side should be greater than the numerical value of position of 1st ground pivot
65.174 – (57.225/2) + 29.5125 = 66.00525 > 65.029 (actual position of right side of 1st ground pivot)
Hence, linkage assembly won't interfere with ground pivots and control arms.

- **Minimum position of center of coupler**:

Numerical value for Maximum position of rocker on right side should be less than the numerical value of position of 2nd ground pivot
65.01+ (57.3625/2) +29.5125=123.20375 < 123.975(actual position of left side of 2nd ground pivot)
Numerical value for Minimum position of rocker on left side should be greater than the numerical value of position of 1st ground pivot
65.01 – (57.3625/2) + 29.5125 = 65.84125 > 65.029 (actual position of right side of 1st ground pivot)
Hence, linkage assembly won't interfere with ground pivots and control arms.
3rd linkage assembly:

- **Maximum position of center of coupler:**

Numerical value for Maximum position of rocker on right side should be less than the numerical value of position of control arm on the right end
130.199 + 57.3625/2 + 29.5125 =188.39275 < 188.975 (actual position of left side of control arm on right end)
Numerical value for Minimum position of rocker on left side should be greater than the numerical value of position of 2nd ground pivot
130.178 – 57.3625/2 + 29.5125 =131.00925 > 130.029 (actual position of right side of 2nd ground pivot)
Hence, linkage assembly won't interfere with ground pivots and control arms.

- **Minimum position of center of coupler:**

Numerical value for Maximum position of rocker on right side should be less than the numerical value of position of control arm on the right end
129.985 + 57.3625/2 + 29.5125 =188.17875 < 188.975 (actual position of left side of control arm on right end)
Numerical value for Minimum position of rocker on left side should be greater than the numerical value of position of 2nd ground pivot
129.985 – 57.3625/2 + 29.5125 =130.81625 > 130.029 (actual position of right side of 2nd ground pivot)
Hence, linkage assembly won't interfere with ground pivots and control arms.

Appendix B. APDL Code for volume averaged stress and deformation

APDL code for obtaining volume averaged VonMises stress and averaged deformation

```
cmsel,s,my_elems_fiber,elem
*get,my_elementcount_1,elem,0,count
set,last
etable,vmstr_1,s,eqv
my_element_number_1 = 0
my_vonmises_volume_1 = 0
my_total_volume_1= 0
*do,i,1,my_elementcount_1
  my_element_number_1= elnext(my_element_number_1)
  *get,my_element_volume_1,elem,my_element_number_1,volu
  *get,my_element_vonmises_1,elem,my_element_number_1,etab,vmstr_1
  my_vonmises_volume_1=my_vonmises_volume_1+
my_element_volume_1*my_element_vonmises_1
  my_total_volume_1 = my_total_volume_1 + my_element_volume_1
*enddo
my_volumeaverage_vonmises_1 = my_vonmises_volume_1/my_total_volume_1
nsel,all
esel,all
allsel,all
cmsel,s,my_elems_matrix,elem
*get,my_elementcount_2,elem,0,count
set,last
etable,vmstr_2,s,eqv
```

```
my_element_number_2 = 0

my_vonmises_volume_2 = 0

my_total_volume_2= 0

*do,j,1,my_elementcount_2

  my_element_number_2= elnext(my_element_number_2)

  *get,my_element_volume_2,elem,my_element_number_2,volu

  *get,my_element_vonmises_2,elem,my_element_number_2,etab,vmstr_2

  my_vonmises_volume_2=my_vonmises_volume_2+
my_element_volume_2*my_element_vonmises_2

  my_total_volume_2 = my_total_volume_2 + my_element_volume_2

*enddo

my_volumeaverage_vonmises_2 = my_vonmises_volume_2/my_total_volume_2

nsel,all

esel,all

allsel,all

cmsel,s,my_nodes_fiber,node

*get,my_numnod_1,node,0,count

*get,minnod_1,node,0,num,min

total_1=0

curnod_1=minnod_1

*do,ii,1,my_numnod_1

*get,cux_1,node,curnod_1,u,sum

total_1=total_1+cux_1

*get,nextnod_1,node,curnod_1,nxth

curnod_1=nextnod_1

*enddo
```

```
my_avgdisp_1=total_1/my_numnod_1
nsel,all
esel,all
allsel,all
cmsel,s,my_nodes_matrix,node
*get,my_numnod_2,node,0,count
*get,minnod_2,node,0,num,min
total_2=0
curnod_2=minnod_2
*do,jj,1,my_numnod_2
*get,cux_2,node,curnod_2,u,sum
total_2=total_2+cux_2
*get,nextnod_2,node,curnod_2,nxth
curnod_2=nextnod_2
*enddo
```

Appendix C. Fiber-elastomer combinations

		Silicone/ FVMQ		Nitrile/HNBR/ CR		Fluorocarbon (FKM/FPM)		ACM/EPDM /EPM	
		F	E	F	E	F	E	F	E
Cotton	2	55.15	6.22	56.18	6.76	56.34	6.77	56.21	6.78
	4	110.30	12.44	112.37	13.53	112.67	13.54	112.42	13.56
	6	165.45	18.66	168.56	20.29	169.00	20.32	168.63	20.34
	8	220.60	24.89	224.74	27.05	225.34	27.09	224.84	27.12
	10	275.75	31.10	280.93	33.82	281.68	33.86	281.05	33.90
	12	330.90	37.33	337.11	40.58	338.02	40.63	337.26	40.67

		Silicone/ FVMQ		Nitrile/HNBR/ CR		Fluorocarbon (FKM/FPM)		ACM/EPDM /EPM	
		F	E	F	E	F	E	F	E
Nylon	2	45.84	4.51	55.55	6.52	55.17	6.40	55.90	6.63
	4	91.68	9.03	111.1	13.0	110.3	12.8	111.8	13.2
	6	137.5	13.5	166.6	19.5	165.5	19.2	167.7	19.8
	8	183.3	18.0	222.2	26.1	220.6	25.6	223.6	26.5
	10	229.2	22.5	277.7	32.6	275.8	32.0	279.5	33.1
	12	275.0	27.1	333.3	39.1	331.0	38.4	335.4	39.7

		Silicone/ FVMQ		Nitrile/HNBR		FKM/FPM		ACM/EPDM/EPM	
		F	E	F	E	F	E	F	E
Kevlar	2	55.47	6.07	56.12	6.75	56.28	6.75	56.12	6.75
	4	110.95	12.15	112.24	13.50	112.57	13.50	112.25	13.51
	6	166.42	18.22	168.36	20.25	168.86	20.25	168.38	20.27

	8	221.90	24.30	224.48	27.00	225.15	27.00	224.50	27.03
	10	277.38	30.37	280.60	33.75	281.44	33.75	280.63	33.79
	12	332.85	36.45	336.72	40.50	337.73	40.51	336.76	40.55

Green color indicates that the stress induced in the fiber/elastomer is less than the yield strength, while red color indicates that the stress induced exceeded its yield strength and hence indicates failure of RDS. Further, F and E indicate fiber and elastomer respectively.